Publications

9-5-2013

Synoptic-Scale Precursors, Characteristics and Typing of Nocturnal Mesoscale Convective Complexes in the Great Plains

Shawn M. Milrad
Embry-Riddle Aeronautical University, milrads@erau.edu

Cailee M. Kelly
University of Kansas

Follow this and additional works at: https://commons.erau.edu/publication

Part of the Atmospheric Sciences Commons, and the Meteorology Commons

Electronic Journal of
SEVERE STORMS METEOROLOGY

Synoptic-Scale Precursors, Characteristics and Typing of Nocturnal Mesoscale Convective Complexes in the Great Plains

SHAWN M. MILRAD

Applied Aviation Sciences Department, Embry-Riddle Aeronautical University, Daytona Beach, Florida

CAILEE M. KELLY

Department of Geography, University of Kansas, Lawrence, Kansas

ABSTRACT

Mesoscale convective complexes (MCCs) occur frequently during the warm season in the central U.S. and can produce flooding rains, hail and tornadoes. Previous work has found that the synoptic-scale environment can greatly affect, and be affected by, the development and maintenance of MCCs. Ninety-two MCC cases from 2006–2011 are manually identified using infrared satellite imagery and partitioned into three types (upstream trough, zonal and ridge) using a unique manual synoptic typing based on 500-hPa height patterns. Upstream trough cases feature an amplified longwave 500-hPa trough upstream of the MCC genesis region (GR), while the 500-hPa flow is relatively flat in zonal cases, and a strong 500-hPa ridge is present over the Rockies in ridge cases. Individual case and storm-relative composite analyses of a subset of 28 cases show that of the three types, upstream trough cases feature both the strongest quasigeostrophic forcing for ascent and lower-tropospheric frontogenesis, the latter of which enhances ascent and is associated with a strong southerly low-level jet (LLJ). Zonal and ridge cases feature smaller magnitudes (in descending order) of all ascent-forcing parameters. Ridge cases, in particular, are characterized by weak Q-vector convergence, but easterly upslope flow likely acts as a compensating ascent mechanism. A thermodynamic analysis shows that high-θ_e air is advected into the GR in all three MCC types, and serves as fuel for development and maintenance. However, while the southerly LLJ advects high-θ_e air from the Gulf of Mexico in the upstream trough and zonal cases, such air is already pooled in the High Plains in the ridge cases and advected into the GR by easterly flow. In accordance with the synoptic-dynamic analysis, upstream trough cases have the longest duration and largest impact on the synoptic-scale environment, while ridge cases are the shortest-lived. The various underlying precipitation structures of each group are also explored; zonal cases, for example, appear to preferentially be associated with bow echoes.

————————————————

1. Introduction

a. Motivation

Mesoscale convective complexes (MCCs) occur frequently in the warm season in the central U.S., producing severe weather and extensive rainfall. The original criteria defining

————————————————
Corresponding Author Address: Shawn M. Milrad, Applied Aviation Sciences Department, Embry-Riddle Aeronautical University, 600 S. Clyde Morris Blvd, Daytona Beach, FL 32114.
E-mail: shawn.milrad@gmail.com

MCCs were outlined by Maddox (1980b) (Table 1). MCCs are primarily nocturnal, long-lived, and nearly circular mesoscale convective systems (MCSs) that are frequently expansive enough to encompass multiple states (e.g., Maddox 1980b). MCCs can produce severe hail and wind, flooding rains, and tornadoes. The Maddox (1980b) criteria originally helped to distinguish MCCs from more linear MCSs such as squall lines, which tend to be shorter-lived. However, recent studies generally have either not differentiated between circular MCCs and linear MCSs (Tuttle and Davis 2006; Jirak and Cotton 2007; Trier et al. 2010), or use tools in addition

to infrared (IR) satellite imagery (e.g., radar imagery, Jirak et al. 2003) to determine whether a system is a MCC or a quasi-linear feature (Jirak et al. 2003). In this study, we focus on using the Maddox (1980b) criteria to identify circular MCCs, although radar imagery examined for a subset of our cases indicated a small number of cases that blur the line between MCCs and quasi-linear systems (section 3c).

MCCs have been observed on every continent except Antarctica (Laing and Fritsch 1997; Laing and Fritsch 2000). Relative maxima include Africa (Laing and Fritsch 1993; Blamey 2012), the western Pacific (Miller and Fritsch 1991), South America (Hernandez et al. 1998; Durkee et al. 2009; Durkee and Mote 2010), and western Europe (Garcia-Herrera et al. 2005). Previous work has shown that in North America, MCCs primarily occur between the Rocky Mountains and Mississippi River (e.g., Maddox et al. 1982; Augustine and Howard 1988), and typically dissipate before reaching the Appalachian Mountains (Anderson and Arritt 1998). However, MCCs occasionally have reached the Atlantic Ocean (Maddox et al. 1982; Cotton et al. 1983).

MCCs can have a large impact on life and property. Maddox (1983) found that one-quarter of all MCCs produce injury or death. An MCC originating in South Dakota was found to be partially responsible for the Johnstown, Pennsylvania flood of 1977 that killed 76 people (Zhang and Fritsch 1987; Bosart and Sanders 1981). In addition, MCCs have been found to be an important part of both the global (Laing and Fritsch 1997) and central U.S. hydrological cycles (e.g., Ashley et al. 2003). Research has shown that MCCs can account for as much as 50% of annual rainfall in the central U.S. (Kane et al. 1987; McAnelly and Cotton 1989), although more recent estimates range from 8-20% of warm season precipitation (Laing and Fritsch 1997; Ashley et al. 2003). In general, MCCs tend to be larger than more linear MCSs and thus tend to be more prolific rainfall producers (Jirak et al. 2003).

The various (both harmful and beneficial) impacts of MCCs on life, property, and agriculture made them a popular topic of study in the 1980s, following the development of the Maddox (1980b) criteria. However, while more recent work has investigated MCCs on other continents (e.g., Durkee et al. 2009), little recent work has focused purely on MCCs in North America.

Since the 1980s, modern datasets such as reanalyses have been developed. In fact, much of the earlier research on the synoptic-scale conditions associated with MCCs in the central U.S. was performed using 0000 and 1200 UTC proximity sounding data or objective analyses of such; these analyses are greatly eclipsed in temporal and spatial resolution by modern reanalysis products. Therefore, a primary objective of this study is to investigate the synoptic-scale precursors and dynamics associated with recent MCCs in the central U.S. using reanalysis data.

b. Previous MCC research

1) IDENTIFICATION AND CHARACTERISTICS

MCCs became a popular topic in the literature shortly after satellite imagery became widely available in the 1970s. Maddox (1980a) detailed one of the first IR satellite images of an MCC, and distinguished MCCs from other convective systems. He explained that MCCs interact with the synoptic-scale environment and thus should not be treated as sub-gridscale features. Cotton et al. (1989) found that MCCs are dynamically large, inertially stable, almost geostrophically balanced systems that exceed the Rossby radius of deformation, while Maddox (1980b) found that the MCC cloud shield was often larger than that of tropical cyclones, which occur near the interface of the meso-α and synoptic scales. MCCs are also similar to tropical cyclones in that they generally occur in areas of weak vertical wind shear (on the anticyclonic shear side of the polar jet), and tend to dissipate when they are cut off from their fuel supply of warm moist (high-θ_e) air (Maddox 1980b).

Maddox (1980b) found that the highest frequency of MCCs in the U.S. occurs from May–September, while Augustine and Howard (1988) found it to be May–August, and Jirak et al. (2003) found MCC frequency to be consistent from May–August. Subsequent studies in other regions across the globe found similar seasonality (Miller and Fritsch 1991; Laing and Fritsch 1993). Laing and Fritsch (1997) reported

that in the Northern Hemisphere, the occurrence of MCCs appears to shift northward with the seasonal migration of the polar jet in the spring (MCCs generally occur on the anticyclonic shear side).

The Maddox (1980b) criteria (Table 1) specify that MCCs must meet the size criteria for ≥6 h, and 6–9 h is generally accepted as the lower bound for the duration of MCCs (Maddox et al. 1982). In annual summaries of MCCs for 1981 and 1982, respectively, Maddox et al. (1982) and Rodgers et al. (1983) found an average duration of 12–15 h, although individual MCCs have been observed to last for 2–4 days (e.g., Bosart and Sanders 1981; Cotton et al. 1983). More recently, Jirak et al. (2003) looked at 111 MCCs and found the average duration to be 10.9 h.

Table 1: Criteria for MCCs based upon IR satellite imagery, as first defined by and taken from Maddox (1980b), and later amended by Augustine and Howard (1988).

Size criteria	Interior cold cloud region with IR temperature ≤−52°C must have an area ≥ 50 000 km²
Initiation	Size criteria are first satisfied
Duration	Size criteria must be met for a period of ≥6 h
Maximum extent	Continuous cold cloud shield (IR temperature ≤ −52°C) reaches maximum size
Eccentricity	≥0.7 at time of maximum extent
Termination	Size criteria no longer satisfied

The preferential occurrence of MCCs at night long has been related to the central U.S. low-level jet (LLJ), which is an important aspect of regional climate (Miller and Fritsch 1991; Stensrud 1996). The LLJ occurs in response to: a) differential cooling between the high terrain of the Rockies and the low terrain of the Mississippi River Valley (Ahrens 2008), and b) the inertial oscillation of the lower-tropospheric wind, associated with the decoupling of the boundary layer from the rest of the troposphere (Coniglio et al. 2010 and references therein).

The LLJ is often responsible for the advection of warm, moist (high-θ_e) air from the Gulf of Mexico to the Central Plains where most MCCs occur (Maddox 1983; Wetzel et al. 1983; Trier and Parsons 1993; Augustine and Caracena 1994). This high-θ_e air is believed to serve as the "fuel" for MCC formation and maintenance, without which the MCC likely would dissipate (e.g., Rodgers et al. 1985). More recent work has also connected the northern terminus of the LLJ to strong lower-tropospheric frontogenesis, which serves as a source of mesoscale ascent in MCS development (Tuttle and Davis 2006; Trier et al. 2006; Coniglio et al. 2010; Coniglio et al. 2011). Finally, MCC propagation speed and direction have been found to correlate well with that of the LLJ (Corfidi et al. 1996).

2) SYNOPTIC-SCALE ENVIRONMENT

MCCs typically form due to a combination of synoptic-scale and mesoscale ascent mechanisms in the presence of a relatively unstable air mass. Several observational (mainly radar-based) studies and field campaigns have focused extensively on mesoscale development aspects (e.g., McAnelly and Cotton 1992; Smull and Augustine 1993; Nachamkin et al. 1994), while here we focus primarily on the synoptic-scale environment.

MCC formation typically begins in the late afternoon or early evening as a single thunderstorm, or small cluster of thunderstorms (e.g., Maddox 1980b). The initial thunderstorms may form with or without the presence of orography (Maddox 1980b); Trier and Parsons (1993) found that one-quarter of MCCs originate in the Rockies, and Tripoli and Cotton (1989) reported that in the absence of synoptic-scale forcing, upslope flow in the lee of the Rockies served as an important ascent mechanism for MCC formation.

The region in which the MCC forms was referred to first by Maddox (1983) as the genesis region (hereafter GR). Prior to MCC formation, the GR is usually marked by a strong southerly LLJ (and associated transport of high-θ_e air), low-level warm-air advection (WAA), and an upstream 500-hPa shortwave trough (Maddox et al. 1983; Rodgers et al. 1985; Cotton et al. 1989). As such, midtropospheric cyclonic vorticity advection (CVA) ahead of the shortwave trough and lower tropospheric WAA

were observed in the GR, as both are associated with quasigeostrophic (QG) forcing for synoptic-scale ascent (Maddox 1983). The contribution to QG ascent from WAA, however, typically was found to be of a larger magnitude than CVA (Maddox 1983).

Many studies have also noted a surface frontal boundary and/or lower-tropospheric frontogenesis in—or just to the north of—the GR, and this frontogenesis may also promote ascent (Wetzel et al. 1983; Trier and Parsons 1993; Augustine and Caracena 1994; Anderson and Arritt 1998; Tucker and Zentmire 1999; Trier et al. 2006). Laing and Fritsch (2000) found that it was common for the lower-tropospheric baroclinic zone to be oriented perpendicular to the southerly LLJ. Along those lines, Tuttle and Davis (2006), Trier et al. (2006) and Coniglio et al. (2011) found that the intersection of the LLJ and the baroclinic zone served as the region of strong frontogenesis. As such, the LLJ appears to act as a means to enhanced ascent, in addition to its long-accepted role in the transport of high-θ_e air (moisture and instability).

In general, the GR is frequently located on the anticyclonic shear side of an upper-tropospheric jet streak (e.g., Maddox 1983; Wetzel et al. 1983; Anderson and Arritt 1998), and more specifically in the equatorward exit region (Coniglio et al. 2011), a region that is not typically favorable for ascent. The GR also typically is characterized by high surface dewpoints and large values of CAPE (Laing and Fritsch 2000; Durkee and Mote 2010), on the equatorward side of the surface front (Wetzel et al. 1983; Trier and Parsons 1993). As the MCC matures and propagates eastward into what Maddox (1983) termed the mature region (hereafter MR), the southerly LLJ tends to veer, continuing to produce frontogenesis (ascent) and transport high-θ_e air, which supports MCC maintenance.

Mature MCCs subsequently can have a large impact on the synoptic-scale environment. Many studies have noted that MCCs were associated with large values of upper-tropospheric divergence, in part resulting from latent heat release due to heavy precipitation (Maddox et al. 1981; Maddox 1983; Augustine and Howard 1988; Rodgers et al. 1985; Cotton et al. 1989; Trier et al. 2010). The diabatic heating

and upper-tropospheric divergence in the MR of an MCC has been found to impact the synoptic-scale environment in two ways: 1) increase the geopotential heights in the upper-troposphere, creating an anticyclonic perturbation aloft (e.g., Fritsch and Maddox 1981a; Trier et al. 2010), and 2) create a jet streak or increase the wind speeds in an existing jet streak located to the north of the MR (Fritsch and Maddox 1981b; Maddox et al. 1981; Maddox 1983; Augustine and Howard 1988; Cotton et al. 1989).

c. Objectives

This study aims to examine the synoptic-scale environments associated with MCCs using modern reanalysis datasets, as well as provide new insights into precursors and characteristics of MCCs through a unique partitioning methodology. Specifically, we aim to:

- Perform a manual synoptic typing of MCCs that will partition cases based on the precursor synoptic-scale environment. Our partitioning is based on oft-used 500-hPa height patterns and thus can easily be reproduced;

- Gain additional insight into the synoptic-scale precursors and characteristics of both the GR and MR, based on our synoptic typing. This will be accomplished using individual case and storm-relative composite analyses; and

- Qualitatively assess the impact of mature MCCs on the synoptic-scale environment.

Section 2 details the data used, section 3 presents the case selection, partitioning methodology, and duration statistics, while section 4 contains the synoptic-dynamic analysis. Finally, section 5 discusses conclusions and avenues of future work.

2. Data

MCCs were manually identified using IR satellite imagery from the University Corporation for Atmospheric Research (UCAR) image archive (http://locust.mmm.ucar.edu/) and the University of Wisconsin Space Science and Engineering archive (http://www.ssec.wisc.edu/data/). Radar imagery was downloaded from the Iowa Environmental Mesonet archive (http://mesonet.agron.iastate.edu/archive/). Soundings were downloaded from the University

of Wyoming sounding archive (http://weather.uwyo.edu/upperair/sounding.html).

For the synoptic-dynamic analysis of individual cases, we utilized the National Centers for Environmental Prediction (NCEP) North American Regional Reanalysis (NARR) dataset (Mesinger et al. 2006), which has a 32-km grid spacing and 3-h output. The NARR has been shown to be sufficient at identifying many synoptic-scale and mesoscale features and processes (e.g., Mesinger et al. 2006). The storm-relative composite diagnostics were completed using the NCEP Global Reanalysis (Kalnay et al. 1996), which has a horizontal resolution of 2.5°, and 6-h output. Previous work has shown that the NCEP Global Reanalysis is sufficient for composite synoptic analyses of meso-α scale systems such as tropical cyclones (e.g., Milrad et al. 2009; Atallah et al. 2007), and results were consistent with individual cases examined with the NARR.

The backward trajectory analysis was completed using the NOAA Air Resources Library (ARL) Hybrid Single Particle Lagrangian Integrated Trajectory (HYSPLIT) model (Draxler and Rolph 2012, http://ready.arl.noaa.gov/HYSPLIT_traj.php). We chose the 40 km Eta Data Assimilation System as the dataset for the HYSPLIT model runs, because the Eta (now North American Mesoscale, NAM) model is also used to produce the NARR.

The NARR and NCEP Global Reanalysis graphics were produced using the General Meteorology Package (GEMPAK) version 6.2.0 (Koch et al. 1983).

3. Case selection, partitioning, and appearance

a. Case selection

MCC cases were identified manually from IR satellite imagery using the Maddox (1980b) criteria (Table 1), slightly amended by Augustine and Howard (1988). To meet the size criterion, MCCs must have a large continuous cold cloud region with an IR temperature $\leq$–52°C over an area $\geq$50 000 km^2. Maddox (1980b) originally included a larger, warmer cloud region in the identification criteria, but Augustine and Howard

(1988) later dropped it, arguing that most precipitation falls within the colder interior region. Studies following Augustine and Howard (1988) primarily have used the amended criteria (e.g., Jirak et al. 2003).

Maddox (1980b) stipulated that a system becomes an MCC at the first time that both the size and temperature criteria are met. There is also a minimum time duration (6 h) during which the size and eccentricity ($\geq$0.7) criteria must be met. The eccentricity criterion highlights that MCCs are relatively circular and helps to separate them from more linear MCSs (Augustine and Caracena 1994; Anderson and Arritt 1998). We identified the time that the criteria were first met using IR imagery and defined t = 0 h as the closest NARR (3-h) time. For example, Fig. 1 shows an MCC that first met the Maddox (1980b) criteria at 0515 UTC (Fig. 1b); thus, t = 0 h is defined as 0600 UTC.

This study is not intended to be a climatology of MCCs in the central U.S.; our primary objective is to analyze the synoptic-scale environment during MCC genesis and maintenance. As such, we limited our period of study to 2006–2011 to acquire just enough cases suitable for composite diagnostics (section 4b). Within that period, intervals encompassing April–July roughly correspond to the peak frequency season of MCCs in the central U.S. (Maddox 1980b; Anderson and Arritt 1998; Jirak et al. 2003). In total, we identified 92 MCCs.

An example of the typical evolution of an MCC in the central U.S is seen in Fig. 1. The first thunderstorms initiate in the west-central Plains (GR) around 0300 UTC 12 May 2010 (Fig. 1a), and coalesce into an MCC by 0515 UTC (Fig. 1b) over western Missouri. The MCC appears to be in the MR from approximately 0745 UTC (Fig. 1c) through 1145 UTC (Fig. 1d); it then dissipates gradually until it reaches the Appalachians at 1845 UTC (Fig. 1f). The MCC shown in Fig. 1 produced heavy rain, severe wind, and hail (not shown) over a large area from eastern Kansas to parts of Ohio and West Virginia. It also fell into the typical duration range of an MCC (Maddox et al. 1982; Rodgers et al. 1983; Jirak et al. 2003).
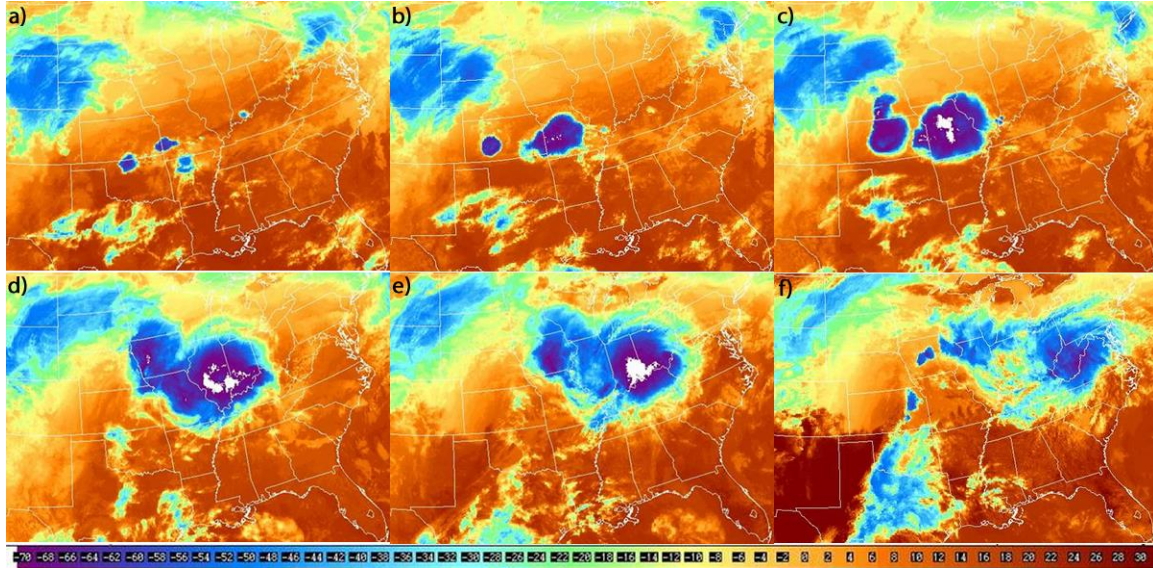
<u>Figure 1</u>: Evolution of an MCC case in this study, using IR satellite imagery. Cloud-top temperatures (°C) are shaded. Case shown is from 12 May 2010 at: a) 0345 UTC, b) 0515 UTC, c) 0745 UTC, d) 1145 UTC, e) 1445 UTC, and f) 1845 UTC. The MCC first met the criteria at 0600 UTC (t = 0 h, Table 2). *Click image to enlarge.*

<u>Table 2</u>: Dates and t = 0 h for the subset of upstream trough (n = 12) cases. The track of each case is shown in Fig. 10a and the sample case used in Fig. 2a,d is denoted in bold italic.

Date	t = 0 h
7 Jun 2009	0600 UTC
16 Jun 2009	0000 UTC
4 Jul 2009	0000 UTC
22 Apr 2010	0900 UTC
12 May 2010	*0600 UTC*
19 May 2010	0900 UTC
22 May 2010	0600 UTC
30 May 2010	0000 UTC
11 Jun 2010	0600 UTC
9 May 2011	0600 UTC
17 May 2011	0300 UTC
20 May 2011	0300 UTC

<u>Table 3</u>: As in Table 2, but for the zonal cases (n = 6), with tracks shown in Fig. 10b and the sample case in Fig. 2b,e.

Date	t = 0 h
21 Jun 2006	0600 UTC
26 Jun 2008	0300 UTC
16 Jul 2008	0300 UTC
8 May 2009	*0900 UTC*
5 Jun 2010	0900 UTC
8 Jun 2010	0600 UTC

b. Case partitioning

   Manual synoptic typing is not new in atmospheric science, having been used for: surface and upper-air analyses of weather events in west Texas (Ladd and Driscoll 1980), an environmental baseline and air-quality analysis in Louisiana (Muller 1977; Muller and Jackson 1985), a synoptic climatology for the Gulf of Alaska (Overland and Hiester 1980), and more recently extreme precipitation events in Atlantic Canada (Milrad et al. 2010). Alpert et al. (2004) found that while automated synoptic typing can be useful, manual typing often is preferred when analyzing mesoscale and/or topographically

<u>Table 4</u>: As in Table 2, but for the subset of ridge cases (n = 10), with tracks shown in Fig. 10c and the sample case in Fig. 2c,f.

Date	t = 0 h
4 Jul 2007	0300 UTC
19 Jul 2007	0600 UTC
20 Jul 2007	0000 UTC
21 Jul 2008	0300 UTC
27 Jul 2008	0000 UTC
11 Jul 2009	*0600 UTC*
12 Jul 2009	0300 UTC
11 Jul 2011	0300 UTC
12 Jul 2011	0600 UTC
16 Jul 2011	0300 UTC

associated phenomena, which may not be handled well by automated typing procedures. Indeed, continental U.S. MCCs are mesoscale phenomena that often originate from convective activity in the Rockies, and evolve into organized convective systems over the Front Range and western High Plains (e.g., Tripoli and Cotton 1989; Trier and Parsons 1993).

We primarily utilize manual synoptic typing to help the forecaster to better identify the synoptic-scale patterns associated with MCC formation and maintenance. Thus, we chose to use 500-hPa geopotential heights as the basis for our manual typing methodology, because it is one of the most commonly-used synoptic-scale variables. Once we identified a) that a case met the Maddox (1980b) criteria and b) t = 0 h, we plotted the NARR 500-hPa geopotential height and geostrophic absolute vorticity at t = 0 h for each case.

From 2006–2011, we identified 92 total MCC cases; partitioned by type into 44 upstream trough, 6 zonal, and 35 ridge cases. Seven cases were not classified because they were on the borderline of either trough-zonal or zonal-ridge categories. The unclassified cases represent only 7.5% of our total, signifying the usefulness and reproducibility of our synoptic typing method. Finally, because a primary component of our study is a composite synoptic analysis, we wanted to create similar numbers of cases among our three groups. Thus, Tables 2–4 list the subset of cases selected for composite analysis in the upstream trough, zonal, and ridge cases, respectively. Since we only found six zonal cases, we used all of them (Table 3). Additionally, 12 upstream trough (Table 2) and 10 ridge (Table 4) cases were selected at random.

Figure 2 presents an example from each group to illustrate the manual synoptic typing methodology. The upstream trough case from 12 May 2010 (Fig. 2a) features a large-amplitude longwave 500-hPa trough centered over the Great Basin region. Embedded shortwave vorticity maxima are evident to the east of the longwave trough. At t = 0 h, the MCC is located in western Missouri (Fig. 1), and proceeds to propagate into the downstream 500-hPa ridge environment, where it eventually dissipates over the Appalachians (Fig. 1f). Similar synoptic-scale patterns were observed by Maddox (1983) and Anderson and Arritt (1998).

The zonal group (n = 6) contains the fewest cases of the three groups (Table 3). Figure 2b shows an example from 8 May 2009. This case was associated with a damaging derecho in Kansas and Missouri, as detailed by Coniglio et al. (2011). The 500-hPa height pattern (Fig. 2b) is much less amplified than in the upstream trough case (Fig. 2a), with the nearest longwave trough located in Montana. However, numerous shortwave ripples are evident in the height field near the GR, in south-central Kansas. Cases with 500-hPa height patterns similar to the zonal cases also have been documented (e.g., Bosart and Sanders 1981; Tripoli and Cotton 1989; Trier et al. 2006; Tuttle and Davis 2006).

The third group is the ridge (n = 10) type, with very different 500-hPa height structures than the other two groups. Figure 2c demonstrates a case from 11 July 2009 in which a large-amplitude 500-hPa ridge is centered over the eastern Rockies, with the closest trough located in northern Wisconsin and Minnesota. There is an apparent lack of shortwave vorticity maxima in or upstream of the GR (Colorado–Nebraska border). While the orography of the Rockies long has been suggested to play a role in the formation of some MCCs (Cotton et al. 1983; Leary and Rappaport 1987; Tripoli and Cotton 1989; Trier and Parsons 1993; Trier et al. 2010), the synoptic-scale environment of such cases has not been extensively detailed. Tripoli and Cotton (1989) and Trier et al. (2010) found that in the absence of synoptic-scale forcing, MCC (MCS) formation was often orogenic (genesis under orographic influences, e.g., Maddox 1980b), and that such MCCs often grew quickly over the Western Plains after originating in the Rockies. The Tripoli and Cotton (1989) case was associated with zonal flow at 500 hPa, in contrast to the dominant ridge seen in Fig. 2c. The 500-hPa height pattern during the time period studied by Trier et al. (2010) was similar to our ridge cases (Fig. 2c), although that study focused on persistent longer-term (week to month) conditions associated with repetitive MCS development.

In addition, the entire subset of ridge cases (Table 3) occurred in the month of July, while the entire subset of upstream trough cases (Table 1) and all but two of the zonal cases occurred in April, May or early June (Table 2). This seasonality generally held true for the full set of cases (e.g., the overwhelming majority of ridge cases occurred in July or late June), and is
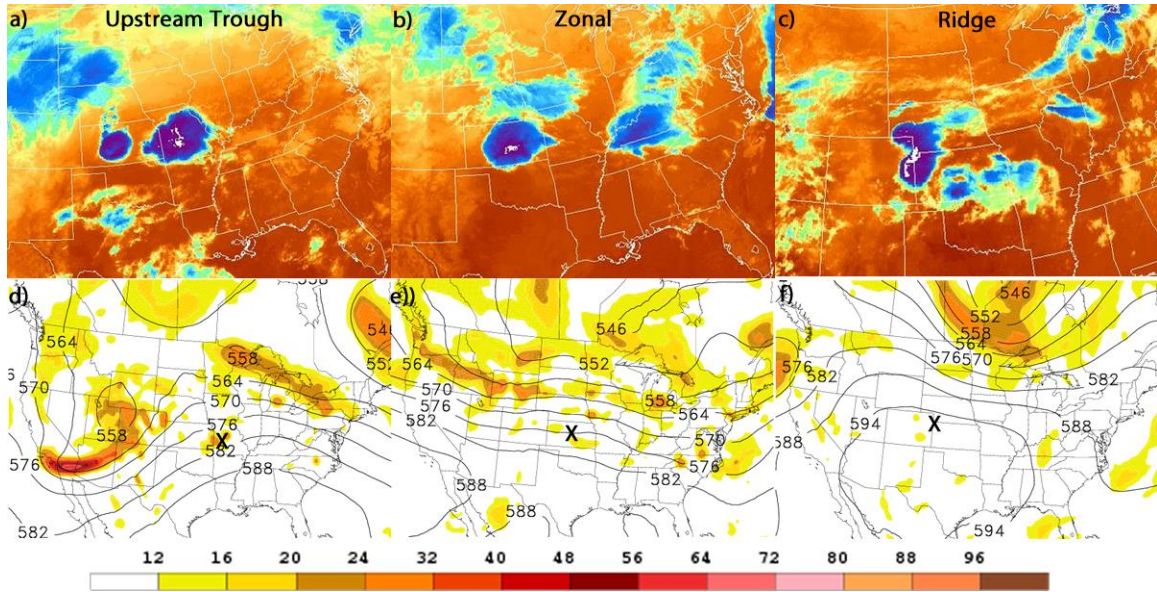
Figure 2: Top row: IR imagery at t = 0 h for sample: a) upstream trough (12 May 2010), b) zonal (8 May 2009), and c) ridge (11 July 2009) cases. Bottom row: Corresponding NARR 500-hPa geopotential height (dam, contoured) and geostrophic absolute vorticity (x 10^{-5} s^{-1}, shaded) at t = 0 h for the d) upstream trough, e) zonal and f) ridge cases.

Table 5: Duration statistics for all three types, including mean and standard deviation.   For the upstream trough and ridge cases, statistics are shown for the subset used in the composite analysis, followed by the full set of cases in parentheses.   All six zonal cases are used in the composite, so only one number is shown.

Type	Mean duration (h)	Standard deviation	Longest duration case (h)	Shortest duration case (h)
Upstream Trough	11.4 (10.5)	3.5 (3.2)	18 (18)	7 (4.8)
Zonal	10.2	3.4	15	6
Ridge	9.3 (9.0)	4.6 (3.6)	19 (19)	6 (4.8)

consistent with the seasonal poleward migration of both the upper-tropospheric jet stream and associated lower-tropospheric horizontal temperature gradient.

Finally, the ridge cases (Table 4) tended to occur in bunches (note two cases each in July 2007, 2008, 2009, and three cases in July 2011), with days between cases ranging from zero to five. This supports Tuttle and Davis (2006) and Trier et al. (2006), who found that certain flow patterns favor repetitive mesoscale precipitation systems over a short-period of time (i.e., a week). Tuttle and Davis (2006) termed these "precipitation corridors", and found that they are preferred in July and August, when the synoptic-scale flow is relatively weak. We believe our ridge cases to be related to precipitation corridors, as they are the only group of cases that exhibit such a temporal pattern (Table 4).

Finally, July is also the peak of the southwest U.S. monsoon season, which can be associated with organized convection in the Central and Southern Rockies (Tripoli and Cotton 1989); this is discussed further in section 3c.

c. Duration and appearance characteristics

In studying 111 cases, Jirak et al. (2003) determined that the average MCC duration was 10.9 h. Following their methodology, we calculated duration statistics for the three types of MCCs in this study. The duration of the MCC is defined by the time it first meets the Maddox (1980b) criteria (see Tables A1–A3 for individual case times). Table 5 shows that the upstream trough cases have the longest mean duration (in both our composite subset of cases and the full dataset), followed by the zonal and ridge cases, respectively. The ridge subset group has the most short-duration events (7 of 10

events last ≤7 h), but contains one event that lasted 19 h, the longest of any case in any group. Thus, the ridge group has the largest standard deviation. Most trough cases last considerably longer than most ridge cases, with the zonal cases falling in between. We believe this is directly related to a more favorable synoptic-scale environment over a longer period of time in the trough cases than the ridge cases, and to some extent the zonal cases. We expand on this hypothesis in our synoptic-dynamic analysis (section 4).

Another important point made by Blanchard (1990) and Jirak et al. (2003) is that not all MCCs (as identified by their circular cold-cloud shield) have circular precipitation patterns. Many of the early MCC papers from the 1980s (e.g., Maddox 1980b; Maddox 1983; Augustine and Howard 1988) were limited solely to the use of IR satellite imagery as a method of identification. Blanchard (1990) and especially Jirak et al. (2003) updated those studies by classifying MCSs based on *both* satellite and radar patterns, which helped to separate more circular MCCs from what Jirak et al. (2003) termed persistent elongated convective systems (PECSs).

The focus of this study is on the synoptic-scale environment during the formation and maintenance of systems that meet the MCC identification criteria (Maddox 1980b; Augustine and Howard 1988), which is based on IR satellite imagery alone. However, for the sake of completeness, it is important to examine the underlying radar structures associated with our cases. To that end, Appendix B (Figs. B1–B3) shows side-by-side IR satellite and composite radar reflectively images for each case in our subsets, at the time of maximum extent (Tables A1–A3).

One finding from the IR satellite imagery alone is that while all cases meet the MCC criteria, some cases take on slightly different shapes at various points during their lifecycles. For example, while upstream trough case 11 (Fig. B1) had one circular cloud shield at t = 0 h (not shown), it appears to have had two main areas of convection at the time of maximum extent. Similar signatures are also seen for some cases in the zonal (e.g., zonal case 4) and ridge (e.g., ridge case 2) groups. This exemplifies that MCCs and PECSs (Jirak et al. 2003) are not mutually exclusive, perhaps underlining why

many recent studies have chosen to use the broader "MCS" designation (e.g., Jirak and Cotton 2007; Coniglio et al. 2010). In this paper, we will continue to use the MCC designation because the MCC criteria (Maddox 1980b; Augustine and Howard 1988) are used to identify our cases, but with two caveats: 1) that some cases can take multiple forms during their lifecycles (i.e., an MCC at one time and a PECS at a later time), and 2) that circular IR satellite shields do not guarantee circular precipitation patterns.

To the second point, a fairly wide range of precipitation patterns is evident in all three MCC types. For example, in the upstream trough group (Fig. B1) at the time of maximum extent, cases 1 and 4 have relatively circular precipitation patterns underneath the circular satellite shield. Meanwhile, upstream trough cases 6 and 9 also have predominantly circular precipitation patterns, but with a bow-echo feature on the southern end of the system. Some other cases (e.g., upstream trough case 12) have multiple areas of precipitation. In the zonal cases (Fig. B2), there are three bow echoes (zonal cases 3, 5 and 6), two mostly circular areas of precipitation (zonal cases 1 and 2), and one with two separate areas of precipitation (zonal case 4). Similar variability is seen in the ridge cases (Fig. B3), including several PECS-like systems (Jirak et al. 2003); however, no bow echoes are seen in the ridge cases. Finally, at least a couple of ridge cases (e.g., ridge cases 1 and 3) appear to be associated with precipitation over the desert southwest. Given the time of year (mid-July), this suggests at least a qualitative association with the southwest U.S. monsoon (Tripoli and Cotton 1989).

Our conclusions from this analysis support what others (e.g., Jirak et al. 2003) have also found: that the underlying precipitation patterns of these systems are more complex than can be identified from IR satellite imagery alone. However, all of our cases do have circular cloud shields in common, which separates them from more linear (squall-line) type systems. As such, we consider a synoptic typing and synoptic-dynamic analysis of the environment during these events to be useful to the forecaster, given the potential severe weather (e.g., Maddox 1980b) and hydrological (e.g., Ashley et al. 2003) threats that these systems pose.

4. Synoptic-dynamic analysis

a. Individual cases

To analyze synoptic-scale mechanisms for vertical motion, we use the adiabatic, frictionless form of the quasigeostrophic (QG) omega equation (Bluestein 1992, p. 329):

$$\left(\nabla_p^2 + \frac{f_o^2}{\sigma}\frac{\partial}{\partial p}\right)\omega = -\frac{f_o}{\sigma}\frac{\partial}{\partial p}\left[-\boldsymbol{v_g}\cdot\nabla_p(\zeta_g + f)\right] - \frac{R}{\sigma p}\nabla_p^2(-\boldsymbol{v_g}\cdot\nabla_p T) \qquad (1)$$

where ω is vertical velocity (Pa s^{-1}), ζ_g is the geostrophic relative vorticity (s^{-1}), f is the latitude-dependent Coriolis parameter, p is pressure, R is the universal gas constant (287 J kg^{-1} K^{-1}), $\boldsymbol{v_g}$ is the geostrophic wind vector (m s^{-1}), and T is temperature (K).

We also use the Q-vector form of the inviscid adiabatic QG omega equation (Hoskins et al. 1978):

$$\left(\nabla_p^2 + \frac{f_o^2}{\sigma}\frac{\partial}{\partial p}\right)\omega = -2\nabla_p\cdot\boldsymbol{Q} \qquad (2)$$

where the sense of the vertical motion is related to the divergence of the $\boldsymbol{Q}$. This was expressed by Hoskins et al. (1978): "In quasi-geostrophic theory…vertical velocity is forced solely by the divergence of $\boldsymbol{Q}$." In other words, areas of Q-vector convergence are associated with QG ascent.

In this study, all Q-vector divergence calculations are averaged through the 850–500 hPa layer. We tested the 400–200 hPa and 850–200 hPa layers (not shown), and while the magnitudes of the Q-vector divergence were smaller, the sign was always identical to that of the 850–500 hPa layer. In our experience in warm season studies (e.g., Hryciw et al. 2013; Milrad et al. 2013), the overwhelming majority of Q-vector divergence is typically manifested in the lower- to mid-troposphere (e.g., 850–500 hPa), and this layer is the best qualitative match with explicit omega values from the reanalysis. In addition, all WAA plots in this paper use 850–700 hPa (layer-averaged). We tested other layers (850–500 hPa and 700–500 hPa), and found very minimal differences; in fact, the 850–700 hPa results were the most robust.

Loosely following Maddox (1983), hereafter we use the term GR for the region in which the MCC forms prior to t = 0 h. At t = 0 h and subsequent times, we use mature region (MR) to describe the area in which the MCC is located, at least until dissipation begins.

1) UPSTREAM TROUGH CASE

The upstream trough case shown here is from 12 May 2010, where t = 0 h is 0600 UTC. In Figs. 3–4, the black 'X' denotes the location of the center of the MCC at each time. An amplified upstream upper-tropospheric trough and jet streak, northwest of the GR at t = –6 h (Fig. 3a), place the GR in the equatorward exit region of the straight jet streak (Maddox 1983), a region typically associated with descent. As the MCC matures (t = 0 h and t = 6 h, Figs. 3c and 3e, respectively), it remains on the anticyclonic shear side of the upper-tropospheric jet streak (Maddox 1983; Anderson and Arritt 1998). Between t = 0 h (Fig. 3c) and t = 6 h (Fig. 3e), the jet streak located poleward of the MR intensifies, which Maddox et al. (1981) and Maddox (1983) related to large values of upper-level divergence in the MR.

Augustine and Howard (1988) noted that even in monthly-averaged fields, mid-tropospheric Q-vector convergence (or negative values of "Div Q", as they called it) was observed in the MCC GR during active months. In the upstream trough case, the GR is marked by large values of Q-vector convergence (Fig. 3b), indicating QG ascent (Eq. 2). This corresponds to both the strong 500-hPa trough located upstream (Fig. 3b), and the strong lower-tropospheric lee cyclone seen in Fig. 4a, because both CVA increasing with height (differential CVA) and lower-tropospheric WAA are associated with QG ascent (Eq. 1). We assume herein that vorticity advection near the surface is small, such that midtropospheric vorticity advection is considered representative of differential vorticity advection in the QG omega equation (Eq. 1). Henceforth, we use mid-tropospheric vorticity advection interchangeably with both differential vorticity advection and vorticity advection increasing with height.

Fig. C1 shows that at t = –6 h, the MCC is located near areas of strong midtropospheric CVA and WAA (Fig. 4b). The existence of WAA was also confirmed independently by examining the t = –6 h (0000 UTC) proximity sounding (e.g., Maddox 1983) from Dodge City, KS (DDC, not shown). By t = 0 h, the MCC has moved downstream of a 500-hPa shortwave ridge, where neutral midtropospheric vorticity

advection is evident (Fig. C1). This suggests that the Q-vector convergence seen in Fig. 3d is primarily due to WAA (Fig. 4d). Finally, at t = 6 h, the MCC is just downstream of a new area of midtropospheric CVA (Fig. C1). Weak WAA is also still evident (Fig. 4f), as the MCC moves downstream of the primary area of Q-vector convergence (Fig. 3f). These findings suggest: a) the Q-vector convergence in the GR is due to both differential CVA and WAA, and b) both mechanisms remain factors in ascent throughout at least part of the MCC evolution. This contrasts with several studies that focused on WAA as the primary QG ascent mechanism in the MR (e.g., Maddox 1983). The existence of midtropospheric CVA and Q-vector convergence in the vicinity of the MCC as late at t = 6 h also might help to explain why this case had an above-average longevity (15 h), even among upstream trough cases (section 3c). We discuss these points further in section 4b.

Finally, Fig. 4a shows a strong southerly LLJ and associated transport of warm, moist (high-θ_e) air from the Gulf of Mexico into the GR at t = −6 h. This continues into the MR at t = 0 h (Fig. 4c) and t = 6 h (Fig. 4e), as the LLJ veers throughout the MCC evolution. Maddox (1983), Trier and Parsons (1989), and Cotton et al. (1989) found that the LLJ typically peaks in the GR during the development stage, although in this case it appears to peak at t = 0 h in the MR (Fig. 4a). Also evident throughout the MCC evolution are large values of lower-tropospheric frontogenesis in both the GR and MR at t = −6 h and t = 0 h (Fig. 4a,c). This frontogenesis indeed occurs at the northern terminus of the LLJ (Tuttle and Davis 2006; Trier et al. 2006; Coniglio et al. 2010; Coniglio et al. 2011) and likely contributes to ascent throughout the life of this case (Fig. 3).

The MCC (after t = 6 h, not shown) finally dissipates when it moves eastward of the WAA and LLJ, and is thus removed from both a QG ascent mechanism and a fuel supply (high-θ_e air).

2) ZONAL CASE

The zonal case chosen is from 8 May 2009, where t = 0 h is 0900 UTC. A typical jet-level height pattern for the zonal cases is evident in Fig. 5: a strong upper-tropospheric straight west-east jet streak, with the MCC GR in the equatorward exit region (Fig. 5a), is seen at

t = -6 h. The MCC remains on the anticyclonic shear side of the jet streak throughout, with the jet streak intensifying in the MR by t = 6 h (Fig. 5e), similar to in the upstream trough case.

Q-vector convergence is evident in the GR at t = −6 h (Fig. 5b), albeit with a smaller magnitude than in the upstream trough case (Fig. 3b). At t = −6 h, Fig. C2 shows that neutral midtropospheric vorticity advection is seen in the GR. Thus, the Q-vector convergence (Fig. 5b, C2) must be due to strong WAA, which is shown in Fig. 6a and was also confirmed independently by examining the t = −9 h (0000 UTC) proximity sounding (e.g., Maddox 1983) from DDC (not shown). By t = 0 h, the Q-vector convergence in the MR (Fig. 5d) is weaker than in the GR; this appears to be due to weaker WAA in the MR (Fig. 6d), as midtropospheric vorticity advection remains neutral (Fig. C2). By t = 6 h (Fig. 5f), the MCC has moved well to the east of the Q-vector convergence near a small area of Q-vector divergence, downstream of a shortwave 500-hPa ridge. Figure C2 confirms that midtropospheric anticyclonic vorticity advection (AVA, associated with QG descent) is evident at this time. The AVA increasing with height combined with weak WAA (Fig. 6f) results in net QG descent (Fig. 5f).

Two key conclusions can be made from this case: 1) The Q-vector convergence in the GR and MR is primarily due to WAA (Fig. 6b,d), not differential CVA, which differs from the upstream trough case and 2) the Q-vector convergence (and thus QG ascent) is shorter-lived than in the upstream trough case. From the latter, one might presume that the MCC was shorter-lived than the upstream trough case. However, Tables A1−A2 show the two cases to have identical longevity (15 h). This apparent contradiction is unique to this particular zonal case (on average, zonal cases are shorter-lived than upstream trough cases), and may be directly related to the fact that it was associated with a derecho, which tends to be a long-lasting and self-sustaining event (Coniglio et al. 2011).

Finally, Fig. 6a,c,e show a similar LLJ pattern for the zonal case as the upstream trough case. The southerly LLJ is strongest at t = 0 h (Fig. 6c), although high-θ_e air advection from the Gulf of Mexico into the GR is evident at t = −6 h (Fig. 6a).
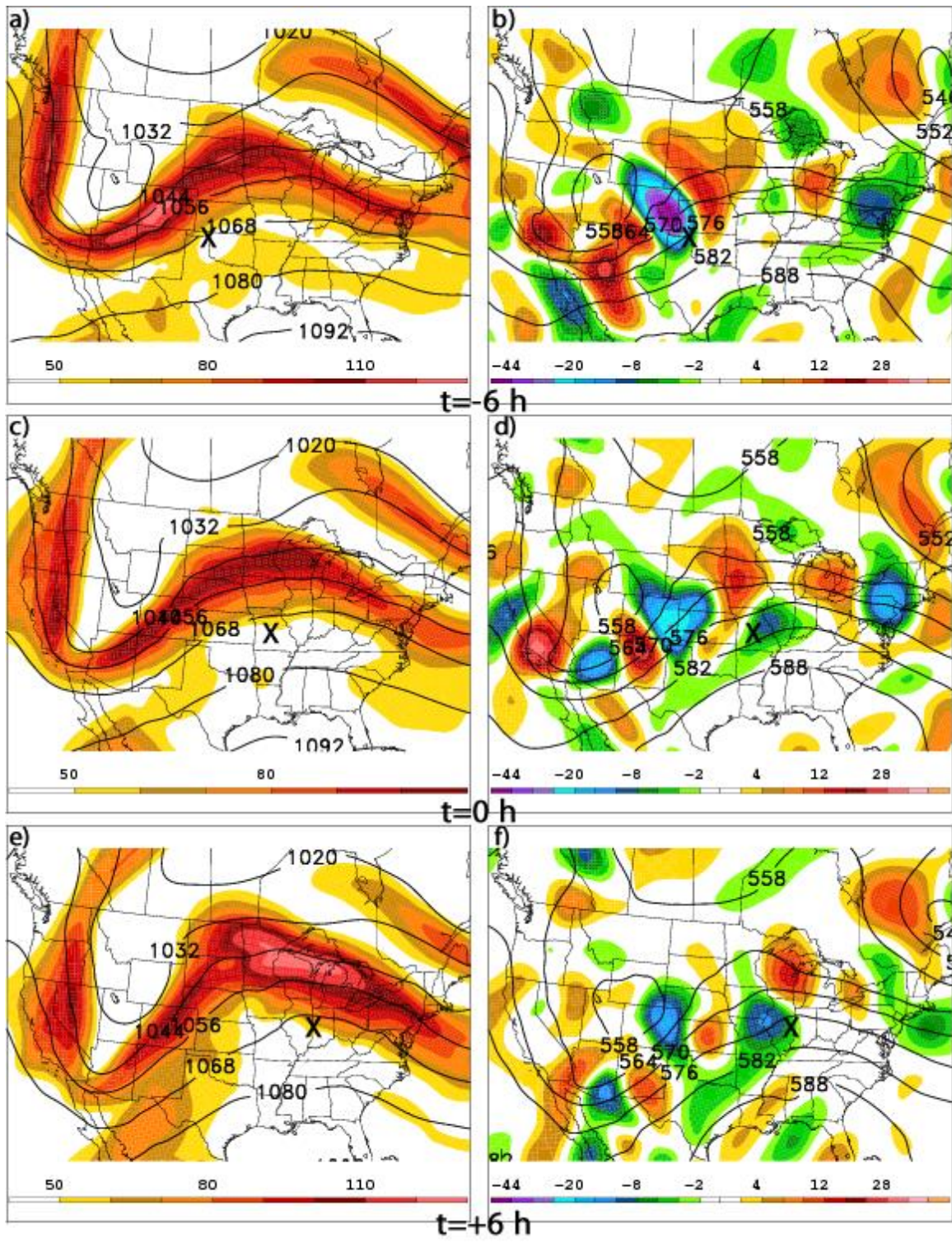
Figure 3: Left: NARR 250-hPa geopotential height (dam, contoured) and wind speed (kts, shaded) for the sample upstream trough case in Fig. 2a at: a) t = –6 h, c) t = 0 h, and e) t = 6 h. Right: NARR 850–500 hPa layer-averaged Q-vector divergence ($\times 10^{-16}$ K m^{-2} s^{-1}, shaded cool colors for convergence, warm colors for divergence) and 500-hPa geopotential height (dam, contoured), at: b) t = –6 h, d) t = 0 h, and f) t = 6 h.
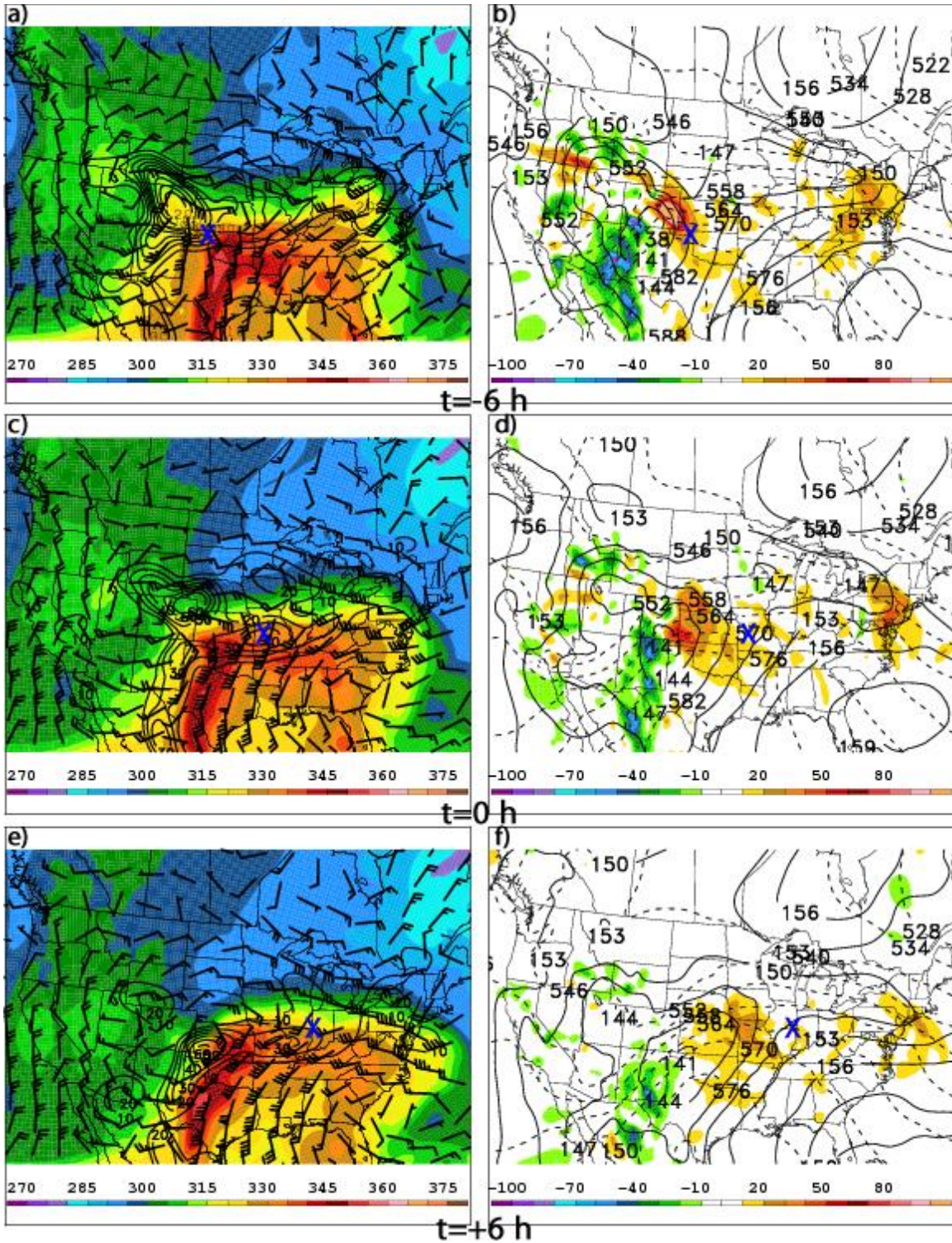
Figure 4: Left: NARR 850-hPa equivalent potential temperature (K, shaded) and winds (kts, barbs), and 1000–700 hPa layer-averaged frontogenesis [solid black contours, $\times 10^{-2}$ K (100 km)$^{-1}$ (3 h)$^{-1}$] for the upstream trough case in Fig. 2a at: a) t = –6 h, c) t = 0 h, and e) t = 6 h. Right: NARR 850–700 hPa layer-averaged geostrophic temperature advection ($\times 10^{-5}$ K s^{-1}, shaded cool colors for cold-air advection, warm colors for warm-air advection), 850-hPa geopotential height (dam, contoured), and 1000–500 hPa thickness (dam, dashed) at: b) t = –6 h, d) t = 0 h, and f) t = 6 h.
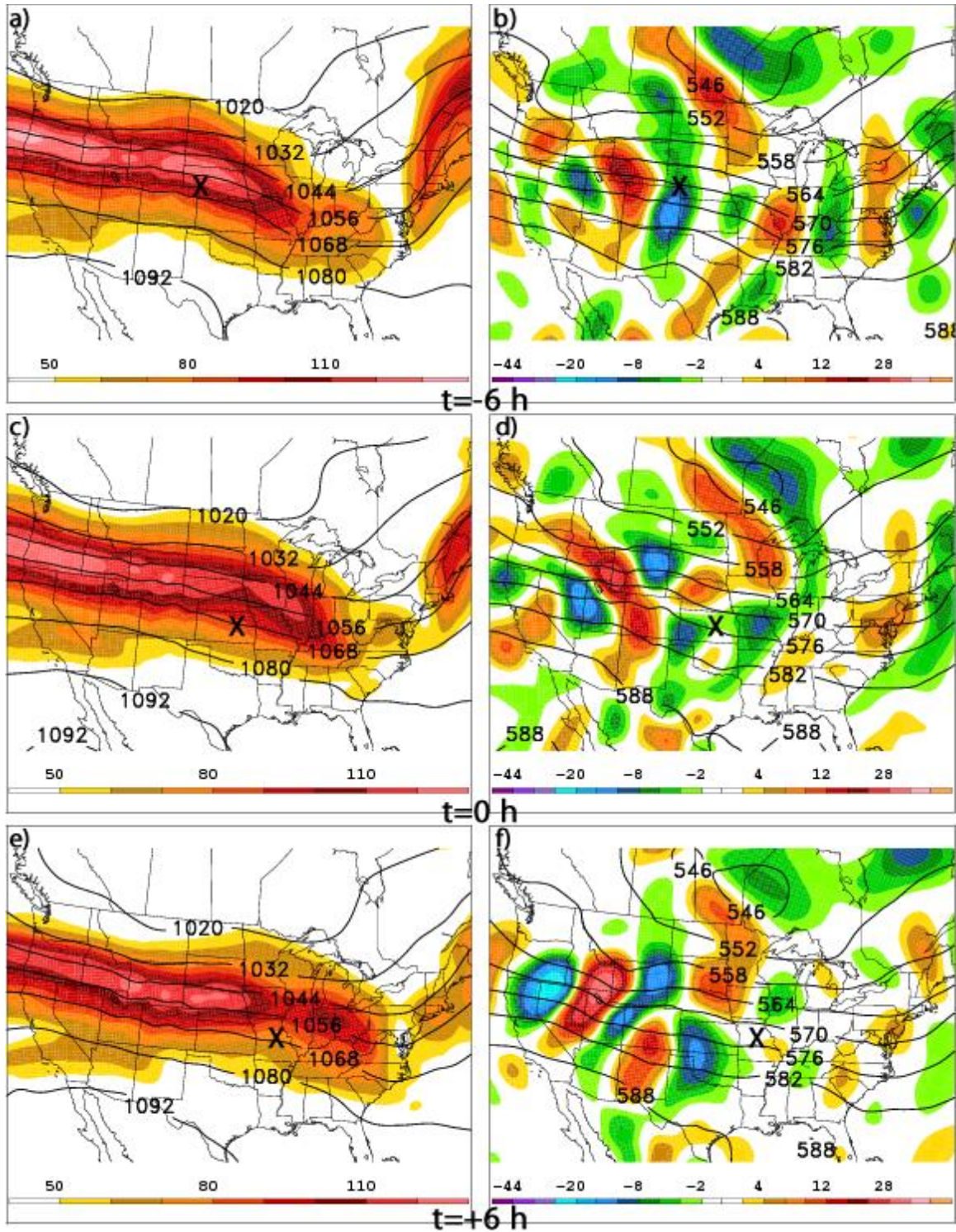
Figure 5: As in Fig. 3, but for the sample zonal case in Fig. 2b.
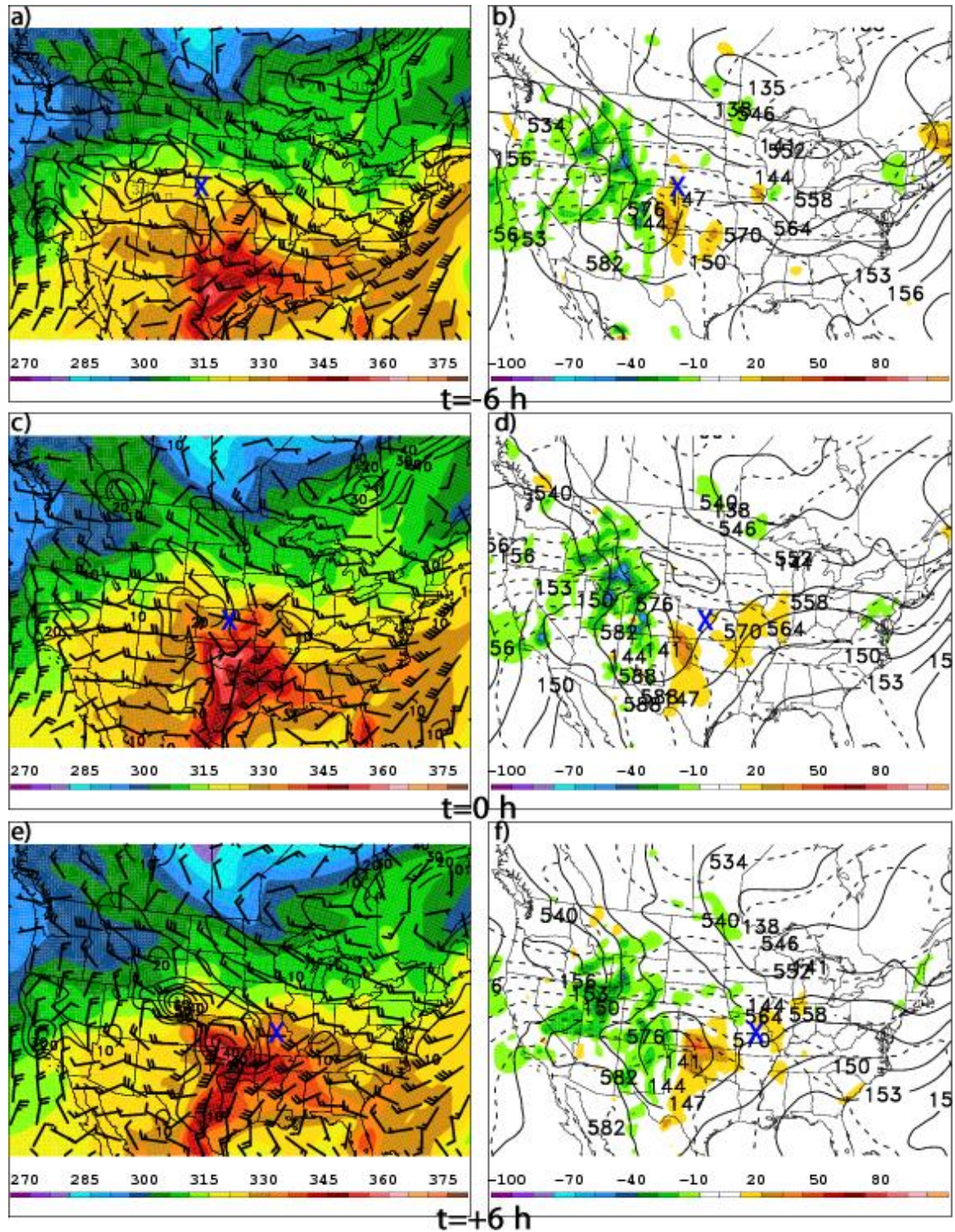
Figure 6: As in Fig. 4, but for the sample zonal case in Fig. 2b

Coniglio et al (2011) also found an unusually strong and deep LLJ for this case. However, the 1000–700 hPa frontogenesis is substantially weaker in both the GR (Fig. 6a) and MR (Fig.

6b) than in the upstream trough case. It is also shorter-lived, as evidenced by the lack of frontogenesis at t = 6 h (Fig. 6e). While it does appear that the frontogenesis contributed to

ascent during formation (as also found by Conligio et al. 2011), its importance appears to decrease as the zonal case progresses eastward. Finally, the LLJ expectedly veers throughout (Fig. 6a,c,e), continuing to supply high-θ_e air throughout the system's lifecycle.

3) RIDGE CASE

The ridge case chosen is from 11 July 2009, where t = 0 h is 0600 UTC. The upper-tropospheric height pattern in the ridge cases is quite different from the other two types; a large upper-tropospheric ridge is centered over the front range of the Rockies throughout the MCC evolution (Fig. 7). As in the upstream trough and zonal cases, the MCC GR and MR are located on the anticyclonic shear side of the upper-tropospheric jet streak (Fig. 7a,c,e); however, they are located in the equatorward entrance quadrant of the straight jet streak (Fig. 7a,c), a region typically associated with ascent.

Figure 7b,d shows that both the MCC GR and MR are collocated with a region of Q-vector convergence that is weaker than in the upstream trough (Fig. 3) and zonal cases (Fig. 5). At t = -6 h, slight midtropospheric CVA is evident in the GR (Fig. C3), owing to a weak shortwave vorticity maximum traversing the longwave ridge environment. Weak WAA (Fig. 8b, C3) is also evident at this time. So while both CVA increasing with height and WAA contribute to the observed Q-vector convergence (Fig. 7b), the magnitudes of all three parameters are small. By t = 0 h, the aforementioned shortwave feature has progressed eastward, leaving the MR in neutral midtropospheric vorticity advection (Fig. C3). Very weak WAA is observed in the vicinity of the MR (Fig. 8d), and this results in even weaker Q-vector convergence (Fig. 7d) than at t = -6 h.

Overall the Q-vector convergence in the GR and MR is of a smaller magnitude than in both the upstream trough and zonal cases. We thus suggest that ascent mechanisms not represented by 850–500 hPa Q-vector divergence may be in play for the ridge case. Specifically, enhanced upper-level divergence in the equatorward entrance region of the jet streak (Fig. 7a,c) and lower-tropospheric upslope flow may both contribute to the synoptic-scale ascent necessary to generate the MCC. To the first point, we produced 400–200 hPa layer-averaged Q-vector

divergence plots (not shown), and the Q-vector convergence at t = -6 h was nearly identical in location and magnitude to Fig. 7b. This suggests upper-tropospheric Q-vector divergence related to the equatorward jet entrance quadrant. To the latter point, Fig. 8b,d shows that an 850-hPa anticyclone is centered to the north and northwest of the GR in northeastern Colorado, indicating that the near-surface wind has an easterly upslope component (Fig. 8a,c). Surface observations from t = -6 h to t = 0 h in eastern Colorado (not shown) confirm this assertion. This case also had a very short lifespan (6.5 h) compared to the upstream trough and zonal cases (Tables A1–A3) and ridge cases in general had the shortest average lifespan of any type (Table 5).

Figure 8 shows a thermodynamic setup different from that in the upstream trough and zonal cases. In Fig. 8a, the highest-θ_e air is located in the Central Plains at t = -6 h. Moreover, there is no coherent southerly LLJ from the Gulf of Mexico at t = -6 h (Fig. 8a). However, with the low-level easterly winds in the vicinity of the GR (Fig. 8a), there is advection of high-θ_e air from into the GR (e.g., Maddox 1983; Trier and Parsons 1989; Cotton et al. 1989). The difference in the ridge case is that the high-θ_e air is already present in the central High Plains and is not being advected directly from the Gulf of Mexico. At t = 0 h (Fig. 8d), a southerly LLJ from the Gulf is evident, but remains to the south and east of the MR, within which easterly flow continues. Finally, as in the zonal case, 1000–700 hPa frontogenesis is evident in both the GR and MR (Fig. 8a,c), but is of a much smaller magnitude than in the upstream trough case.

4) TRAJECTORY ANALYSIS

In order to confirm the differences in LLJ orientation and lower-tropospheric air mass between the three aforementioned cases, we plotted nine backward air parcel trajectories for 24 h prior to t = 0 h from the NOAA HYSPLIT model. Trajectory endpoints are at 850 hPa and distributed within a 2° × 2° box around the center of the MCC at t = 0 h (Fig. 9).

In the upstream trough case (Fig. 9a), air parcels are coming from the south (i.e., the Gulf of Mexico), associated with the aforementioned strong LLJ, and rise as they approach the MR. In the zonal case (Fig. 9b), most air parcels are coming from the south (and rising) in association
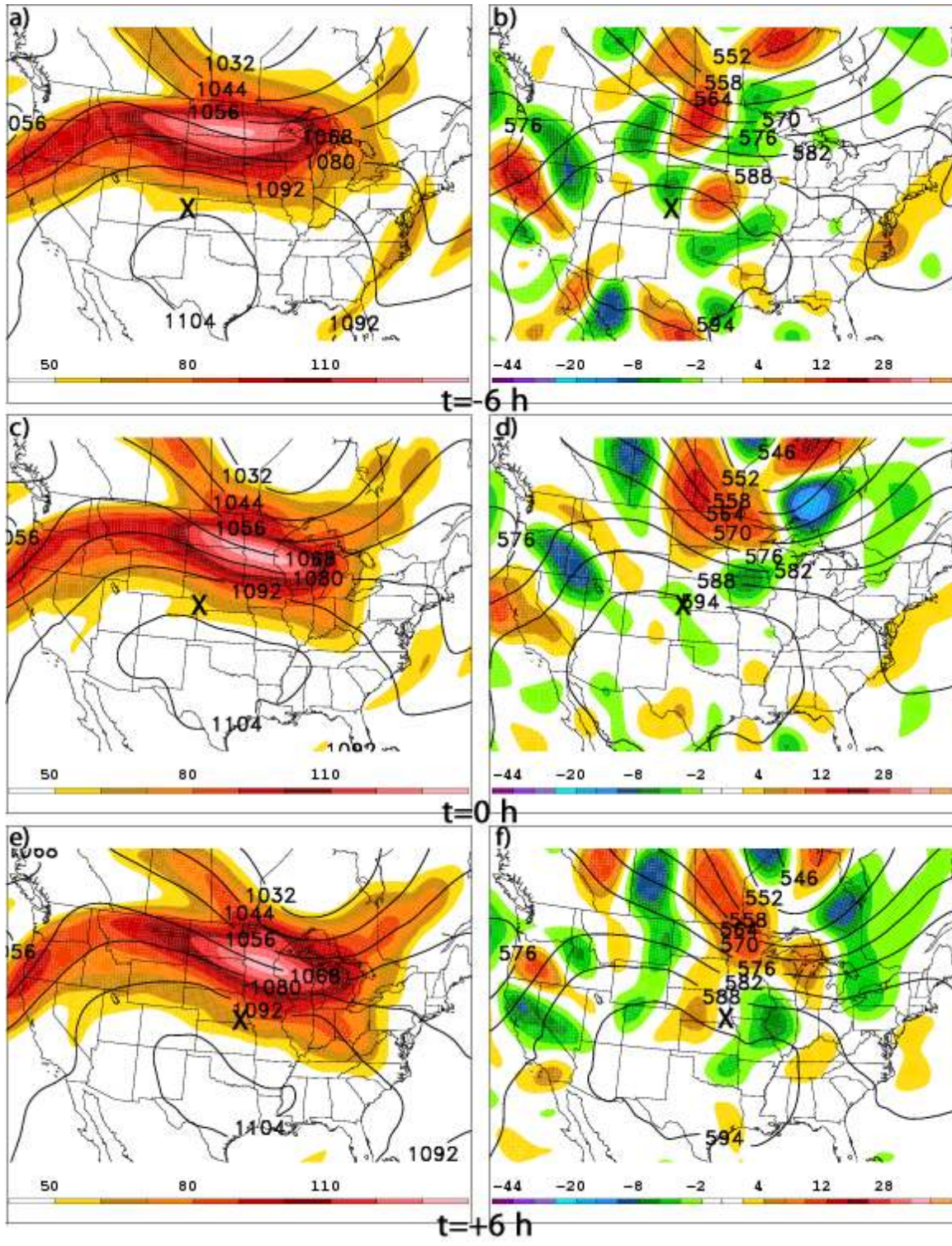
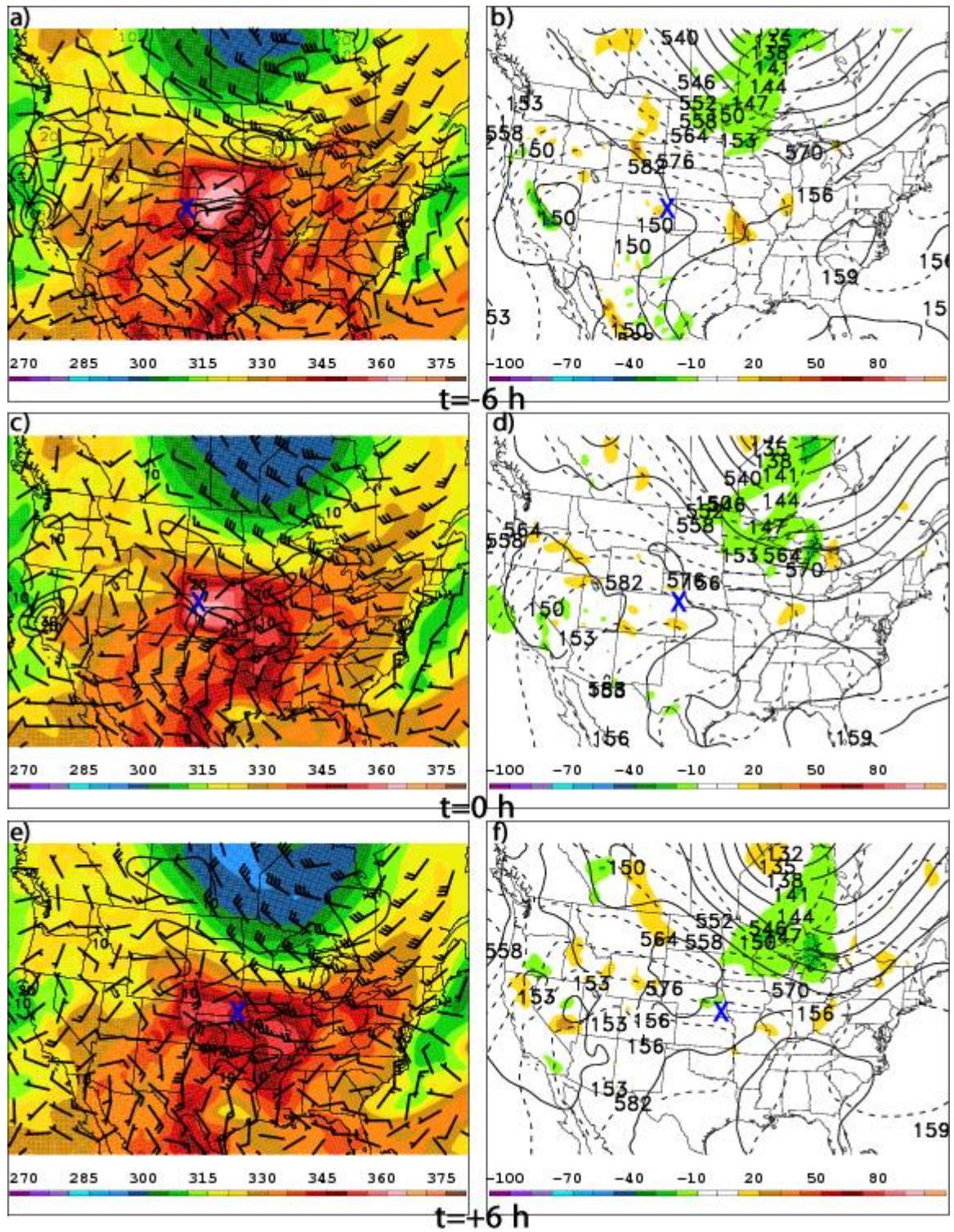Figure 7: As in Fig. 3, but for the sample ridge case in Fig. 2c.

Figure 8*:* As in Fig. 4, but for the sample ridge case in Fig. 2c.

with the LLJ, although a minority come from the southwest, and lack large upward vertical motion. This indicates that the LLJ in the zonal case is narrower than in the upstream trough case, a finding substantiated by Figs. 6c and 4c, respectively.

In the ridge case (Fig. 9c), the trajectories exhibit an entirely different pattern; the majority of trajectories originate from the high-θ_e air in Nebraska and Kansas (Fig. 8d), and ascend as they approach the MR. Meanwhile, a minority of trajectories actually approach the MR from the west, and sink near t = 0 h, likely as a result of

the mesoscale downdraft. The trajectories coming from the east suggest that a southerly LLJ from the Gulf may not be as important for ridge cases. The crucial factor seems to be the advection of already-present high-θ_e air into the GR and MR. This air serves as the fuel supply in formation and maintenance, but it does not necessarily have to be transported directly from the Gulf of Mexico. The advection of already-present high-θ_e air into the GR and MR, in combination with the appropriate ascent mechanisms (i.e., the easterly upslope flow itself), is enough to support an MCC.
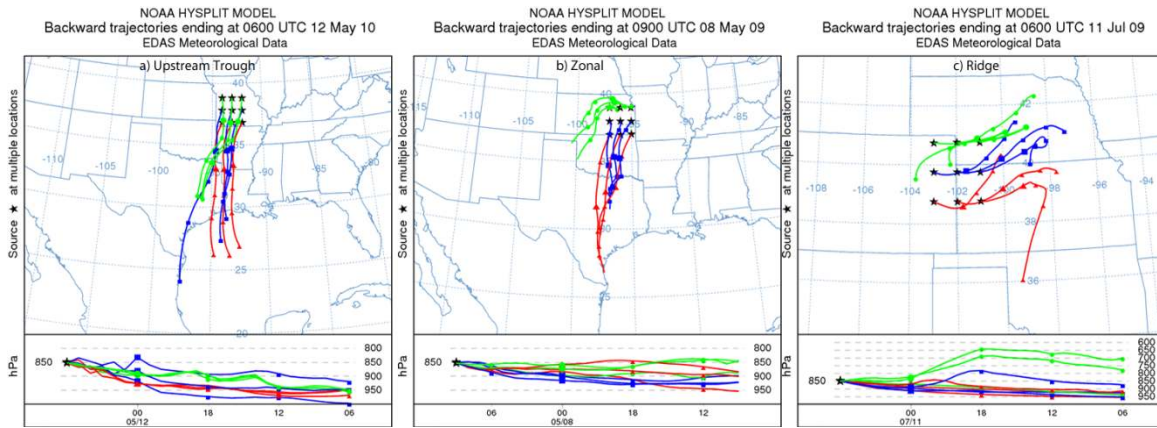
Figure 9: Nine backward trajectories from the NOAA HYSPLIT model starting at t = 0 h with the origin being 24 h earlier and the ending points at 850 hPa (marked with black stars) for the sample a) upstream trough, b) zonal, and c) ridge cases shown in Fig. 2. Ending points are distributed within a 2° latitude × 2° longitude box centered on the middle of the MCC at t = 0 h (marked with an 'X' in Fig. 2). Each dot along a trajectory represents a 6-h backward time step. Note that the map projection in panel (c) is different from that of (a) and (b). *Click image to enlarge.*

b. Composite Analysis

1) METHODOLOGY

In all three MCC types, there is case-to-case track variability (Fig. 10). For example, the 12 upstream trough cases originate as far north as Wyoming and as far south as the Texas Panhandle (Fig. 10a). The MCC endpoints in the 12 upstream trough cases range from northern Wisconsin to West Virginia. There is also some track variability in the zonal (Fig. 10b) and ridge (Fig. 10c) types, albeit less than in the upstream trough cases (Fig. 10a). The track variability subjects a pure composite to considerable smearing, which may result in unreliable or unrealistic composite structures.

To mitigate smearing, all composite diagnostics are produced using a storm-relative

compositing method, as in the extratropical transition work of Atallah et al. (2007) and Milrad et al. (2009). This method composites MCC cases relative to a specific latitude-longitude point based on a reference MCC track. In other words, all the grids in a given composite at t = 0 h are shifted so that each MCC center is located at the same latitude-longitude coordinate, as specified by the reference MCC track. As a result, the composite environment is only relative to the reference track and not the background geography. The geography is retained on the composite plots mainly for the purposes of scale and ease of discussion. Storm positions at each time are generally within five degrees of latitude of each other, therefore minimizing Earth-curvature problems (Atallah et al. 2007).

We chose the reference track to be the average ridge case so that the background geography in the ridge composite is still relevant. This is done because the ridge group has the largest number of cases that originate in/near the Rockies, indicating that the terrain may play a more substantial role in the formation of those cases relative to the other groups. We should note, however, that each group contains some cases that originate in the higher terrain. In the upstream trough and zonal groups, such cases move out of the higher terrain faster than in the ridge cases (Fig. 10).

Due to technical issues (related to grid projection) in producing storm-relative composites using a regional reanalysis dataset (Aiyyer, personal communication), to save time we utilized the NCEP/NCAR Global Reanalysis (Kalnay et al. 1996). While this dataset has a coarser resolution than the NARR, it is still able to diagnose the synoptic-scale environment of meso-α features such as tropical cyclones (e.g., Atallah et al. 2007; Milrad et al. 2009) and MCCs, and in turn, the impact of the meso-$α$ scale features on the synoptic-scale environment (Milrad et al. 2009).

2) RESULTS

The composite diagnostics serve as a comparison and confirmation of the individual case results in section 4a. In addition, they allow us to make general conclusions about the dynamics and thermodynamics of the synoptic-scale environment in each MCC type.

Composites of 500-hPa height and absolute vorticity are presented in Fig. 11. The composites are consistent with the case examples discussed in section 4a. In the upstream trough composite, an amplified longwave trough is located west of the GR at t = –6 h (Fig. 11a). In the zonal composite at t = –6 h (Fig. 11b), there are no amplified synoptic-scale shortwave troughs evident upstream of the GR, while in the ridge composite (Fig. 11c), an amplified synoptic-scale ridge is centered upstream of the GR. In the upstream trough composite, the MCC begins to move into the downstream ridge by t = 0 h (Fig. 11d), and ahead of the ridge at t = 6 h (Fig. 11g) and t = 12 h (Fig. 11j). The zonal and ridge composite 500-hPa geopotential height structures at t = 0 h (Fig. 11e–f) and t = 6 h (Fig. 11h–i) correspond to those described in section 4a.
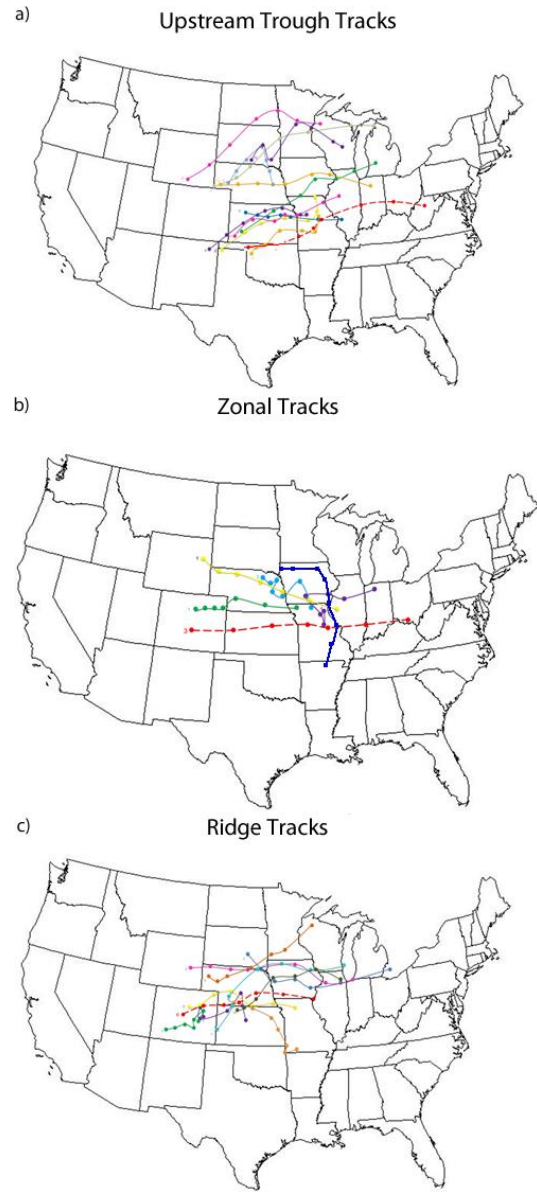

Figure 10: Approximate tracks of all the cases as observed using IR satellite imagery for the a) upstream trough (n = 12), b) zonal (n = 6), and c) ridge (n = 10) groups. Tracks are marked with dots every 3 h from t = –6 h to t = 12 h (t = 0 h is listed in Tables 2–4). The tracks of the sample cases chosen for further analysis in Figs. 3–8 are red dashed in each panel. *Click image to enlarge*.

At t = –6 h, both the upstream trough and zonal composites show an upper-tropospheric jet streak located northwest of the GR (Fig. 12a–b), while Fig. 12c shows a jet streak to the northeast of the GR in the ridge composite. This places the GR in the exit region of a weak, cyclonically

curved jet streak (associated with ascent, Moore and Vanknowe 1992) in the upstream trough composite (Fig. 12a), an equatorward exit region (associated with descent) in the zonal composite (Fig. 12b) and in the equatorward entrance region (associated with ascent) in the ridge composite. In the upstream trough composite, the jet streak to the north of the MR starts to intensify at t = 6 h (Fig. 12g) and continues to do so into t = 12 h (Fig. 12j), suggesting that MCC-related upper-level divergence is helping to intensify the jet streak (Maddox 1983; Anderson and Arritt 1998). The jet streak intensifies in both the upstream trough and zonal composites (Fig. 12e,h,k), but does not intensify at all in the ridge composite (Fig. 12f,i,l).

Strong Q-vector convergence is evident in the GR at t = –6 h in the upstream trough composite (Fig. 13a), slightly weaker Q-vector convergence is seen in the GR of the zonal composite (Fig. 13b), and substantially weaker Q-vector convergence is located in the GR of the ridge composite (Fig. 13c). In the upstream trough composite, the Q-vector convergence at t = –6 h is clearly due to large values of both midtropospheric CVA (Fig. C4) and lower-tropospheric WAA (Fig. 14a). In the zonal and ridge composites, both midtropospheric CVA (Fig. C4) and WAA (Fig. 14b–c) are still evident, but weaker than in the upstream trough composite.

In the MR at t = 0 h, the magnitude of Q-vector convergence is largest in the upstream trough composite (Fig. 13d), followed by the zonal (Fig. 13e) and ridge (Fig. 13f) composites, respectively. Closer inspection of the individual mechanisms shows that midtropospheric CVA is still fairly robust in both the upstream trough and zonal composites, but weaker in the ridge composite (Fig. C4). Meanwhile, very strong WAA is seen in the upstream trough composite (Fig. 14d), followed in decreasing magnitude by the zonal (Fig. 14e) and ridge (Fig. 14f) composites, respectively.

At t = 6 h, strong Q-vector convergence remains evident in both the upstream trough (Fig. 13g) and zonal (Fig. 13h) composites, while the ridge composite exhibits neutral Q-vector divergence (Fig. 13i). The Q-vector convergence in the upstream trough composite at this time appears primarily due to continued strong WAA (Fig. 14g), as the MCC has moved downstream from the main area of midtropospheric CVA (Fig. C4). Meanwhile, both strong midtropospheric CVA (Fig. C4) and WAA (Fig. 14h) are still seen in the zonal composite, while both midtropospheric vorticity advection and lower-tropospheric temperature advection are neutral in the ridge composite (Figs. C4, 14i).

From the findings discussed above, we can conclude that the composite evolution of the upstream trough cases is similar to that of the individual case shown in section 4a. From a QG ascent perspective, the GR is marked by both strong differential CVA and lower-tropospheric WAA. As the MCC propagates away from the upstream trough, WAA becomes a more dominant player, similar to previous results (e.g., Maddox 1983; Jirak and Cotton 2007).

The zonal composite results are somewhat different than that of the individual case discussed in section 4a. That is, the role of differential CVA in QG ascent, while accordingly small in the GR, is substantially larger in the MR in the composite than in the case study. WAA appears to be a prominent QG ascent mechanism throughout the lifecycle of the composite MCC (as in the case study). The end result is much stronger Q-vector convergence in the MR (especially at t = 6 h) than in the GR, which was not evident in the case study. This MR Q-vector convergence (at t = 6 h) is actually stronger in the zonal composite than in the upstream trough composite. The difference in Q-vector convergence magnitude between the zonal composite and the case study suggests that some zonal cases may be sustained for a much longer time period than others, which is supported by the longevity statistics (Tables 5, A2). We do caution however that since the zonal composite only includes six cases, high case-to-case variability is more likely than in the other two composites.

In the ridge composite, the MCC remains in an area of weak Q-vector convergence in the MR (Fig. 13f, i), in agreement with the case study in section 4a. Both midtropospheric CVA (Fig. C4) and WAA (Fig. 14c,f,i) are of a considerably smaller magnitude than in either the upstream trough or zonal composites. Again, we can conclude that synoptic-scale ascent mechanisms not represented by 850–500 hPa Q-vector divergence (specifically the equatorward jet entrance region and low-level upslope flow) likely play a role in the formation and

maintenance of the ridge cases. Finally, we advise the reader to ignore the large area of Q-vector convergence seen in the ridge composite at t = 12 h (Fig. 13l), as this occurs after average

ridge case dissipation (section 3c) and is likely associated with the positively tilted 500-hPa trough located over Wisconsin (Fig. 13l).
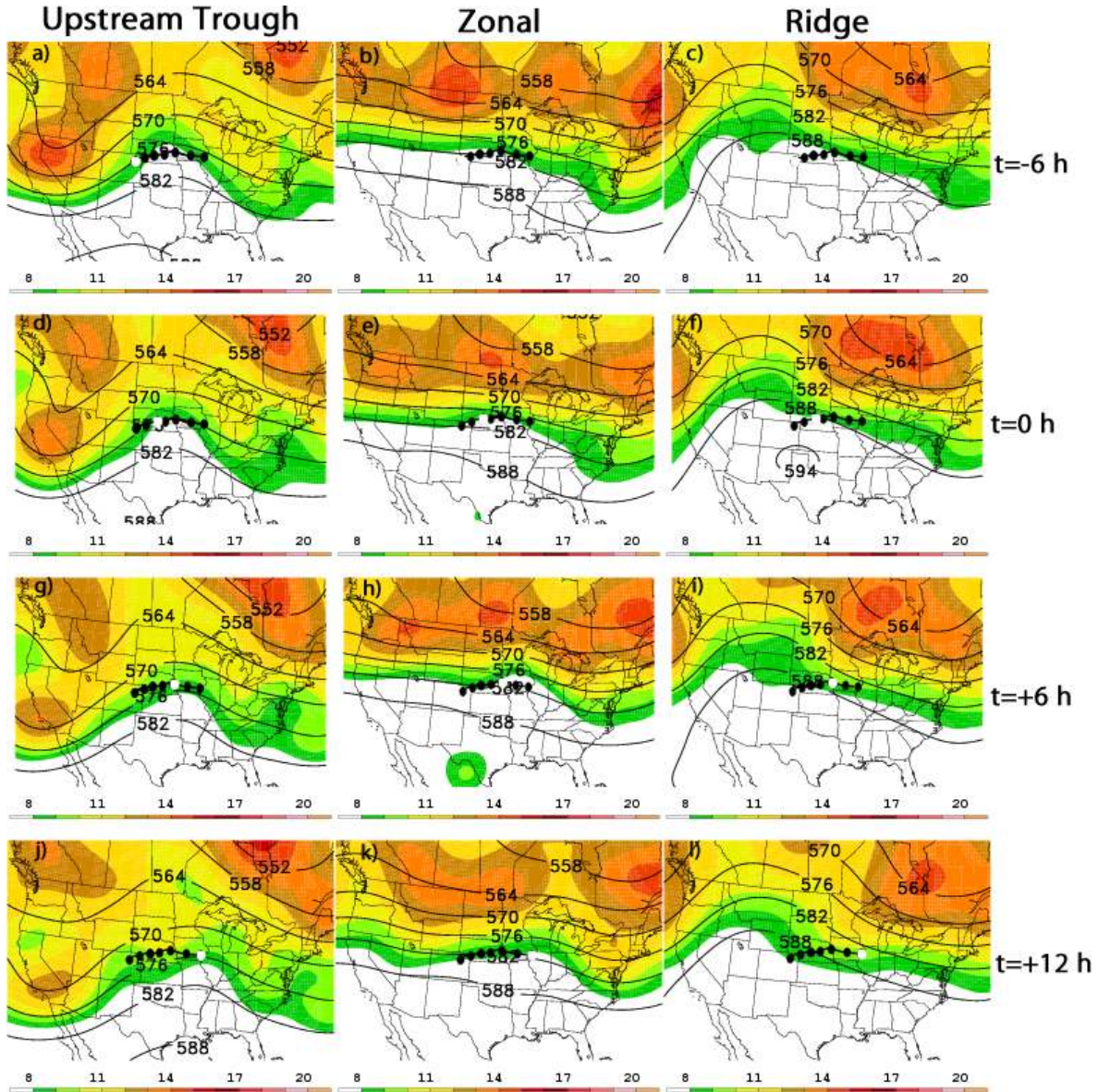

Figure 11: NCEP Global Reanalysis grid-centered composites of 500-hPa geopotential height (dam, contoured) and geostrophic absolute vorticity (x 10^{-5} s^{-1}, shaded), for the upstream trough (left), zonal (middle) and ridge (right) groups. Panels a–c) are for t = –6 h, d–f) for t = 0 h, g–i) for t = 6 h, and j–l) for t = 12 h. The location of the composite storm at each time is marked along the black dotted track with a white dot. *Click image to enlarge*.
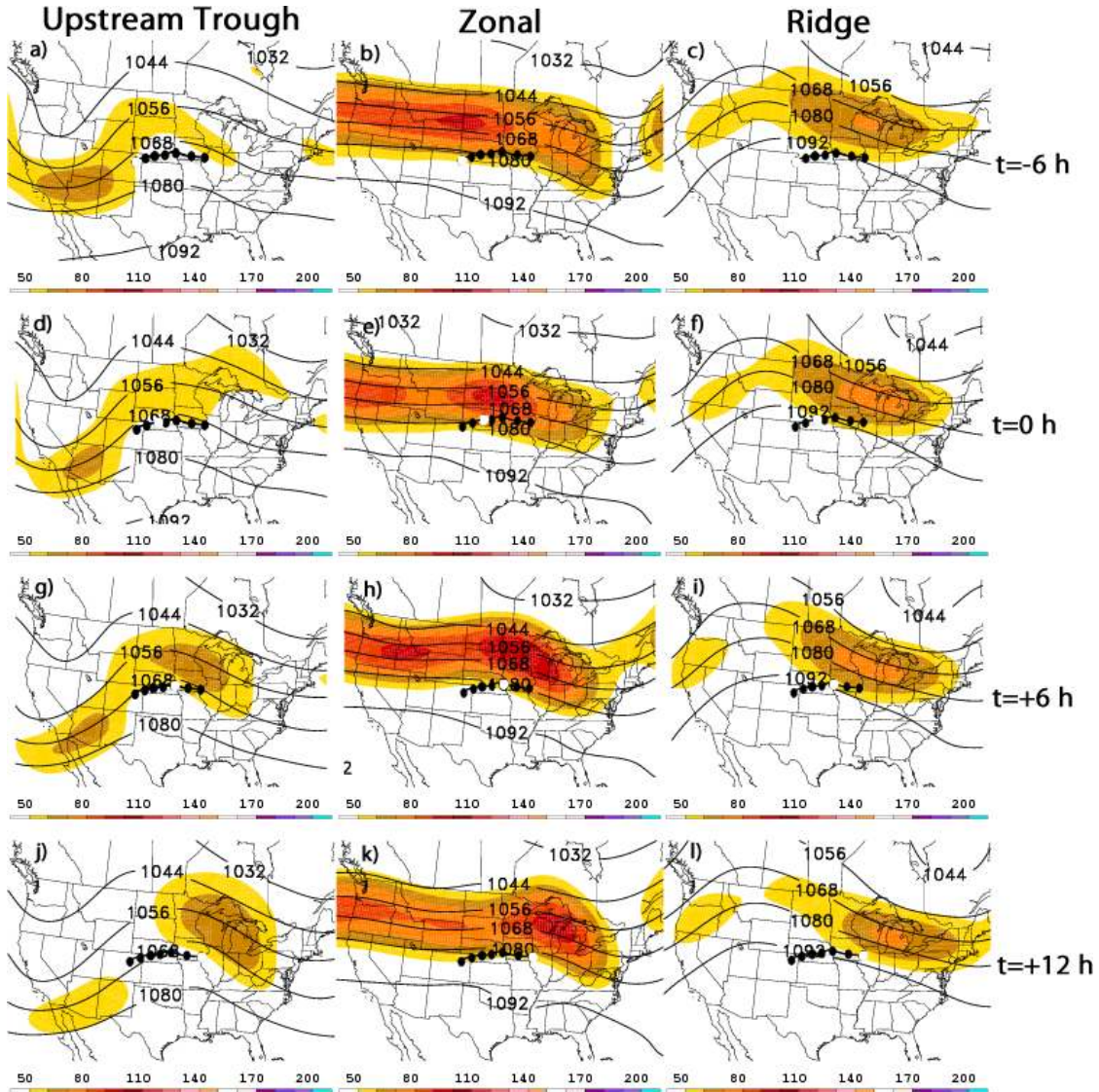
Figure 12: As in Fig. 11, but for 250-hPa geopotential height (dam, contoured) and wind speed (kts, shaded). *Click image to enlarge*.

composites than in the ridge composite. This corroborates the findings of the case studies and suggests that the LLJ is likely stronger in the upstream trough and zonal composites than in the ridge composite. Strong frontogenesis is evident in the location of the upstream trough composite MCC through t = 6 h (Fig. 15d,g), while the MCC gradually moves away from the strongest frontogenesis in the zonal composite (Fig. 15e,h). These conclusions support the recent findings of Trier et al. (2006) and Jirak and Cotton (2007), but also show that the strong frontogenesis from the LLJ is not limited to one (e.g., zonal) synoptic-scale pattern.

Regarding instability and moisture, the southerly LLJ clearly advects higher-θ_e air into the GR and MR in both the upstream trough and zonal composites (Fig. 15), supporting our case study results. However, in the ridge composite, the highest-θ_e air is already pooled near the GR and MR. That is, the southerly LLJ is actually advecting *lower-θ_e* air. Thus, we suggest that in the ridge cases, easterly and southeasterly upslope flow (Fig. 15c) advects the highest-θ_e air (which is already present in the High Plains) into the GR and MR. This is in complete agreement with our case study and trajectory diagnostics, and was also discussed by Trier et al. (2010). Finally, in all three composites, the southerly LLJ continually veers

23

throughout the MCC evolution, as previously documented in several studies (e.g., Maddox 1983).

5. Conclusions and future work

We identify 92 MCC cases from 2006–2011 using IR satellite imagery. Using a unique synoptic typing method based on 500-hPa height patterns, we partition our cases into three groups: upstream trough, zonal, and ridge. Upstream trough cases feature a longwave 500-hPa trough (Fig. 11a) upstream of the GR, while the 500-hPa height pattern is relatively flat in the zonal cases (Fig. 11b), and an upstream ridge is present over the Rockies in the ridge cases (Fig. 11c).

In all three composites, a southerly LLJ is evident in the GR at t = −6 h (Fig. 15), which supports previous findings (e.g., Maddox 1983; Trier and Parsons 1989; Cotton et al. 1989).
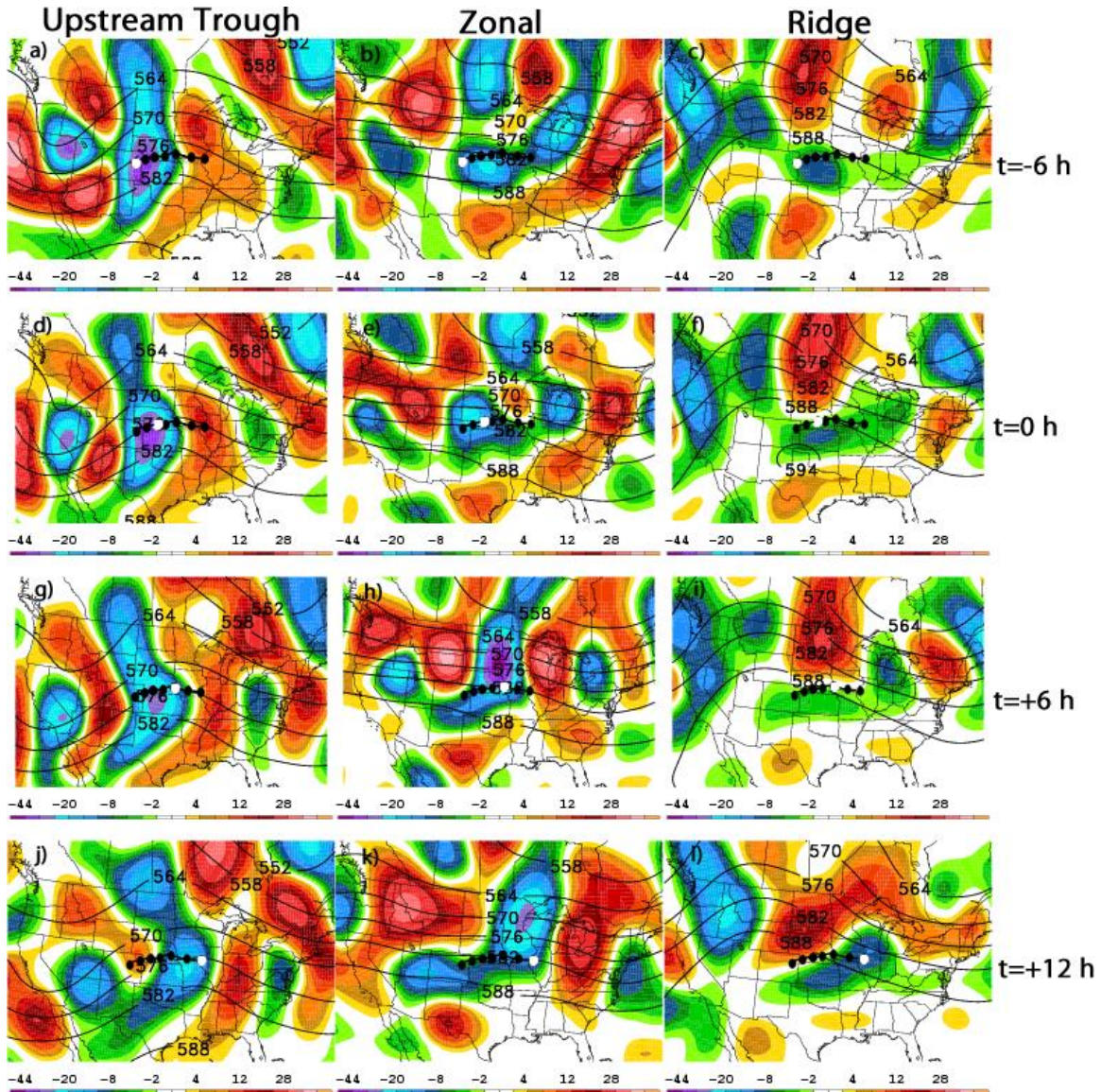
Figure 13: As in Fig. 11, but 850–500 hPa layer-averaged Q-vector divergence ($\times 10^{-16}$ K m^{-2} s^{-1}, shaded cool colors for convergence, warm colors for divergence) and 500-hPa geopotential height (dam, contoured). *Click image to enlarge.*

However, the 1000–700 hPa frontogenesis is much stronger in the upstream trough and zonal.

Using individual case and storm-relative composite analyses, a subset of 28 cases (12 upstream trough, 6 zonal, and 10 ridge) is further investigated. Our results show that upstream trough cases have the longest average duration, while ridge cases have both the shortest average duration and the largest number of cases with short lifespans (≤7 h). Furthermore, while all cases meet the Maddox (1980b) MCC identification criteria, precipitation patterns underneath the circular cloud shield are of a wide variety (Appendix B, Jirak et al. 2003). Upstream trough cases feature the most circular precipitation patterns, while zonal cases appear preferential to bow echoes. No bow echoes are evident in ridge cases, but several cases appear to be related to the southwest U.S. monsoon, especially given the time of year in which they occur (late June to late July). Ridge cases also tend to occur in bunches (Table 4), which supports the "precipitation corridors" discussed by Tuttle and Davis (2006).
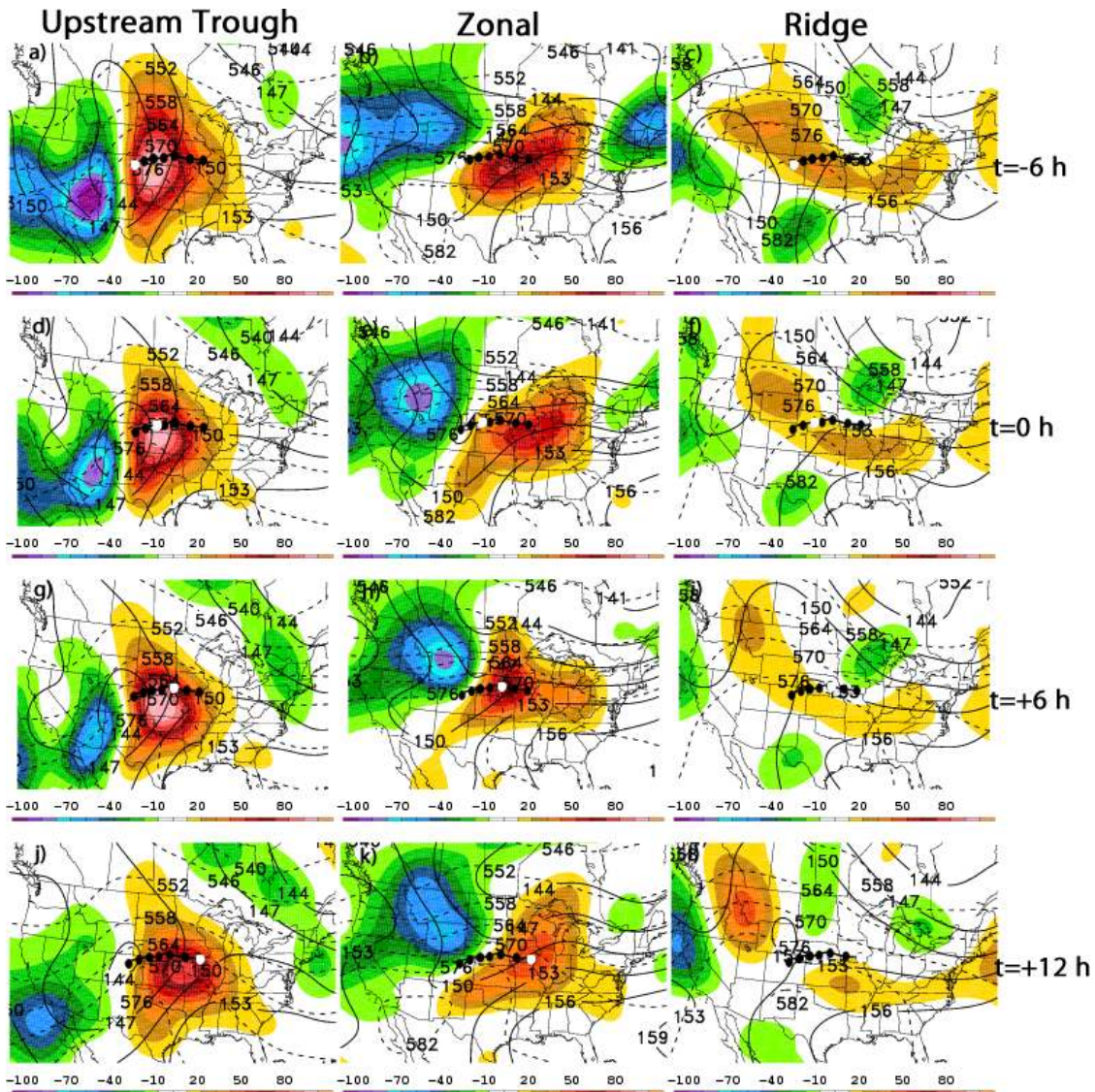
Figure 14: As in Fig. 11, but for 850–700 hPa layer-averaged geostrophic temperature advection (x10⁻⁵ K s⁻¹, shaded cool colors for cold-air advection, warm colors for warm-air advection), 850-hPa geopotential height (dam, contoured), and 1000–500 hPa thickness (dam, dashed). *Click image to enlarge.*
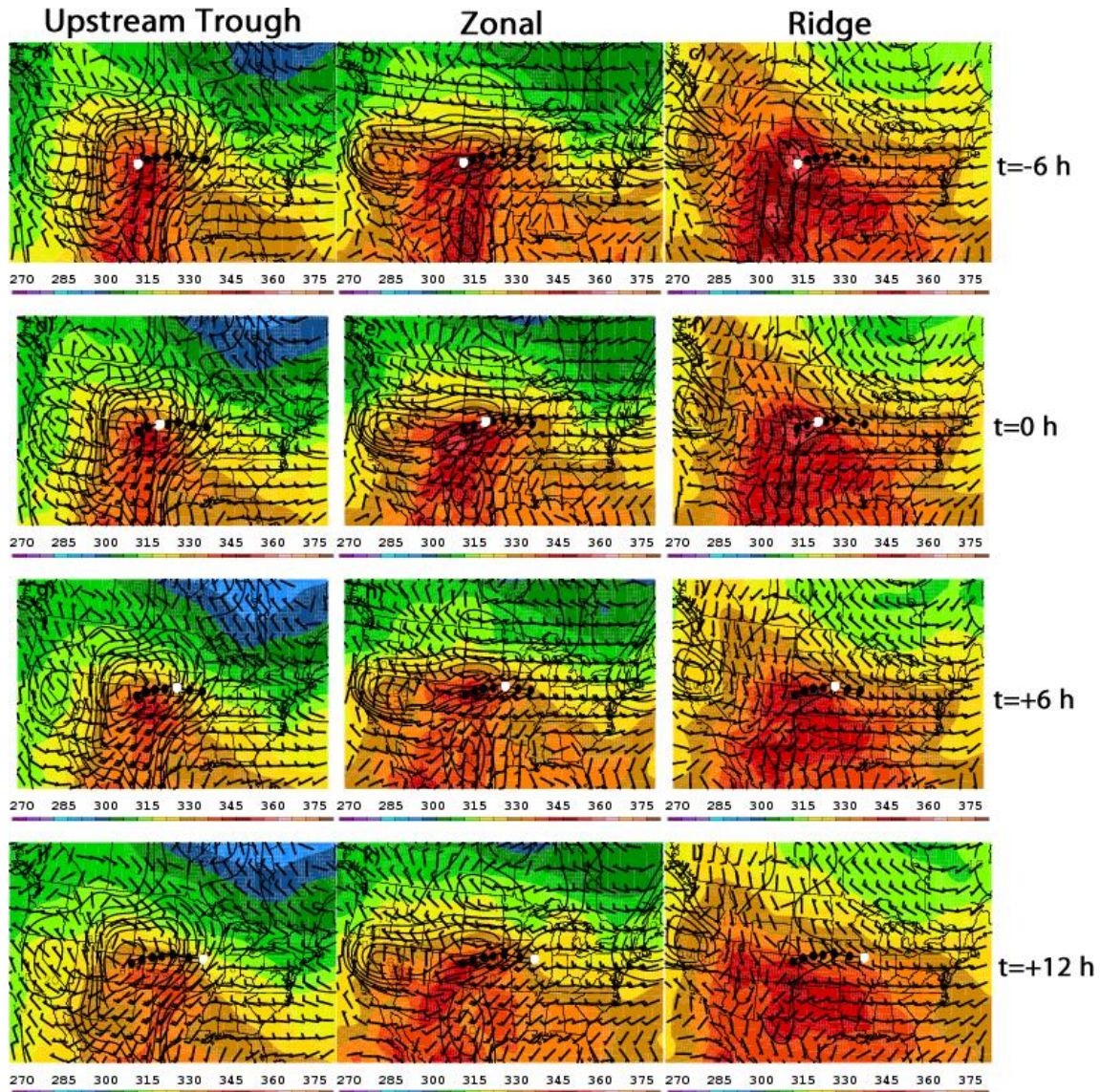
<u>Figure 15</u>: As in Fig. 11, but for 850-hPa equivalent potential temperature (K, shaded) and wind (kts, barbs), and 1000–700 hPa layer-averaged frontogenesis [solid black contours, x10^{-2} K (100 km)$^{-1}$ (3 h)$^{-1}$]. *Click image to enlarge.*

Our synoptic-dynamic analysis finds that, consistent with past research, all MCCs occur on the anticyclonic shear side of an upper-tropospheric jet streak.   However, important differences exist among the three groups. First, the GR in the upstream trough cases is located in an exit region of a weak cyclonically curved jet and in an entrance region of a weak anticyclonically curved jet (Fig. 12a), both regions of ascent (Moore and Vanknowe 1992). Second, while the zonal cases form in an equatorward exit region (Fig 12b), the ridge cases tend to form in an equatorward entrance region (Fig 12c). This indicates that two of our

three types (upstream trough and ridge) form in a jet region that does not fit the traditional paradigm (Maddox 1983).

During the formation stage (in the GR), the upstream trough cases feature the strongest Q-vector convergence of any type (Fig. 13); our results indicate that this is due to a combination of differential CVA and lower-tropospheric WAA (Appendix C). Both differential CVA and WAA remain factors throughout the lifecycle of the upstream trough cases, although WAA is generally of a larger magnitude (Maddox 1983). WAA is also present throughout the lifecycle of

zonal cases, but is weaker than in the upstream trough cases. Finally, the ridge cases feature much weaker mid-tropospheric Q-vector convergence than the other two types. We suggest that compensating synoptic-scale ascent is provided by easterly upslope flow in the lee of the Rockies and upper-level divergence in the equatorward entrance region of the jet streak.

The climatological Great Plains LLJ, which is maximized at night (e.g., Stensrud 1996), presumably plays a crucial role in supplying and sustaining the fuel supply (i.e., high-θ_e air) and by providing additional ascent via lower-tropospheric frontogenesis (e.g., Trier et al. 2006). Our results find that the upstream trough cases have the strongest, most southerly LLJ (Figs. 9, 15). Accordingly, the upstream trough cases have the largest values of 1000–700 hPa frontogenesis in the GR and MR, which likely contributes to ascent throughout the MCC lifecycle. The LLJ is similar in the zonal cases (Fig. 15), but slightly weaker and more southwesterly. Frontogenesis is also present in the zonal cases, but weaker and shorter-lived. The ridge cases, however, feature an entirely different pattern: the highest-θ_e air is already present in the High Plains prior to MCC genesis. Although a southerly LLJ is evident near the GR in the ridge cases, it is actually advecting *lower-θ_e* air from the south into the High Plains (Fig. 15). Moreover, the frontogenesis in the ridge cases is the weakest and shortest-lived of any type. This suggests that southeasterly upslope flow advects the highest-θ_e air into the GR from the nearby High Plains θ_e maximum. Thus, while high-θ_e advection is an important factor in MCC development and maintenance, such transport does not necessarily have to originate directly from the Gulf of Mexico.

Upstream trough cases are on average the longest-duration and most intense group, featuring the strongest QG ascent and lower-tropospheric frontogenesis over the longest period of time. Moreover, these cases feature the widest and strongest southerly LLJ, which helps to advect high-θ_e air continually into the GR and MR. On the other end of the spectrum, ridge cases feature weak QG forcing for ascent and frontogenesis, and do not appear to be supported by high-θ_e air advection from the Gulf of Mexico. Thus, ridge cases have the shortest average duration and more often than not struggle to be sustained for >7 h.

Finally, because MCCs tend to produce a maximum in diabatic heating in the mid-troposphere (700–400 hPa), the effects of the diabatic heating should be to raise geopotential heights in the upper-troposphere (e.g., Cotton et al. 1989; Trier et al. 2010), and create areas of enhanced upper-level divergence. We find that in upstream trough cases, the downstream upper-tropospheric jet streak strengthens over time (Fig. 12). Some jet streak intensification is also seen in the zonal cases, while little to no intensification is observed in the ridge cases. This suggests that the upstream trough cases (which are the strongest and have the longest duration) feature the greatest latent heat release from intense precipitation, and therefore act to build the downstream upper-level ridge more than the other two MCC types.

The previous conclusion sets up a hypothetical, yet important aspect for future work: if in response to strong diabatic heating, upstream trough cases feature the largest upper-tropospheric height rises of any type, then these cases may have a greater impact on features far removed from the original MCC. That is, if latent heat release from an upstream trough MCC acts to build the downstream upper-tropospheric ridge, it is conceivable that downstream Rossby wave development would lead to a stronger downstream upper-tropospheric trough than would occur without the MCC. Similar signatures have been observed with other meso-α scale features such as tropical cyclones (Atallah et al. 2007; Milrad et al. 2009), such that a full quantification of the role of the MCC in this process is warranted.

ACKNOWLEDGMENTS

APPENDIX A
Dates and key times of each case

Table A1: Dates and key times for the subset (n = 12) of upstream trough cases. The track of each case is shown in Fig. 10a and the sample case used in Fig. 2a,d is denoted in bold italic.

Date (of t = 0 h)	First thunderstorm (UTC)	t = 0 h (UTC)	Maximum extent (UTC)	No longer meets MCC criteria (UTC)
7 Jun 2009	0200	0600	1100	1500
16 Jun 2009	2100 (15 Jun)	0000	0800	1800
4 Jul 2009	2100 (3 Jul)	0000	0700	1500
22 Apr 2010	2030 (21 Apr)	0900	1400	1730
12 May 2010	*0230*	*0600*	*1200*	*2100*
19 May 2010	2200 (18 May)	0900	1300	1700
22 May 2010	2200 (21 May)	0600	1200	1830
30 May 2010	2200 (29 May)	0000	0600	1200
11 Jun 2010	0000	0600	0930	1430
9 May 2011	0000	0600	1100	2000
17 Jun 2011	1800 (16 Jun)	0300	0500	1000
20 Jun 2011	2300 (19 Jun)	0300	0900	1700

Table A2: Dates and key times for the zonal (n = 6) cases. The track of each case is shown in Fig. 10b and the sample case used in Fig. 2b,e is denoted in bold italic.

Date (of t = 0 h)	First thunderstorm (UTC)	t = 0 h (UTC)	Maximum extent (UTC)	No longer meets MCC criteria (UTC)
21 Jun 2006	2000 (20 Jun)	0000	0700	0900
26 Jun 2008	2300 (25 Jun)	0300	0600	0900
16 Jul 2008	2100 (15 Jul)	0300	0600	1030
8 May 2009	*0530*	*0900*	*1400*	*0000 (9 May)*
5 Jun 2010	2200 (4 Jun)	0600	1100	1500
8 Jun 2010	2130 (7 Jun)	0300	0600	1730

Table A3: Dates and key times for the subset (n = 10) of ridge cases. The track of each case is shown in Fig. 10c and the sample case used in Fig. 2c,f is denoted in bold italic.

Date (of t = 0 h)	First thunderstorm (UTC)	t = 0 h (UTC)	Maximum extent (UTC)	No longer meets MCC criteria (UTC)
4 Jul 2007	2100 (3 Jul)	0300	0500	1030
19 Jul 2007	0130	0600	0830	1200
20 Jul 2007	2000 (19 Jul)	0000	0530	0700
21 Jul 2008	0000	0300	0600	1400
27 Jul 2008	1830 (26 Jul)	0000	0200	0630
11 Jul 2009	*0200*	*0600*	*0900*	*1230*
12 Jul 2009	2200 (11 Jul)	0300	1300	2000
11 Jul 2011	2200 (10 Jul)	0300	1200	0100 (12 Jul)
12 Jul 2011	2030 (11 Jul)	0600	0900	1200
16 Jul 2011	2100 (15 Jul)	0300	0900	1030

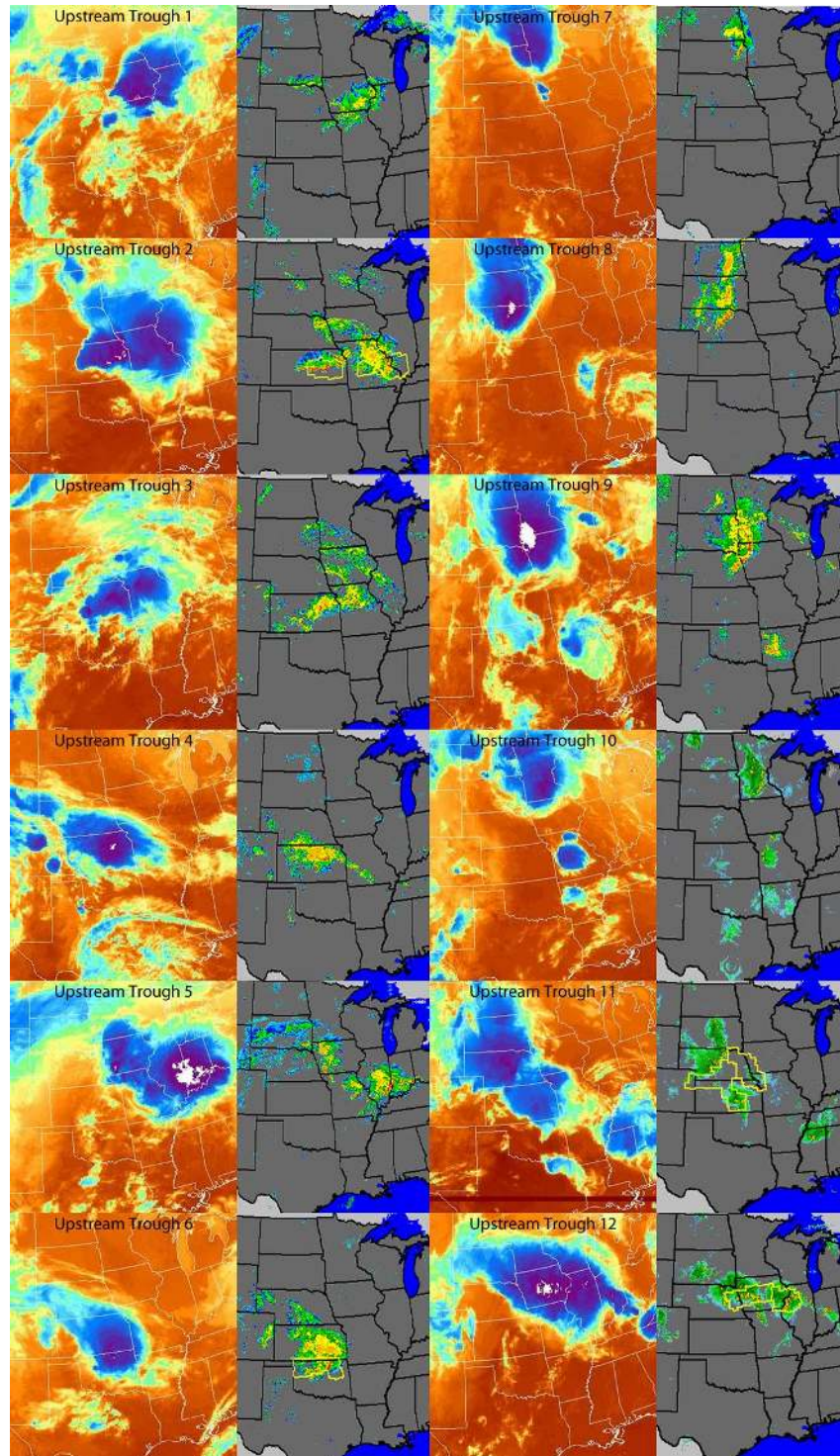APPENDIX B
Satellite and radar characteristics of each case

Figure B1: For the subset of upstream trough cases (n = 12), 10–12 μm IR satellite imagery and composite radar reflectivity at the time of maximum extent for each MCC (see Table A1). Yellow and red polygons represent Storm Prediction Center severe thunderstorm and tornado watches, respectively. *Click image to enlarge.*
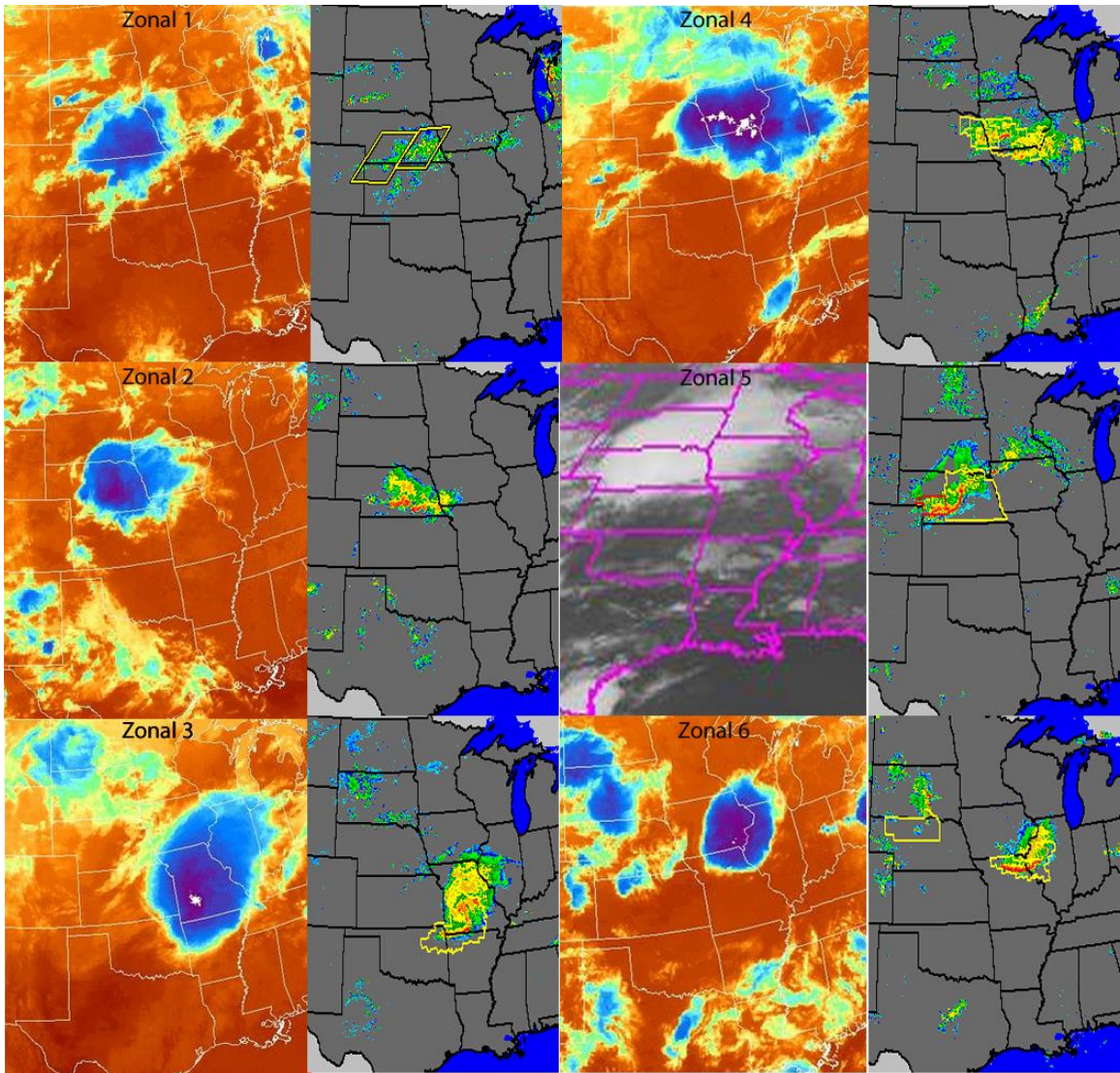
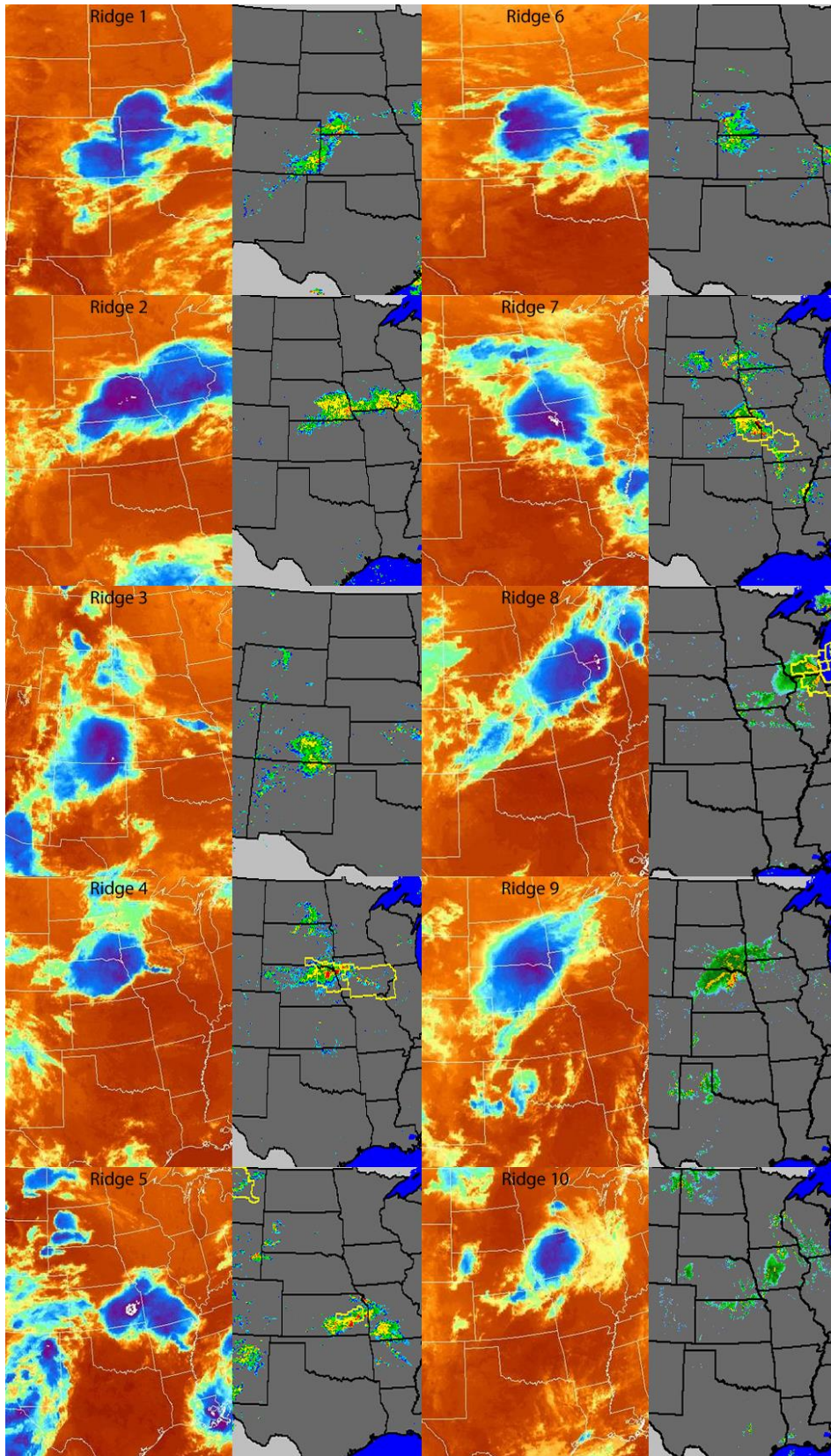Figure B2: As in Fig. B1, but for the zonal (n = 6) cases (Table A2). *Click image to enlarge.*

<u>Figure B3</u>: As in Fig. B1, but for the subset (n = 10) of ridge cases (Table A3). *Click image to enlarge*.

APPENDIX C
Qualitative QG analysis
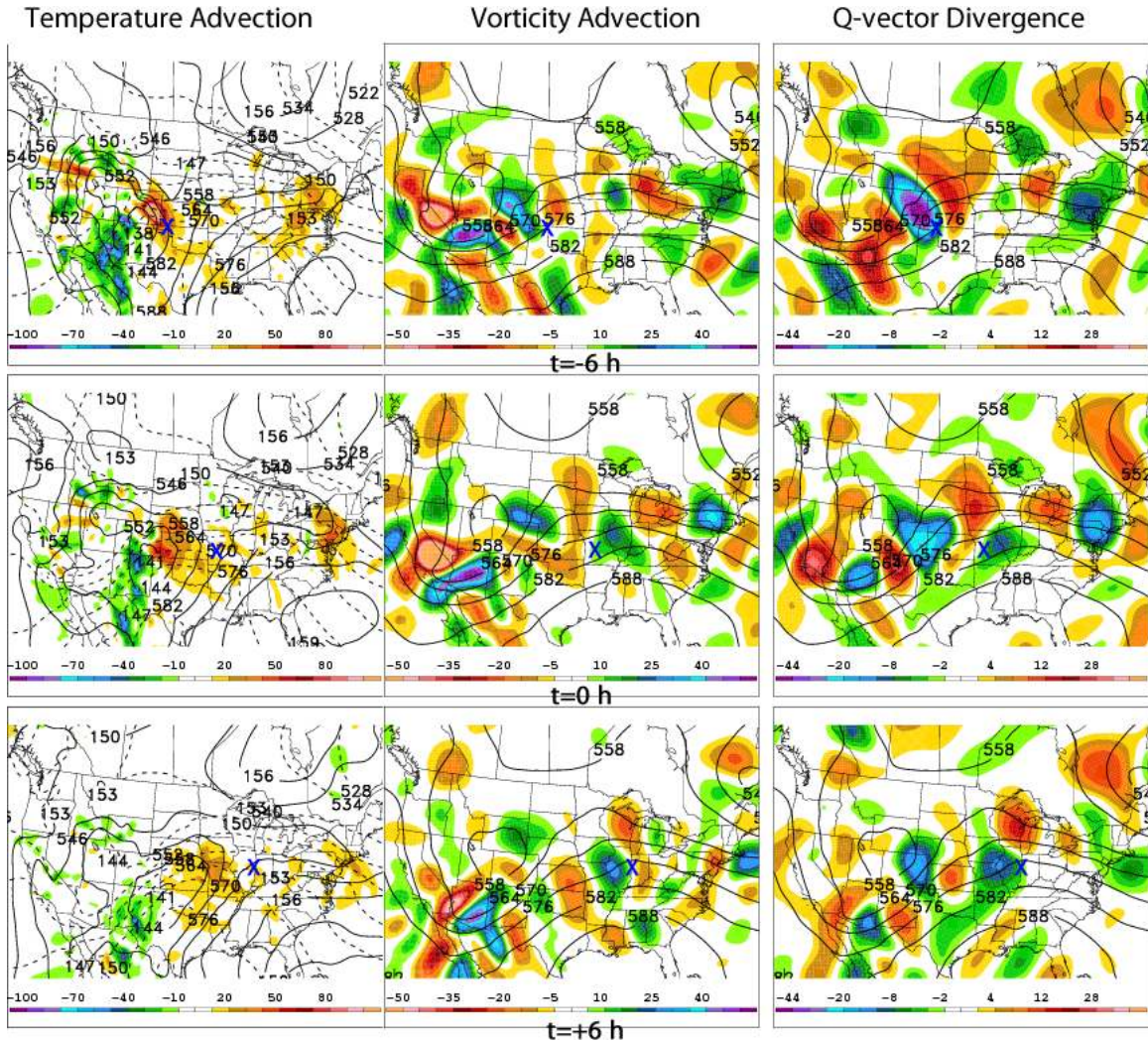
Figure C1: For the sample upstream trough case in Fig. 2a at t = −6 h (top row), t = 0 h (middle row), and t = 6 h (bottom row):

Left: NARR 850–700 hPa layer-averaged geostrophic temperature advection ($\times 10^{-5}$ K s^{-1}, shaded cool colors for cold-air advection, warm colors for warm-air advection), 850-hPa geopotential height (dam, contoured), and 1000–500 hPa thickness (dam, dashed).

Middle: NARR 700–400 hPa layer-averaged geostrophic absolute vorticity advection ($\times 10^{-10}$ K m^{-2} s^{-1}, shaded cool colors for CVA, warm colors for AVA) and 500-hPa geopotential height (dam, contoured) Because lower-tropospheric vorticity advection is typically small, midtropospheric vorticity advection can be considered representative of differential vorticity advection (Eq. 1).

Right: NARR 850–500 hPa layer-averaged Q-vector divergence ($\times 10^{-16}$ K m^{-2} s^{-1}, shaded cool colors for convergence, warm colors for divergence) and 500-hPa geopotential height (dam, contoured).

Click image to enlarge.
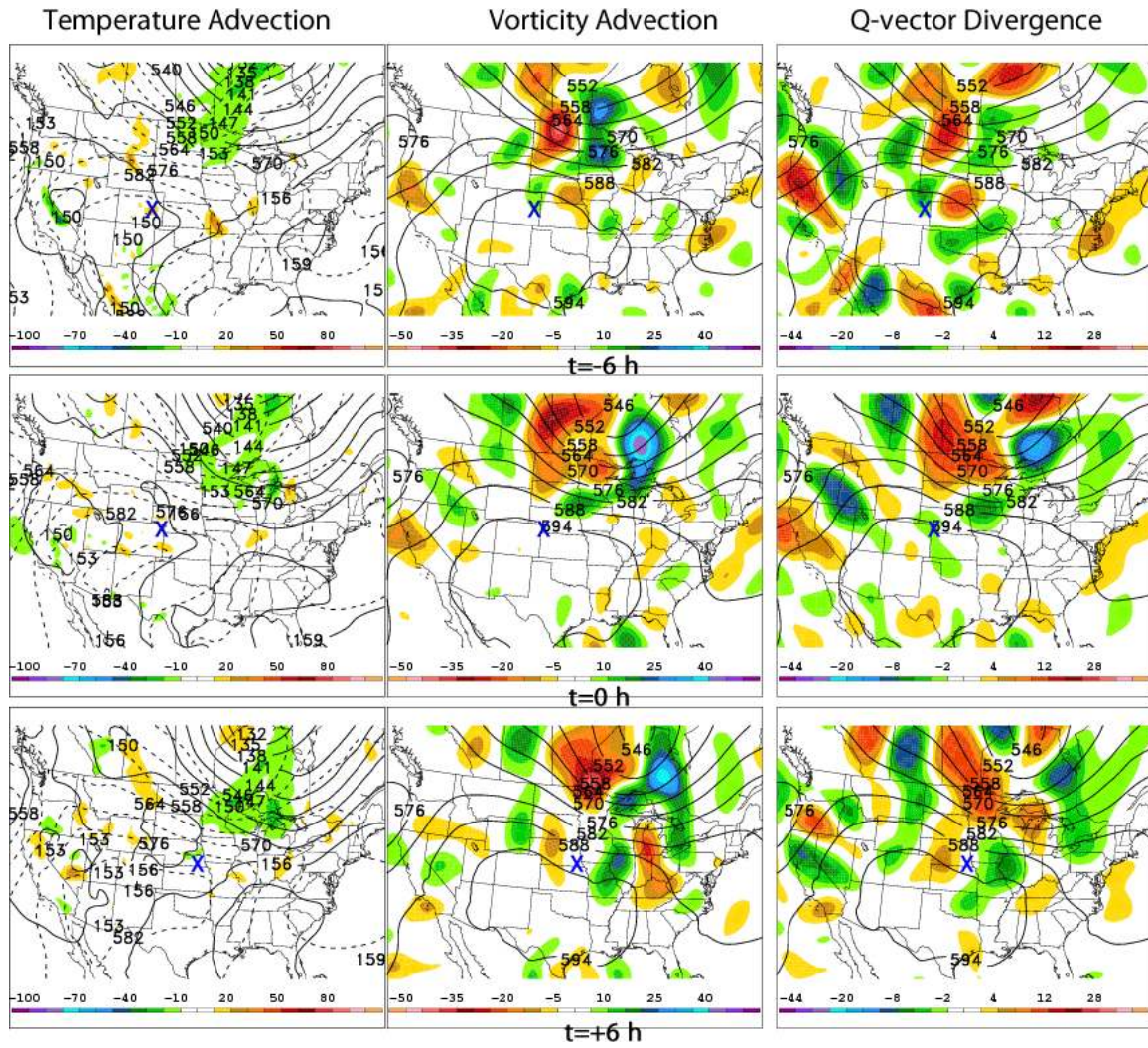
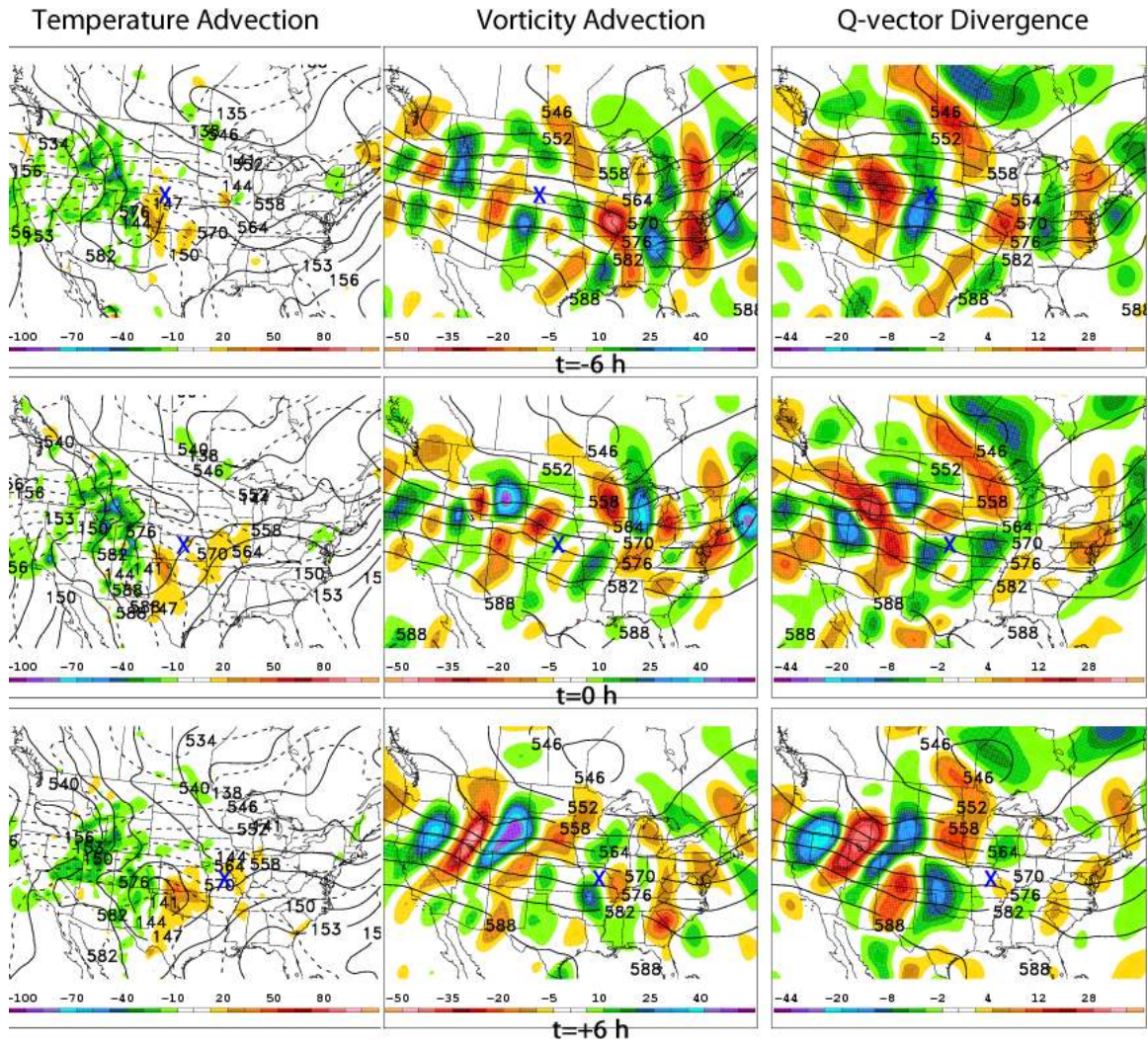Figure C2: As in Fig. C1, but for the sample zonal case in Fig. 2b. *Click image to enlarge*.

Figure C3: As in Fig. C1, but for the sample ridge case in Fig. 2c. *Click image to enlarge*.

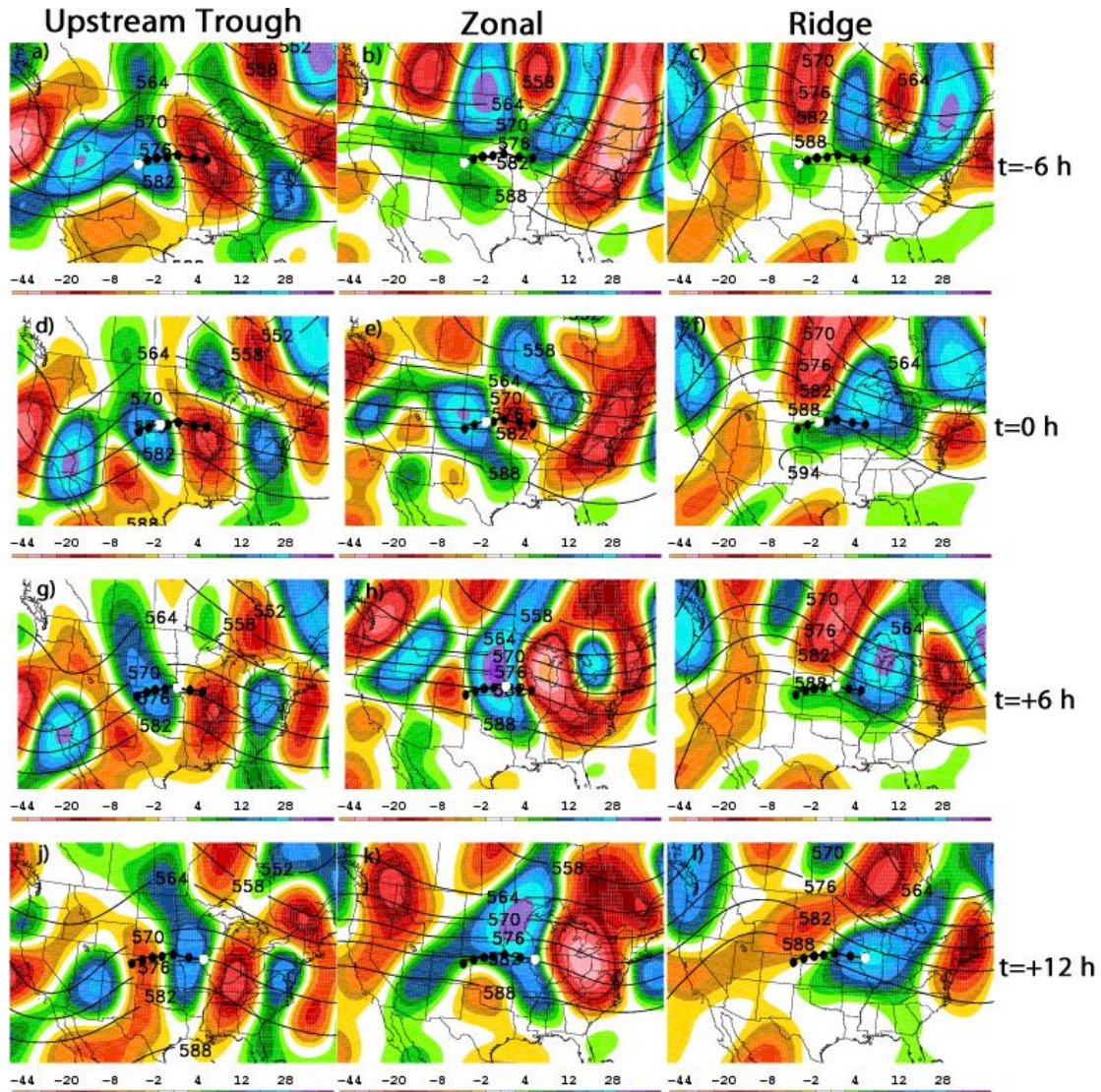Figure C4:   As in Fig. 11, but for NARR 700–400 hPa layer-averaged geostrophic absolute vorticity advection ($\times 10^{-10}$ K m^{-2} s^{-1}, shaded cool colors for CVA, warm colors for AVA) and 500-hPa geopotential height (dam, contoured).   Because lower-tropospheric vorticity advection is typically small, mid-tropospheric vorticity advection can be considered representative of differential vorticity advection (Eq. 1). *Click image to enlarge.*

REFERENCES

Ahrens, C. D., 2008: *Meteorology Today: An Introduction to Weather, Climate and the Environment.* 9th Ed.. Brooks/Cole, 549 pp.

Alpert, P., I. Osetinsky, B. Ziv, and H. Shafir, 2004: Semi-objective classification for daily synoptic systems: Application to the Eastern Mediterranean climate change. *Int. J. Climatol.*, **24**, 1001–1011.

Anderson, C. J., and R. W. Arritt, 1998: Mesoscale convective complexes and persistent elongated convective systems over the United States during 1992 and 1993. *Mon. Wea. Rev.*, **126**, 578–599.

Ashley, W. S., and Coauthors, 2003: Mesoscaleconvective complex rainfall in the United States. *Mon. Wea. Rev.*, **131**, 3003–3017.

Atallah, E. H., L. F. Bosart, and A. Aiyyer, 2007: Precipitation distribution associated with landfalling tropical cyclones over the Eastern United States. *Mon. Wea. Rev.*, **135**, 2185–2206.

Augustine, J. A., and K. W. Howard, 1988: Mesoscale convective complexes over the United States during 1985. *Mon. Wea. Rev.*, **116**, 685–701.

——, and F. Caracena, 1994: Lower tropospheric precursors to nocturnal MCS development over the central United States. *Wea. Forecasting*, **9**, 116–135.

Blamey, R. C., and C. J. C. Reason, 2012: Mesoscale convective complexes over southern Africa. *J. Climate*, **25**, 753–765.

Blanchard, D. O., 1990: Mesoscale convective patterns of the southern High Plains. *Bull. Amer. Meteor. Soc.*, **71**, 994–1005.

Bluestein, H. B., 1992: *Synoptic-Dynamic Meteorology in Midlatitudes: Volume I.* Oxford University Press, 431 pp.

Bosart, L. F., and F. Sanders, 1981: The Johnstown flood of July 1997: A long-lived convective system. *J. Atmos. Sci.*, **38**, 1616–1642.

Coniglio, M. C., J. Y. Hwang, and D. J. Stensrud, 2010: Environmental factors in the upscale growth and longevity of MCSs derived from Rapid Update Cycle analyses. *Mon. Wea. Rev.*, **138**, 3514–3539.

——, S. F. Corfidi, and J. S. Kain, 2011: Environment and early evolution of the 8 May 2009 derecho-producing convective systems. *Mon. Wea. Rev.*, **139**, 1083–1102.

Corfidi, S. F., J. H. Merritt, and J. M. Fritsch, 1996: Predicting the movement of mesoscale convective complexes. *Wea. Forecasting*, **11**, 41–46.

Cotton, W. R., R. L. George, P. J. Wetzel, and R. L. McAnelly, 1983: A long-lived mesoscale convective complex. Part I: The mountain-generated component. *Mon. Wea. Rev.*, **111**, 1893–1918.

——, M. S. Lin, R. L. McAnelly, and C. J. Tremback, 1989: A composite model of mesoscale convective complexes. *Mon. Wea. Rev.*, **117**, 765–783.

Draxler, R. R. and Rolph, G. D., 2012. HYSPLIT (HYbrid Single-Particle Lagrangian Integrated Trajectory) model. NOAA Air Resources Laboratory, Silver Spring, MD. [Available online via http://ready.arl.noaa.gov/HYSPLIT.php.]

Durkee, J. D., and T. L. Mote, 2010: A climatology of warm-season mesoscale convective complexes in subtropical South America. *Int. J. Climatol.*, **30**, 418–431.

——, T. L. Mote, and J. M. Shepherd, 2009: The contribution of mesoscale convective complexes to rainfall across subtropical South America. *J. Climate.*, **22**, 4590–4605.

Fritsch, J. M., and R. A. Maddox, 1981a: Convectively driven mesoscale weather systems aloft. Part I: Observations. *J. Appl. Meteor.*, **20**, 9–19.

——, and ——, 1981b: Convectively driven mesoscale weather systems aloft. Part II: Numerical simulations. *J. Appl. Meteor.*, **20**, 20–26.

Garcia-Herrera, R., D. Barriopedro, E. Hernández, D. Paredes, J. F. Correoso, and L. Prieto, 2005: The 2001 mesoscale convective systems over Iberia and the Balearic Islands. *Meteorol. Atmos. Phys.*, **90**, 225–243.

Hernandez, E., L. Cana, J. Diaz, R. Garcia, and L. Gimeno, 1998: Mesoscale convective complexes over the western Mediterranean area during 1990–1994. *Meteor. Atmos. Phys.*, **68**, 1–12.

Hoskins, B. J., I. Draghici, and H. C. Davies, 1978: A new look at the omega equation. *Quart. J. Roy. Meteor. Soc.*, **104**, 31–38.

Hryciw, L. M., E.H. Atallah, S.M. Milrad, and J. R. Gyakum, 2013: A meteorological analysis of important contributors to the 1999–2005 Canadian Prairie drought. *Mon. Wea. Rev.*, in press.

Jirak, I. L., and W. R. Cotton, 2007: Observational analysis of the predictability of mesoscale convective systems. *Wea. Forecasting*, **22**, 813–838.

——, ——, and R. L. McAnelly, 2003: Satellite and radar survey of mesoscale convective system development. *Mon. Wea. Rev.*, **131**, 2428–2449.

Kalnay, E., and Coauthors, 1996: The NCEP/NCAR 40-year reanalysis project. *Bull. Amer. Meteor. Soc.*, **77**, 437–471.

Kane, R. J., C. R. Chelius, and J. M. Fritsch, 1987: Precipitation characteristics of mesoscale convective weather systems. *J. Clim. Appl. Meteor.*, **26**, 1345–1357.

Koch, S., M. DesJardins, and P. Kocin, 1983: An interactive Barnes objective map analysis scheme for use with satellite and conventional data. *J. Appl. Meteor.*, **22**, 1487–1503.

Ladd, J. W., and D. M. Driscoll, 1980: A comparison of objective and subjective means of weather typing: An example from West Texas. *J. Appl. Meteor.*, **19**, 691–704.

Laing, A. G., and J. M. Fritsch, 1993: Mesoscale convective complexes in Africa. *Mon. Wea. Rev.*, **121**, 2254–2261.

——, and ——, 1997: The global population of mesoscale convective complexes. *Quart. J. Roy. Meteor. Soc.*, **123**, 389–405.

——, and ——, 2000: The large-scale environments of the global populations of mesoscale convective complexes. *Mon. Wea. Rev.*, **128**, 2756–2776.

Leary, C. A., and E. N. Rappaport, 1987: The life cycle and internal structure of a mesoscale convective complex. *Mon. Wea. Rev.*, **115**, 1503–1527.

Maddox, R. A. 1980a: An objective technique for separating macroscale and mesoscale features in meteorological data. *Mon. Wea. Rev.*, **108**, 1108–1121.

——, 1980b: Mesoscale convective complexes. *Bull. Amer. Meteor. Soc.*, **61**, 1374–1387.

——, 1983: Large-scale meteorological conditions associated with midlatitude mesoscale convective complexes. *Mon. Wea. Rev.*, **111**, 1475–1493.

——, D. J. Perkey, and J. M. Fritsch, 1981: Evolution of upper tropospheric features during the development of a mesoscale convective complex. *J. Atmos. Sci*, **38**, 1664–1674.

——, D. M. Rodgers, K. W. Howard, 1982: Mesoscale convective complexes over the United States during 1981. Annual summary. *Mon. Wea. Rev.*, **110**, 1501–1514.

McAnelly, R. L., and W. Cotton, 1989: The precipitation life cycle of mesoscale convective complexes over the central United States. *Mon. Wea. Rev.*, **117**, 784–808.

——, and ——, 1992: Early growth of mesoscale convective complexes: A meso-β scale cycle of convective precipitation. *Mon. Wea. Rev.*, **120**, 1851–1877.

Mesinger, F. and Coauthors, 2006: North American regional reanalysis. *Bull. Amer. Meteor. Soc.*, **87**, 343–360.

Miller, D., and J. M. Fritsch, 1991: Mesoscale convective complexes in the western Pacific region. *Mon. Wea. Rev.*, **119**, 2978–2992.

Milrad, S. M., E. H. Atallah, and J. R. Gyakum, 2009: Dynamical and precipitation structures of poleward moving tropical cyclones in eastern Canada, 1979–2005. *Mon. Wea. Rev.*, **137**, 836–851.

——, ——, and ——, 2010: Synoptic typing of extreme cool-season precipitationevents at St. John's, Newfoundland, 1979–2005. W*ea. Forecasting*, **25**, 562–586.

——, ——, ——, and G. Dookhie, 2013: Synoptic-scale precursors and typing of warm-season precipitation events at Montreal, Quebec. W*ea. Forecasting*, submitted.

Moore, J. T., and G. E. Vanknowe, 1992: The effect of jet streak curvature on kinematic fields. *Mon. Wea. Rev*., **120**, 2429–2441.

Muller, R. A., 1977: A synoptic climatology for environmental baseline analysis: New Orleans. *J. Appl. Meteor.*, **16**, 20–33.

——, and A. L. Jackson, 1985: Estimates of climatic air quality potential at Shreveport, Louisiana. *J. Climate and Appl. Meteor.*, **24**, 293–301.

Nachamkin, J. E., R. L. McAnelly, and W. R. Cotton, 1994: An observational analysis of a developing mesoscale convective complex. *Mon. Wea. Rev.*, **122**, 1168–1188.

Overland, J. E., and T. R. Hiester, 1980: Development of a synoptic climatology for the northeast Gulf of Alaska. *J. Appl. Meteor.*, **19**, 1–14.

Rodgers, D. M., K. W. Howard, and E. C. Johnston, 1983: Mesoscale convective complexes over the United States during 1982. *Mon. Wea. Rev.*, **111**, 2363–2369.

——, M. J. Magnano, and J. H. Arns, 1985: Mesoscale convective complexes over the United States during 1983. *Mon. Wea. Rev.*, **113**, 888–901.

Smull, B. F., and J. A. Augustine, 1993: Multiscale analysis of a mature mesoscale convective complex. *Mon. Wea. Rev.*, **121**, 103–132.

Stensrud, D. J., 1996: Importance of low-level jets to climate: A review. *J. Climate*, **9**, 1698–1711.

Trier, S. B., and D. B. Parsons, 1993: Evolution of environmental conditions preceding the development of a nocturnal mesoscale convective complex. *Mon. Wea. Rev*, **121**, 1078–1098.

——, C. A. Davis, and D. A. Ahijevych, 2010: Environmental controls on the simulated diurnal cycle of warm-season precipitation in the continental United States. *J. Atmos. Sci.*, **67**, 1066–1090.

——, ——, ——, M. L. Weisman, and G. H. Bryan, 2006: Mechanisms supporting long-lived episodes of propagating nocturnal convection within a 7-day WRF model simulation. *J. Atmos. Sci.*, **63**, 2437–2461.

Tripoli, G. J., and W. R. Cotton, 1989: Numerical study of an observed orogenic mesoscale convective system, Part I: Simulated genesis and comparison with observations. *Mon. Wea. Rev.*, **117**, 273–304.

Tucker, D. F. and K. S. Zentmire, 1999: On the forecasting of orogenic mesoscale convective complexes. *Wea. Forecasting*, **14**, 1017–1022.

Tuttle, J. D., and C. A. Davis, 2006: Corridors of warm season precipitation in the central United States. *Mon. Wea. Rev.*, **134**, 2297–2317.

Wetzel, P. J., W. R. Cotton, and R. L. McAnelly, 1983: A long-lived mesoscale convective complex. Part II: Evolution and structure of the mature complex. *Mon. Wea. Rev.*, **111**, 1919–1937.

Zhang, D., and J. M. Fritsch, 1987: Numerical simulation of the meso-β scale structure and evolution of the 1977 Johnstown flood. Part II: Inertially stable warm-core vortex and the mesoscale convective complex. *J. Atmos. Sci.*, **44**, 2593–2612

<div align="center">**REVIEWER COMMENTS**</div>

[Authors' responses in *blue italics.*]

REVIEWER A (Russ Schumacher):

Initial Review:

Recommendation: Accept with major revisions.

General comments: In this study, the authors analyze the large-scale environments of mesoscale convective complexes (MCCs). They use both brief case studies and composite analysis to categorize the MCCs into three categories, termed "trough", "zonal", and "orographic". The results show that the cases with a strong upstream trough have stronger quasi-geostrophic forcing for ascent than the other types, and also that the advection of high-θ_e air into the area of the MCC appears to be important in all three types.

This manuscript is well written, clearly states its conclusions, and the figures do a good job of illustrating the primary results. The composite analysis provides a useful distinction between the different types of large-scale conditions that support MCCs. The authors do a very good job of summarizing much of the past literature on MCCs and MCSs, but they do miss several key recent papers that have very strong relevance to this work, and in the context of which this work should be placed. Furthermore, there are some statements made in the manuscript that come across as speculation, but which I imagine could be fairly easily quantified with the existing datasets. As a result, I recommend major revisions for this manuscript and I look forward to reviewing a revised version.

Major Comments: Probably the biggest suggestion I have for revision is to place this work in the context of some important recent work on MCSs and MCCs in the central US. This should not be particularly onerous but is quite important for assessing which results here are novel and which are confirmations of previous studies. There are three sets of articles that I think are particularly relevant to the present manuscript. One is the work of Jirak et al. (2003) and Jirak and Cotton (2007). The 2003 paper is a satellite and radar-based objective climatology of MCCs, and the 2007 paper then develops an index for MCS/MCC development and maintenance based on storm-centered composites. The second is the model-based analysis of Trier et al. (2006,2010). These papers both use somewhat idealized or smoothed large-scale warm-season conditions and investigate the connection between the large-scale conditions and the storm-scale processes governing MCSs. In particular, they point out that in mid-summer (i.e., July/August), the primary role of the low-level jet is not moisture transport but convergence and lift, which is similar to a conclusion reached here for the orographic cases. The third is the paper by Coniglio et al. (2010), which uses reanalysis data for a large number of MCS cases to discriminate between the conditions supporting and inhibiting upscale growth and maintenance. I don't think that any of the results of the current manuscript are in contradiction to these previous studies, but there are numerous places in this manuscript where the similarity to these previous works should be noted.

Thanks very much for the suggestion of the recent papers, they were enlightening and helped put our work into better context. We have inserted references throughout the text to the Jirak et al. papers, the Trier et al. papers, and the Coniglio et al. papers, including throughout the synoptic analysis section (putting our results into the context of their results). One major thing that we have added as a result of reading the papers that you suggested is 1000–700 hPa frontogenesis contours to our 850-hPa/LLJ plots; several of the papers you cited discuss the LLJ and its impact on ascent (in addition to moisture/instability), and we felt that this was a good way to discuss that. In addition, the new duration and identification section (section 3c, Appendices A and B) speaks to some of the issues with just using a satellite-based identification scheme (Bob Maddox brought this point up as well). Our results have not really changed, but we feel that they are more robust with these revisions.

The categorization scheme for the large-scale flow conditions makes sense to me and the differences between the three types are clear in the individual cases and the composites. However, I have a couple of suggestions for perhaps further strengthening the classification and analysis. First, I might suggest that the

"trough" category be renamed "upstream trough" or something similar, as the current name might lead the reader to believe that the MCCs are taking place near a trough, when in fact they mature very near the axis of the ridge! Clearly the ascent forced out ahead of the trough is a key factor in these cases, and this is mainly just a semantic/readability suggestion. The difference between the "orographic" type and the other two types is made quite clear as well, but it does suggest that orographic effects are not important in the trough or zonal categories, when I suspect that they might be, at least in some cases. Since many of the trough and zonal cases also originate near the Rockies, it would seem that the mountains play some role in these synoptic patterns as well. Perhaps some comment on this would be warranted.

Again, well-taken suggestions. We have renamed two of the groups throughout the paper: "trough" is now "upstream trough", and "orographic" is now "ridge". The change to "upstream trough" is done for the reason that you mentioned, as the longwave trough remains upstream for the entire evolution of both the composite and individual case MCCs. The change to "ridge" is a) so as not to confuse the reader by suggesting that no zonal or upstream trough cases formed near/in the Rockies (as you noted, a couple of zonal cases did, and we now note this in the paper), and b) because "ridge" makes more sense, as the typing is based on 500-hPa height patterns. In reality, you do not see anything "orographic" on a 500-hPa height chart, you see either a trough, ridge, or zonal flow.

Finally, I wonder whether there were any MCC cases in the database that didn't nicely fit one of these three categories. [The forceful argument by Doswell et al. (1991) for an "unclassified" category in taxonomic studies comes to mind.]

We went back and double-checked this. From 6 years of data (2006–2011), there were 7 borderline zonal/trough or zonal/ridge cases that we did not classify. We have added mention of this to section 3b (on page 6). We now explain in the text that the percentage of systems unable to be classified was extremely small. In fact, that was one of the original motivations for using the 500-hPa height partitioning: it was extremely neat and may be reproduced easily.

There are a few points that are brought up throughout the manuscript that the authors speculate might be true, but which could probably be easily confirmed with the datasets already being used. One is regarding the longevity of the different classes of MCCs: since the authors have already identified the locations and tracks of all the MCCs being studied, shouldn't it be possible to also present the longevity of each of the MCCs? (And then calculate the median, mean standard deviation, etc., for each of the subsets.) This is brought up in a few places in section 4b2, for example at the end of page 13.

We have added section 3c, which details the duration statistics for all three event groups. The new associated table is now called "Table 5", and Appendix A contains related information for each case in the study.

Similarly, the relative importance of the vorticity advection term compared with the thermal advection term of the omega equation is one of the key results of the manuscript, however the actual magnitude of the vorticity advection term is never explicitly shown for either the individual cases or the composites. As the authors point out, it's pretty obvious that there's stronger CVA in the trough pattern than the other two patterns, but I wonder if actually calculating the vorticity advection to go along with the temperature advection for each type might reveal some interesting patterns.

We have added a vorticity advection analysis, and we feel it makes our results (and discussion) much more robust. The new (700-400 hPa) vorticity advection figures are contained in Appendix C, and we include them in our QG forcing analysis (for both the case studies and composites, throughout section 4)

[Minor comments omitted...]

Second review:

Recommendation: Accept.

General Comments: I have now completed my review of "Synoptic-scale precursors, characteristics, and typing of nocturnal Mesoscale Convective Complexes in the Great Plains" for E-Journal of Severe Storms Meteorology, and submitted my recommendation, "Accept Submission."

REVIEWER B (Edward J. Szoke):

Initial Review:

Reviewer recommendation: Accept with minor revisions.

General comments:

Author's note: Per Russ Schumacher's, suggestions and after careful consideration, we have renamed our "trough" cases as "upstream trough" and our "orographic" cases as "ridge" cases, to better reflect the patterns seen in the 500-hPa height field.

The main concerns are outlined in the substantive comments section. Basically they amount to the following:

1) Authors need to be a bit careful in overstating some of the conclusions regarding forcing (or lack thereof) since compositing will tend to smooth out smaller scale features. So what might be appropriate on the synoptic scale may not apply to smaller, mesoscale features, which can be critical.

See specific comments in the technical comments section.

2) Speculation is made about upper-level forcing based on jet stream quadrant arguments and likely vorticity advection patterns. I kept thinking though, why not actually use the QG diagnostics to go ahead and calculate QG forcing for, say, the 200–400-hPa layer? Then one could remove some of the speculations.

See comments below in the technical comments section.

3) But one could add a little speculation concerning the orographic cases. These are probably dominated by systems coming out of the SW monsoon flow into the southern and central Rockies, and as such may be more organized when they emerge from the Rockies then the more convective-scale phenomenon for the other two categories. Maybe not MCC category, but MCS at least in many cases. Something worth mentioning and certainly makes it interesting to consider this as a separate category, as you have.

See our new section on satellite and radar analysis (as requested by another reviewer). At least a few of the ridge cases do appear to be associated with typical SW monsoon radar observations. We have added mention of this to the last sentence in section 3b, as well a brief discussion of it in the radar analysis portion of section 3c, and in the conclusions (section 5).

Substantive comments:

"By t = 0 h (Fig. 3d) and t = +6 h (Fig. 3f), the MCC has moved downstream of the strongest Q-vector convergence and just downstream of a shortwave 500-hPa ridge axis (Fig. 3d). This places the MCC in a region of both 500-hPa anticyclonic vorticity advection (AVA) and Q-vector convergence at t = 0 h (Fig. 3d) and t = +6 h (Fig. 3f)". This is a bit confusing since in the first sentence you state it is downstream of the Q-vector conv, then say it is in an area of Q-vector convergence (which it is, but a new, separate area). You simply say something like "…This places the MCC in a region of both 500-hPa anticyclonic vorticity advection (AVA) and a new area of Q-vector convergence …" and I think this would help, and leads to your argument at the end of this paragraph (where you could again say something like "new area of Q-vector convergence" if you want.

Agree, this wording was very confusing. Per Russ Schumacher's suggestion, we have added vorticity advection diagnostics for each case and placed them in Appendix C. This enables the reader to see the evolution of both the vorticity and temperature advection, in addition to the Q-vector divergence. Thus, instead of making QG forcing conclusions based on the 500-hPa height structures alone, we now qualitatively discuss each term in the QG omega equation. Much of the synoptic-scale analysis (section 4) has been rewritten. The conclusions are generally the same, but we think the descriptions are much improved.

"Thus, we can conclude that unlike in the trough case, WAA is the only QG mechanism for ascent throughout the life of the zonal case." There certainly could be an embedded shortwave within a mostly zonal flow, and I don't think you can state this with such certainty. Perhaps you could say WAA is the primary synoptic scale ascent mechanism, but certainly not for smaller scales. It should also though be noted that your choice of the 850–500-hPa layer for QG calculations might preclude seeing higher level forcing (such as with a jet streak, where a choice of 400–200 hPa might have been more appropriate). Later in this discussion you note the presence of CAA at t = +6h, but I only see lack of WAA in the figure, at least at the coloring contours shown. Maybe I am not seeing weak CAA?

See the response to #2 above. The vorticity advection analysis has eliminated the ambiguity in our QG forcing statements, at least on the synoptic scale. Also, we have changed the wording throughout such that when we refer to one mechanism being stronger (or weaker) than the other, we emphasize that we can only come to such conclusions on the synoptic scale (which is our primary objective here anyway).

"…we suggest that non-QG ascent mechanisms may be in play, specifically the equatorward entrance region (Fig. 7a,c) of the jet streak" — one could address such forcing with QG diagnostics but for a higher layer near the jet, so calling this a "non-QG ascent mechanism" is not correct. In fact, I think your analyses would benefit from such a calculation, since you are often referring to (but not diagnosing) differential vorticity advection and jet streak dynamics.

Firstly, our original wording was rather sloppy and confusing. By "non-QG mechanisms", we meant mechanisms that are not represented in the Q-vector form of the QG omega equation (i.e. not CVA or WAA for ascent). By rewording most of this section and adding the vorticity advection analysis, a lot of the confusion and ambiguity has been removed. We have also added the following statement to section 4a3: "We thus suggest that ascent mechanisms not represented by Eq. (2) may be in play for the ridge case. Specifically, enhanced upper-level divergence in the equatorward entrance region of the jet streak (Fig. 7a,c) and low-level upslope flow may both contribute to the synoptic-scale ascent necessary to generate the MCC."

Secondly, to your point about the levels chosen for the Q-vector divergence (layer-averaged 850–500 hPa): We went ahead and computed plots as in Figs. 3, 5, and 7, but for both 400–200 hPa (layer-averaged) Q-vector divergence and 850–200 hPa (layer-averaged) Q-vector divergence. These sample figures are pasted below. You will notice that the sign of the Q-vector divergence is the same no matter what level is chosen, but the magnitude is strongest when the 850–500 hPa layer is used. In our experience, 850–500 hPa Q-vector divergence consistently produces the best (qualitative) match with explicit omega values from the reanalysis. The overwhelming majority of the Q-vector divergence seems to always be in the lower to mid-troposphere. We have added a sentence shortly after we define Eq. (2) that states that we experimented with other layers, and found the 850–500 hPa layer to be representative of what we are trying to show. We have referenced one of our recent accepted papers (Hryciw et al. 2013) to provide a citation for this statement.
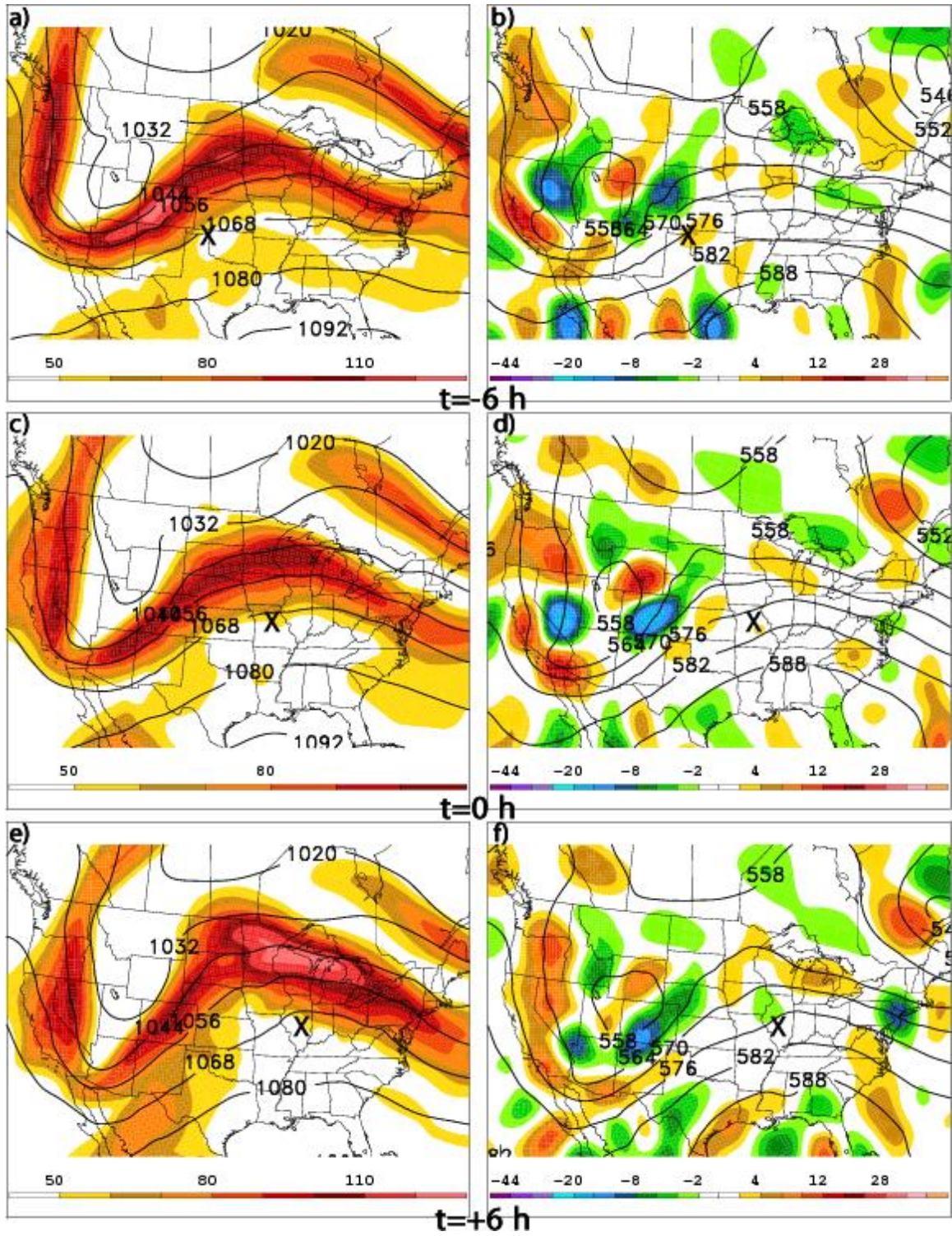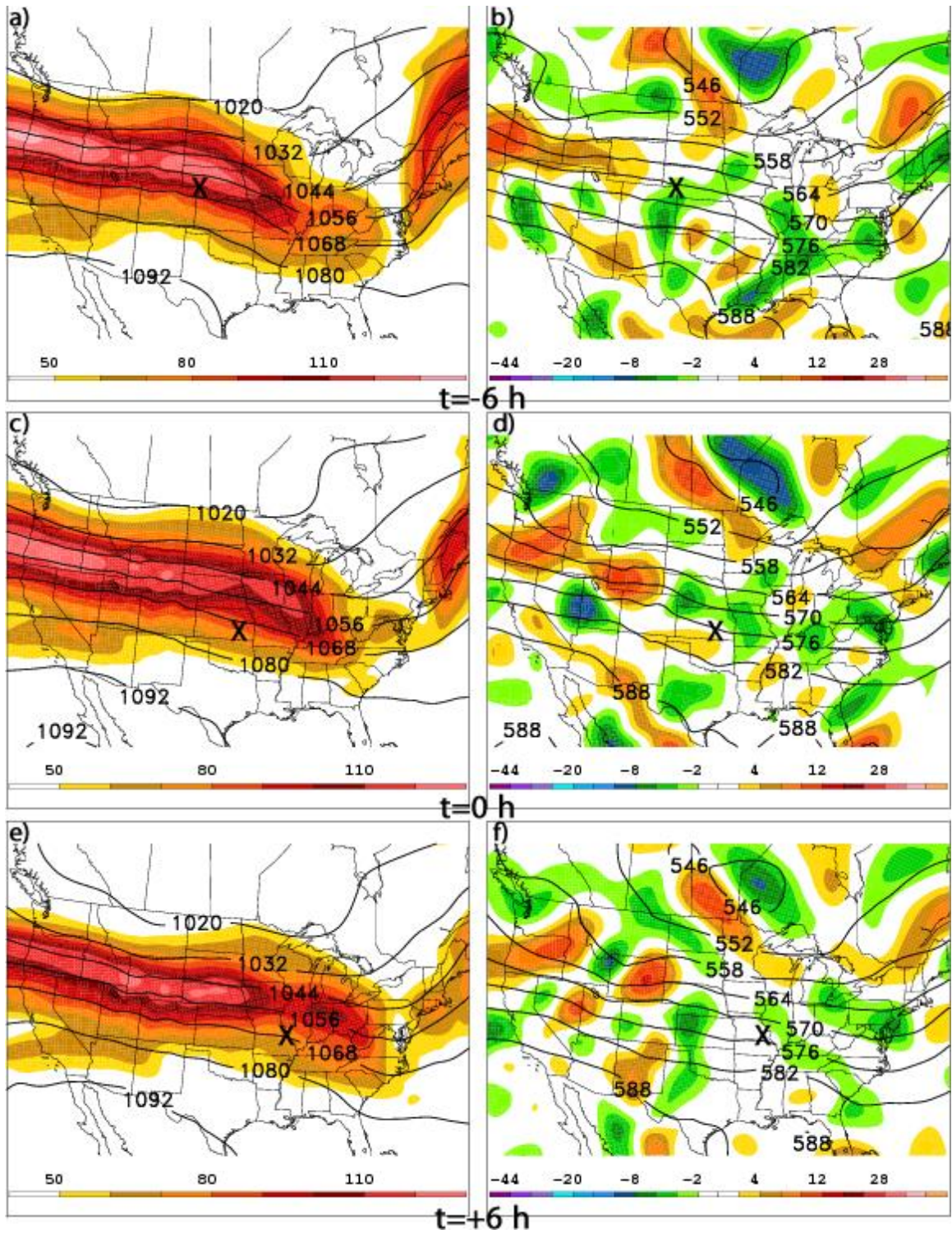
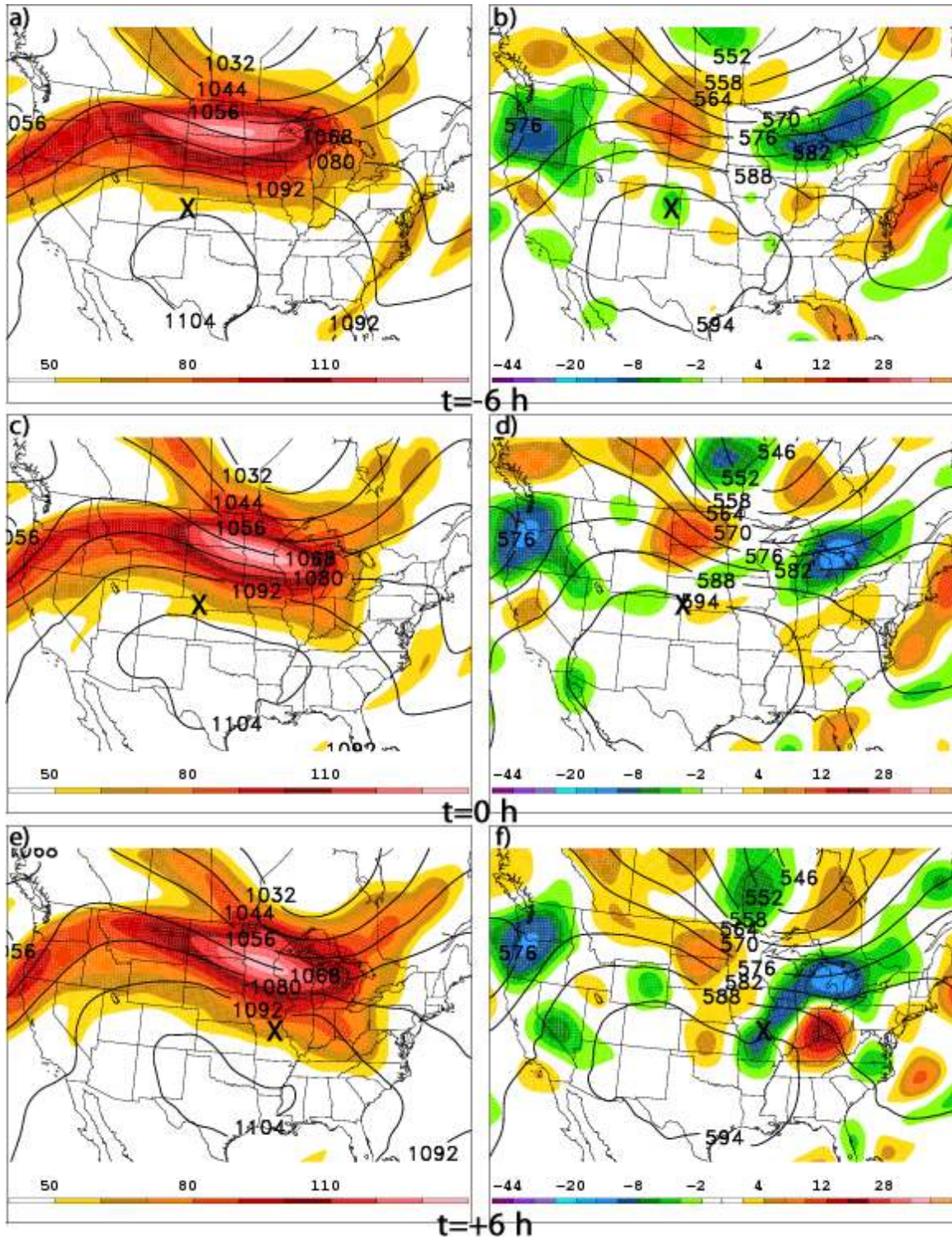*As in Fig. 3, but for 400–200 hPa Q-vector divergence in the right-hand panels.*
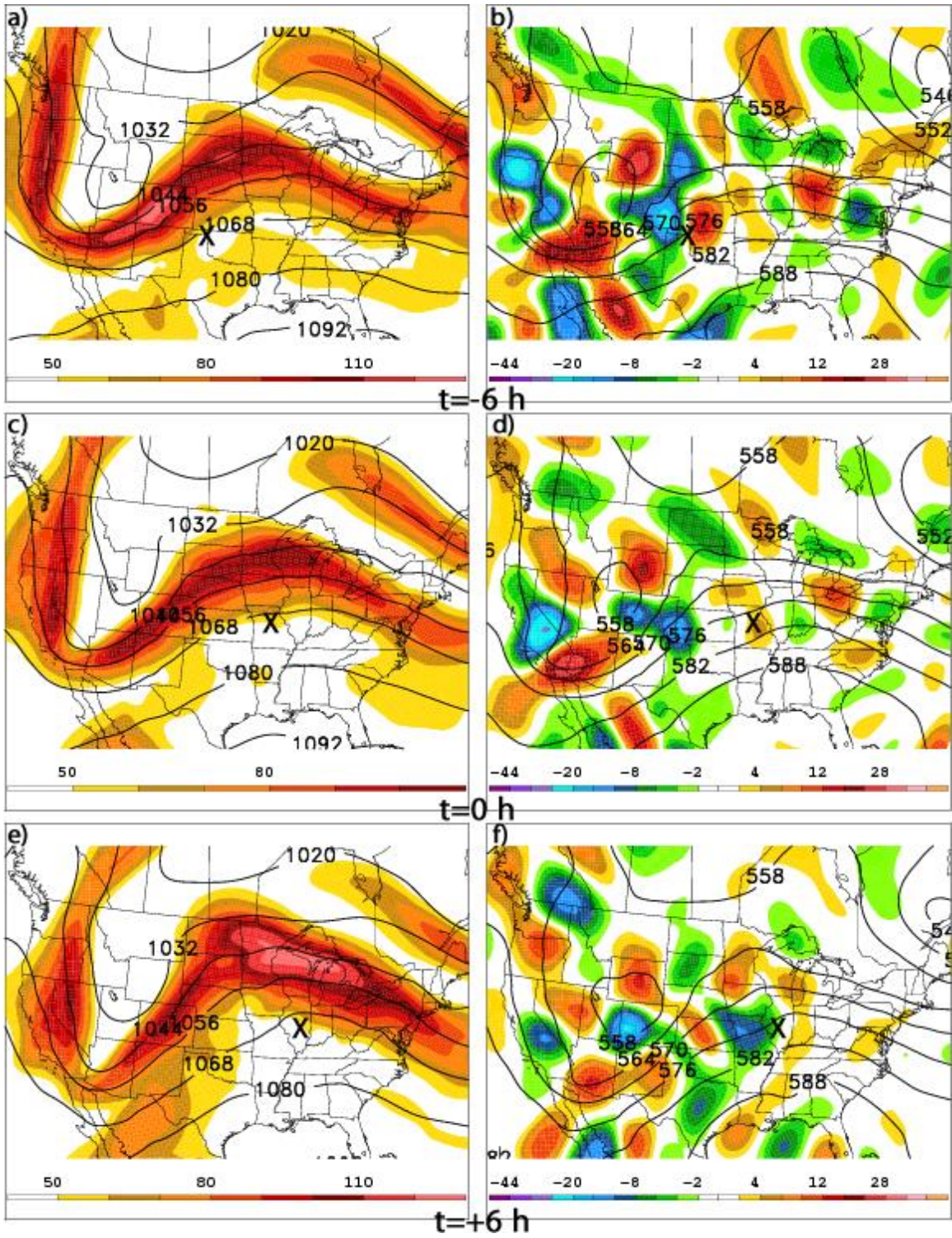
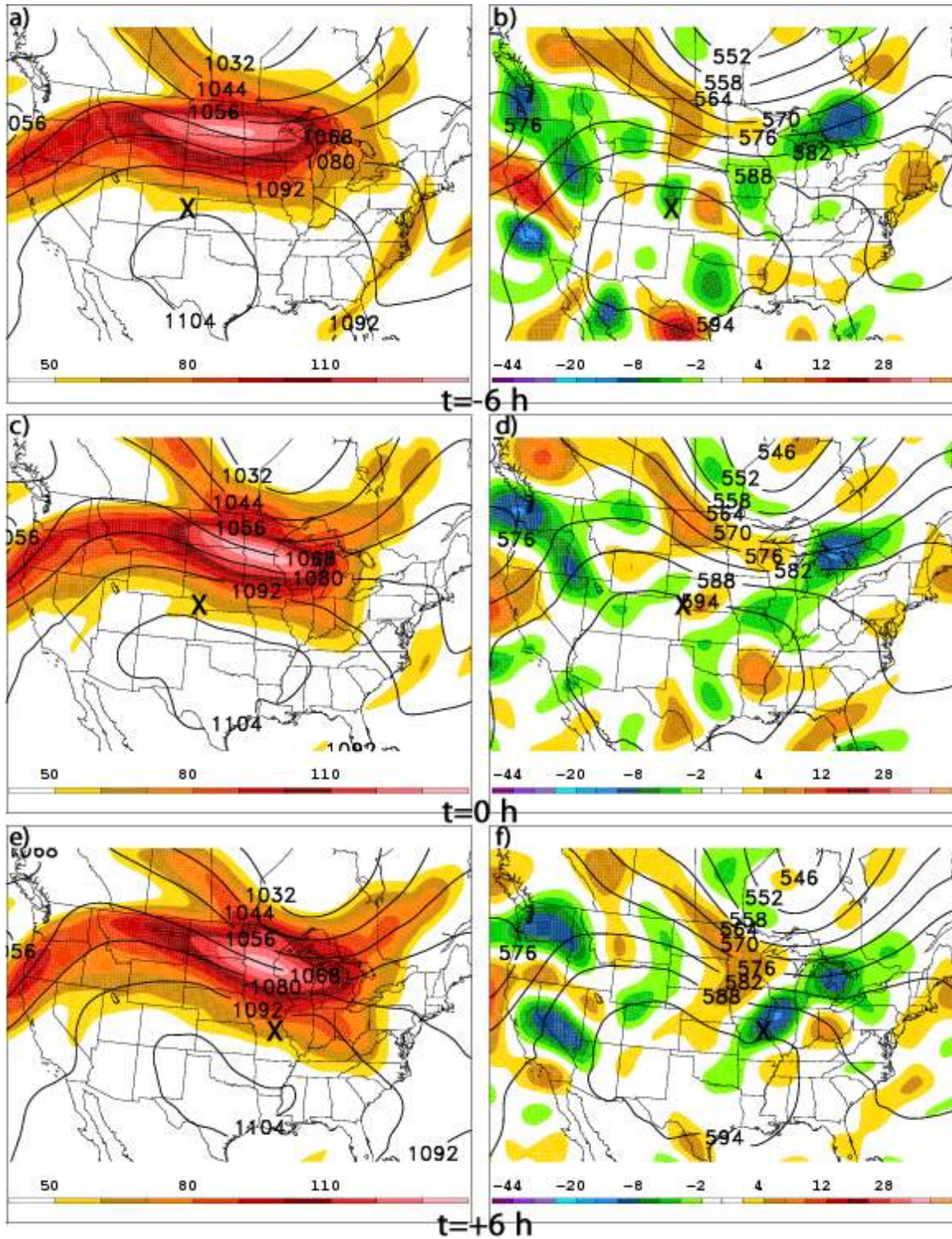*As in Fig. 3, but for 850-200 hPa Q-vector divergence in the right-hand panels.*
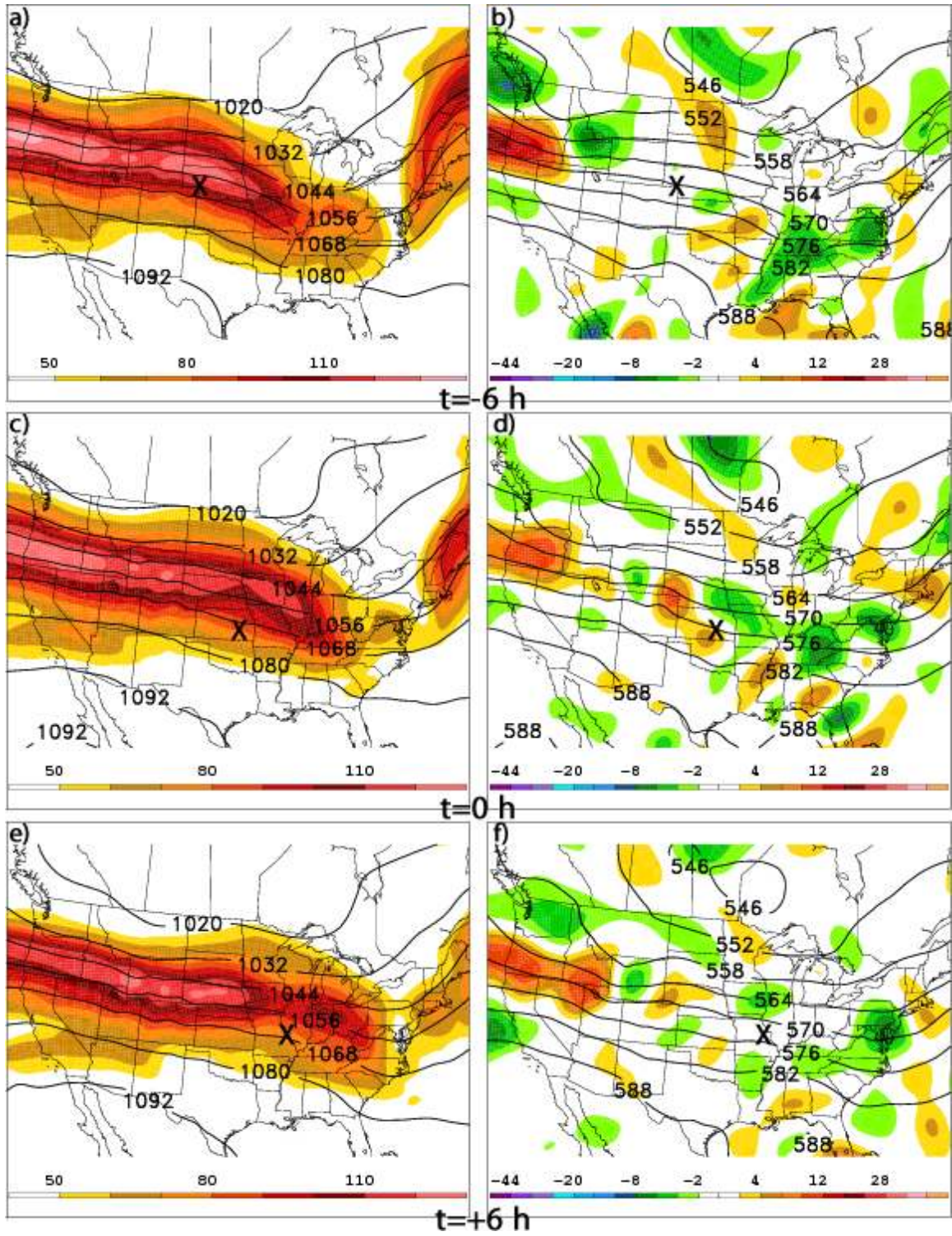
As in Fig. 5, but for 400-200 hPa Q-vector divergence in the right-hand panels.

As in Fig. 5, but for 850-200 hPa Q-vector divergence in the right-hand panels.

As in Fig. 7, but for 400-200 hPa Q-vector divergence in the right-hand panels.

As in Fig. 7, but for 850-200 hPa Q-vector divergence in the right-hand panels.

[Minor comments omitted...]

Second Review:

Reviewer recommendation: Accept with minor revisions.

General comments: I believe the authors have done a nice job addressing the concerns of the reviewers, and my comments are generally minor at this point. A nice addition might be to expand Table 5 to include all the cases (perhaps as an additional grouping for each). Then you wouldn't be "wasting" all these cases, and it would also be a nice check on how representative the other cases are. Otherwise checking on the Figure 5/C2 comparison should be done.

[Minor comments omitted...]

REVIEWER C (Robert A. Maddox):

Initial Review:

Recommendation: Accept with major revisions.

General comments:

Author's note: Following Russ Schumacher's suggestion, after careful consideration we have renamed our "trough" cases as "upstream trough" and our "orographic" cases as "ridge" cases, to better reflect the patterns seen in the 500-hPa height field (see response to Reviewer A substantive comment #2)

The authors have identified MCCs for their study using only the satellite definition from almost 40 years ago. As Reviewer B remarks this was indeed back in the "dark ages," w.r.t. both observations and modeling. The satellite perspective captures only the nature of the anvil cloud associated with the convective system. Since numerous studies have since shown there to be a wide spectrum of convective structures associated with nearly circular anvils [e.g., see Blanchard (1990) and Jirak et al. (2003) reference provided by Reviewer A], an important question arises: Can a study such as this be done today without some consideration of the internal structures indicated by modern radar data? The character of the MCCs considered is quite important, since some can be derechos (your case of 8 May 2009) with long tracks and fast movement and others can be slow-moving, heavy rain producers. The tracks of the MCCs considered (Fig. 10) seem to indicate that using only satellite data to follow system evolution has led to some problems (i.e., a number of very erratic tracks). Do each of your three synoptic patterns tend to support MCCs having different internal and severe weather characteristics? I suspect that your "zonal" pattern favors derechos.

The references you mentioned (and cited by Reviewer A) as well were enlightening in this regard. We have added those references, and created Appendix B, which shows snapshots of IR satellite and composite radar reflectivity at the time of maximum extent (see Appendix A) for each case. A discussion of the different structures beneath the circular anvils in now included in section 3c (including the fact that a few zonal cases are obvious derechos). Since the reproducible element of our study is our synoptic partitioning (based on the 500-hPa heights), we do not feel that the different underlying radar structures change the basis for our study. However, it does bring up an interesting point regarding semantics: that is, should we keep the 'MCC' name based on satellite imagery alone, or use the more general 'MCS' name (which many recent studies have adopted)? We discuss this fairly extensively in section 3c. For now, we have kept the MCC name, to differentiate from squall lines. While the radar structures do show some PECS'-type events along an east–west axis, none of our cases fit the traditional north–south squall line appearance. We think it makes an interesting point in itself that all cases have circular anvils (i.e. fit the original MCC criteria), but have different underlying structures.

Finally, we also make the point in section 3c that several cases take different forms at different times in their lifecycles; this perhaps justifies the 500-hPa height classification system even more, since it is more easily reproducible than trying to categorize events based on radar imagery.

Use of the –32°C criteria in the MCC definition. This criterion was included in the original work because of efforts at NESDIS to do operational satellite rainfall estimation. Scofield and colleagues there had developed an IR procedure that began accumulating rainfall at –32°C. The later work dropping the –32°C part of the definition fit better with the reality of actual surface observations under MCCs. Augustine developed an automated technique that keyed only on the –52°C part of the definition (his procedure was used by authors of some of the references recommended by reviewer A).

Using the –32°C temperature contour in the definition usually becomes messy and I don't find any explanation of how you dealt with this. Consider the situation shown in your Fig. 1. There are two MCSs over Kansas and Missouri. The eastern one becomes your MCC case, while the trailing MCS moves northeastward behind the MCC. However, the –32°C contour connects both MCSs—how did you resolve this ambiguity? The orographic case chosen seems to be a very marginal MCC since two distinct convective clusters are apparent, since the cold cloud shield appears elongated, and since the size appears to be small.

A look at Doswell (1980) might be useful w.r.t. your orographic category.

Reviewer A made this point as well, and we have taken the suggestion, changing the appropriate tables, and mentioning that Augustine and Howard (1988) updated the criterion. It does not change our results, but it fits better with recent studies.

As for the specific issues you mention with the cases in Fig. 2:
- *For the upstream trough case, we essentially ignored the trailing MCS and considered the two features separate systems. The circular feature in front was the one that first met the MCC criteria. The removal of the –32°C criterion should take care of this issue either way.*
- *For the ridge case, it was actually a small mistake in Fig. 2; the previous image was 0.5 hours earlier than the correct t = 0 h image (and thus the system appeared small). We have inserted the correct image into the revised version of Fig. 2.*

You state that you wanted "…to create similar numbers of cases…", but have ended up with 12, 10 and 5 cases. It seems that you should consider expanding your sample of "zonal" events.

We have added 1 case to the zonal composite (the full total from 2006–2011). Our results do not change much if at all by adding the one case. We realize that six is a bit low for a composite analysis, but there simply are not any more zonal cases in our study period (2006–2011), and we did not want to compromise our methodology by considering borderline cases. We should note that we have used as little as five cases in synoptic compositing used for published peer-reviewed journal articles in the past.

The "Xs" for t–6h, t = 0h, and t+6h shown for your three case examples do not match with the tracks for these events shown in Fig. 10. For example, consider the zonal case, shown in Fig. 5, where the "Xs" move from southwest Nebraska at t–6h, to east Kansas at t = 0 and then to eastern Missouri. But in Fig. 10 the t–6h position is shown to be over central Colorado, a substantial difference w.r.t. the t–6h forcing. The discrepancies are even greater for the trough and orographic cases.

We went back and double-checked. The tracks in Fig. 10 were/are correct, but the Xs were not (in panels of other figures), with one exception (t = –6 h in the upstream trough case, where the t = –6 h point on the Fig. 10 track was too far east). All the appropriate figures have been corrected and the discussion of the synoptic-scale features has been edited to reflect the correct positions.

Low-level jet issues: Reviewer A has remarked about the inertial oscillation component of the LLJ and this is an important aspect of the diurnal cycle that needs to be mentioned. The inertial oscillation leads to a situation where thermal advection at low-levels is sub-geostrophic during late afternoon but super-geostrophic by midnight and later, when the daytime BL has decoupled from the surface. During summer the oscillation produces a wind regime within the Plains boundary layer that tends to be divergent during the afternoon and convergent during the night. Are these ageostrophic effects significant when compared to your geostrophic computations?

Computing thermal advection for the 850–700 hPa layer can be problematic, since 850 is often in the boundary layer (or decoupled BL); whereas 700 hPa is often in an elevated mixed layer. I note that the sense of thermal advection at 850 hPa for your orographic example seems completely out of phase with the 700-hPa advection. I recommend taking a look at some of the actual sounding data for your cases so that you get a feel for how the NARR has done with these events. This might be especially important for your orographic example, which may have some significant problems. This is very easy to do at the University of Wyoming upper-air site.

Following your comments, we experimented with two different layer-averaged calculations for all three cases (and the composites). We show the case plots below (they are representative of the composites): The first set is for the 850–500 hPa (layer-averaged) temperature advection, and the 2ⁿᵈ set is for the 700–400 hPa (layer-averaged) temperature advection. As you will see, the differences are extremely minimal. If anything, our original 850–700 hPa results are slightly more robust than the other two layers. We have added mention of this to the paper in section 4a, right after we present the QG equations.
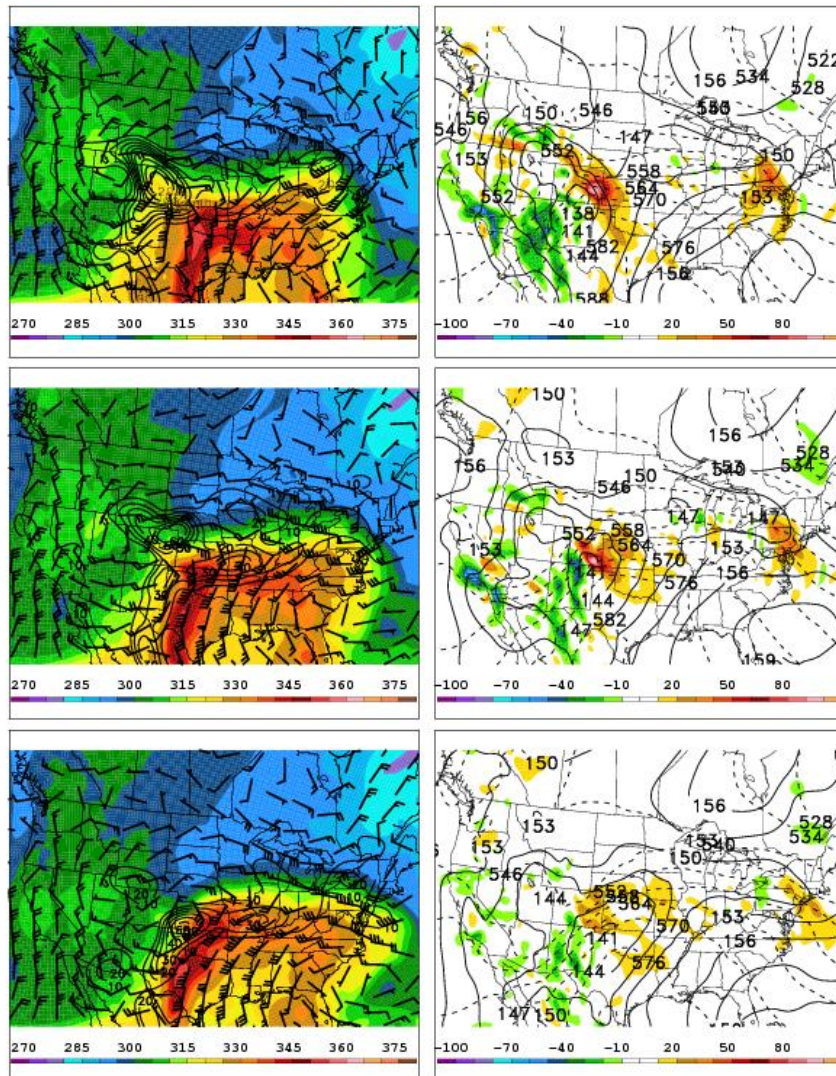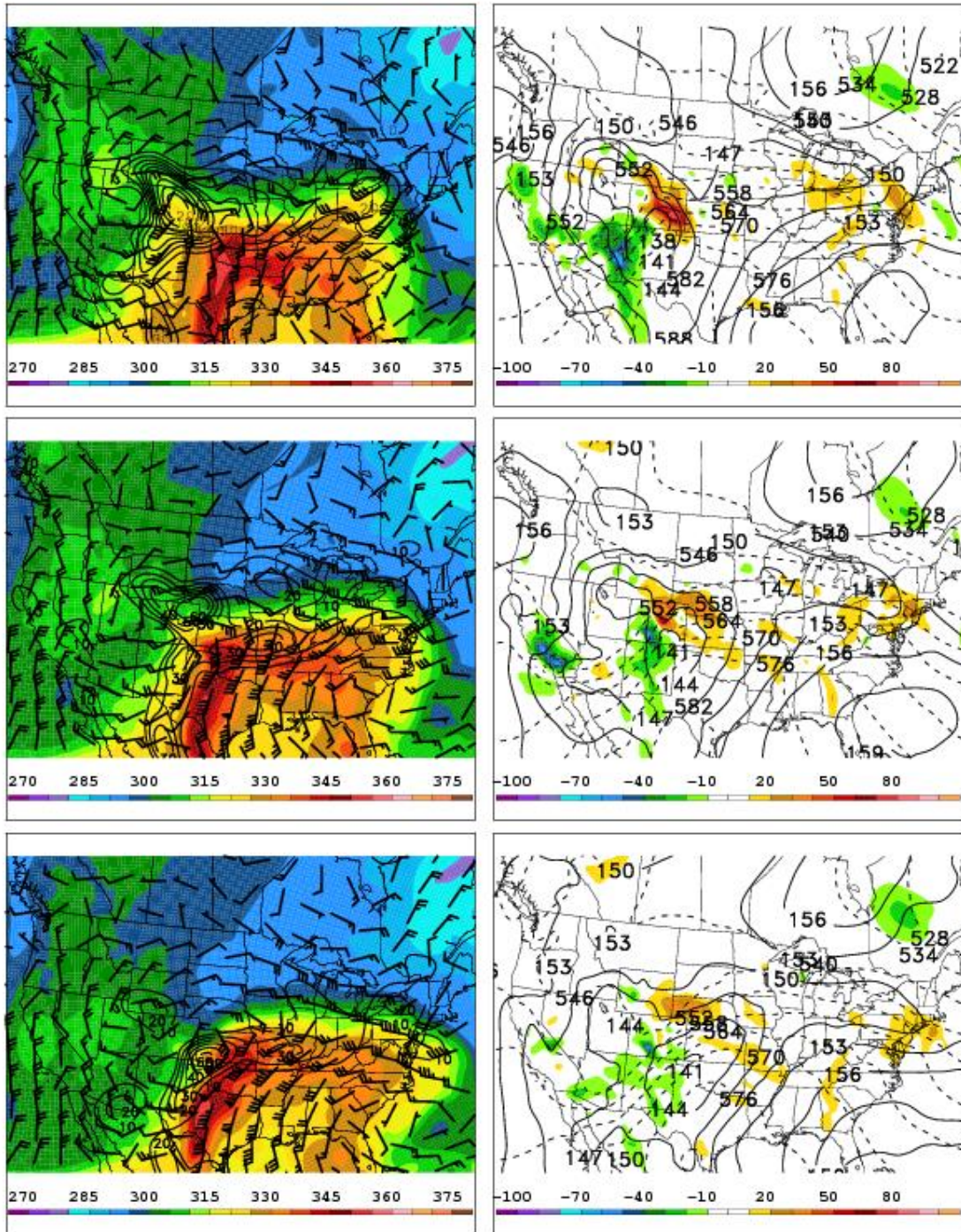
As in Fig. 4 (upstream trough case), but for temperature advection in the 850–500 hPa layer.
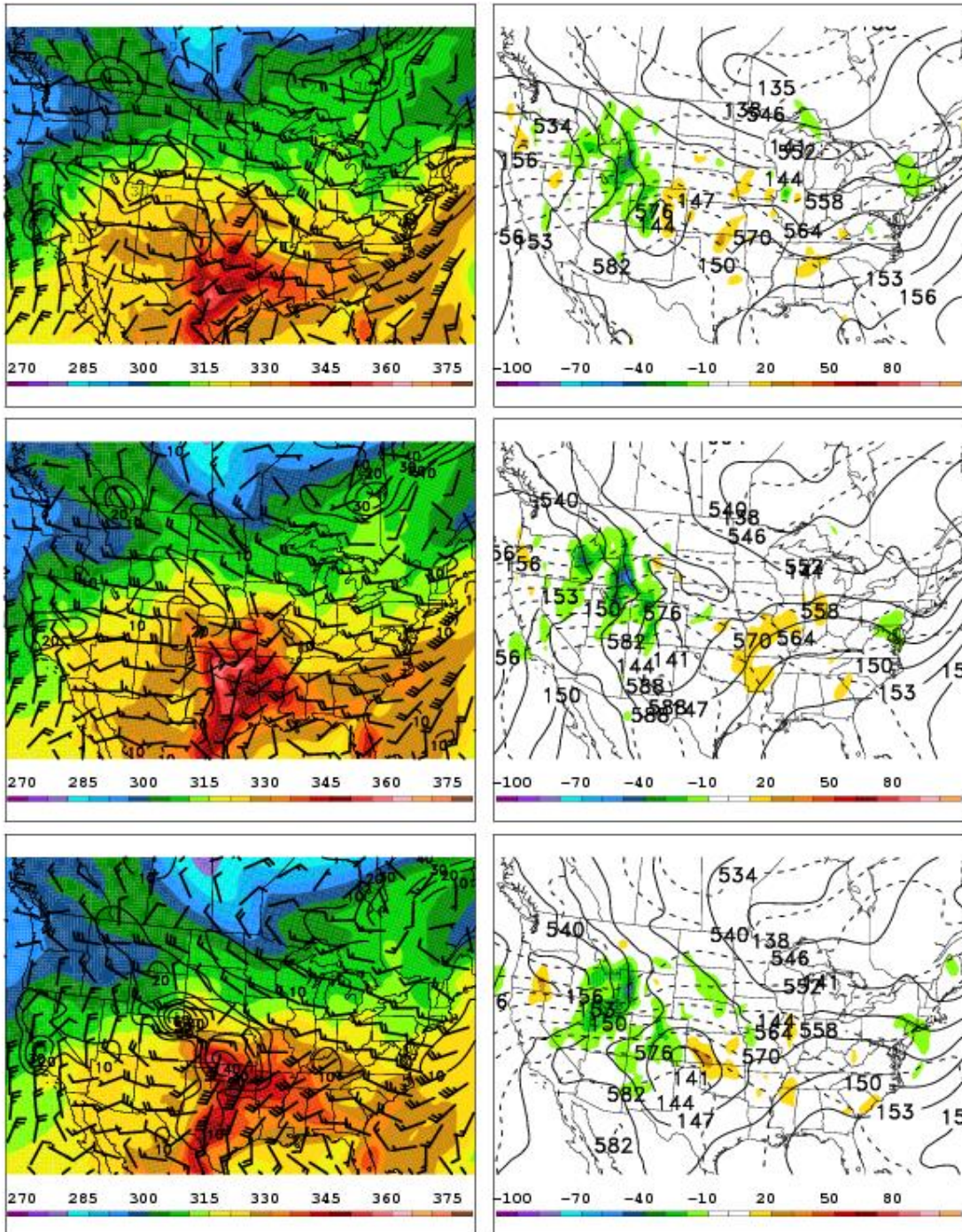
As in Fig. 4 (upstream trough case), but for temperature advection in the 700–400 hPa layer.

As in Fig. 6 (zonal case), but for temperature advection in the 850–500 hPa layer.

As in Fig. 6 (zonal case), but for temperature advection in the 700–400 hPa layer.
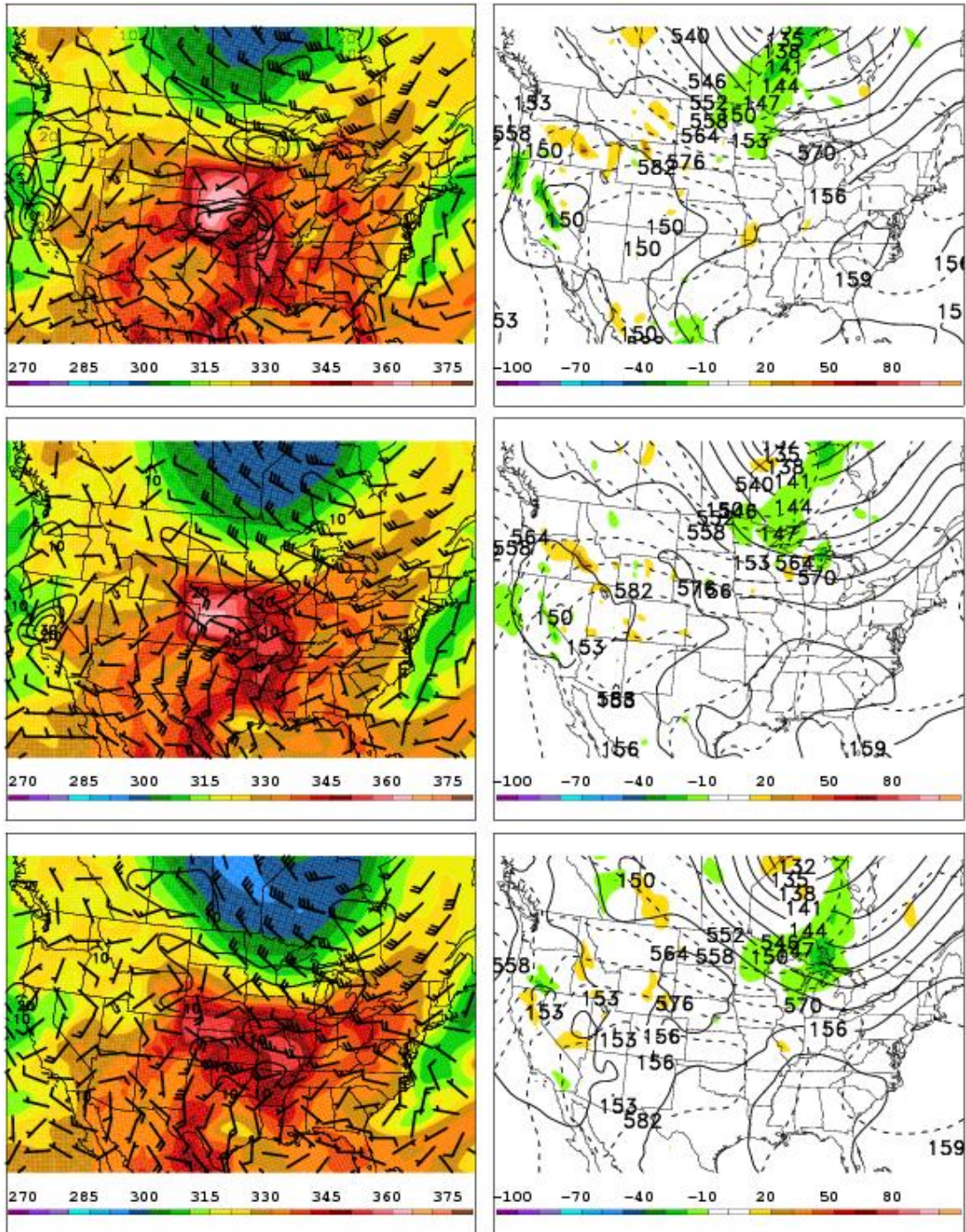
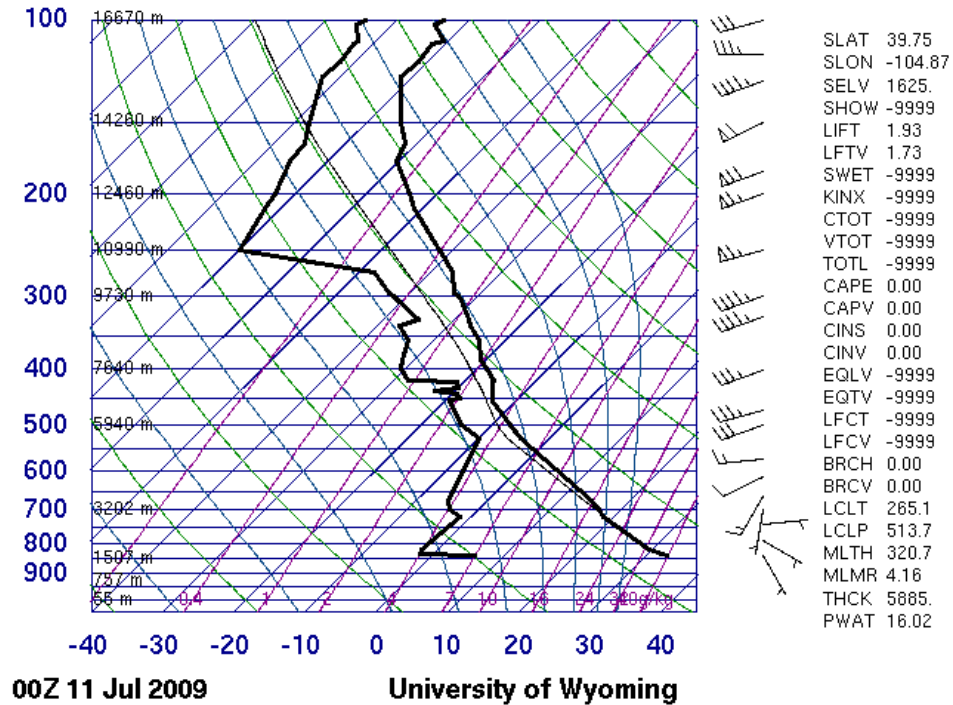*As in Fig. 8 (ridge case), but for temperature advection in the 850–500 hPa layer.*
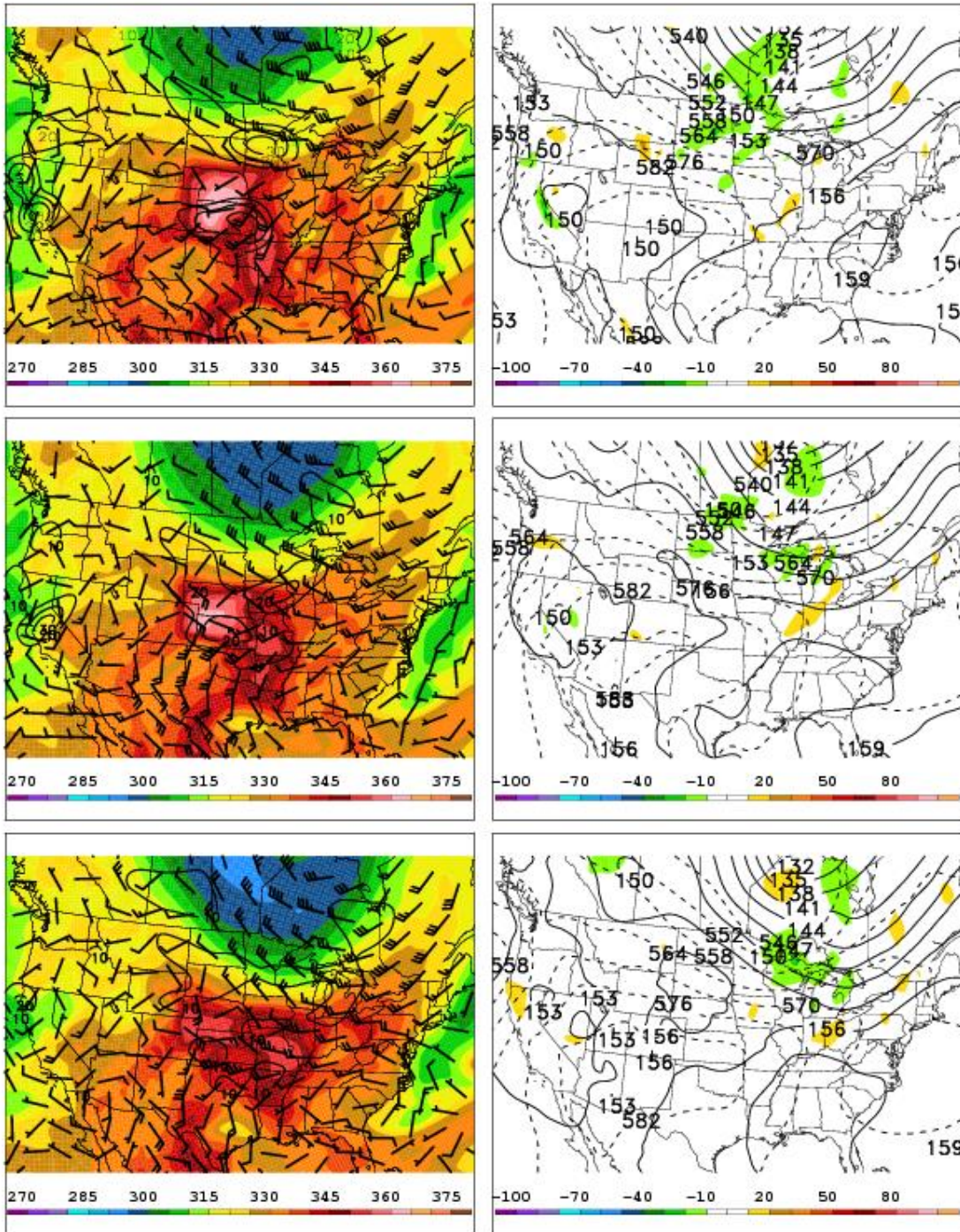
As in Fig. 8 (ridge case), but for temperature advection in the 700–400 hPa layer.
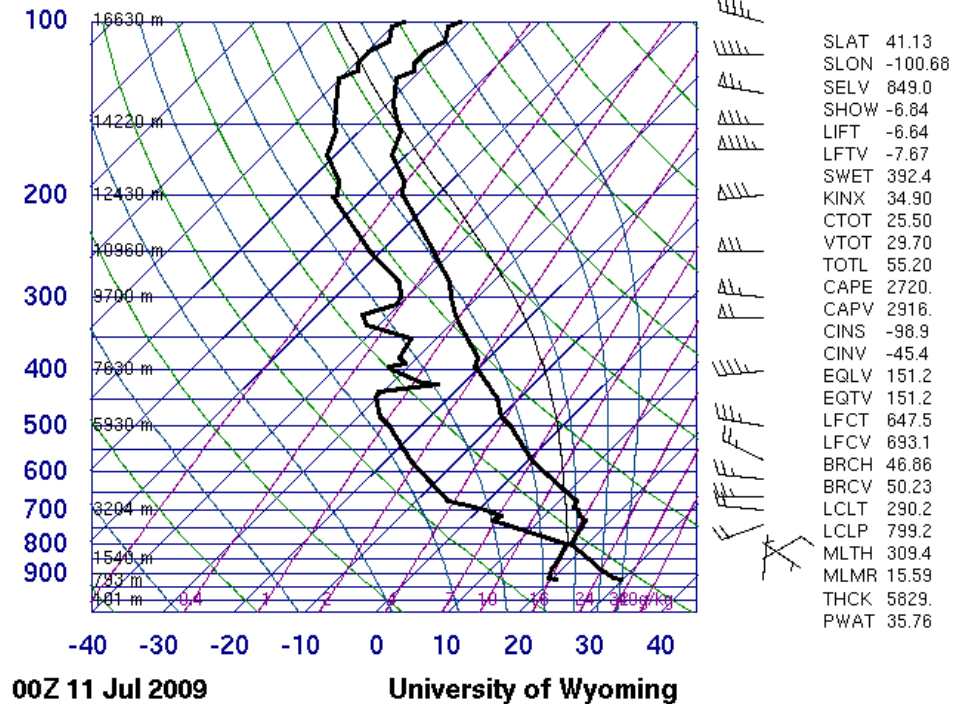
As for the soundings, below you will find the soundings at t = –6 h of the ridge case (0000 UTC 11 Jul 2009) from Denver (DNR) and North Platte (LBF). The flow in the boundary layer does appear a little decoupled at DNR, but not at LBF. However, it is clear that the soundings show weak WAA in whichever layer you use (850–700, 850–500, 700–400). If you feel that the 700–400 hPa temperature advection plots are more physically representative, we are certainly willing to make the switch. For now, we will leave the

850–700 hPa plots in the paper. Also, we did go ahead and check the proximity soundings (from DDC) for the upstream trough and zonal cases, and they also confirm the WAA seen in the flat maps (see last two soundings pasted below). As a result, we now mention that the soundings confirm the in the paper, during the discussion of each case.

I too like the use of trajectories from ARL's system. Note that time dots are missing from panel a—the left panel. Perhaps you should note in the legend that the scaling for panel c—the right panel is different. It might be useful to add a small insert figure at lower left of each panel that shows the grid points for which the trajectories were calculated. It also might help the clarity of the figures to reduce the number of trajectories shown. When I examined an expanded version of the right panel, I found what appears to be a problem. The system is slow-moving, the grid mesh is relatively large, and wind speeds are weak. A number of the trajectories begin west of the MCC and thus represent inflow from the rear that ends up in the mesoscale downdraft. The time/pressure plots at the bottom leave the visual impression that all the trajectories come in from the east. Again, I think that there are a number of problems with the orographic case that need careful examination.

We have uncluttered the trajectory plots by making them a 2×2° box with only 9 grid points instead of 16 (see new Fig. 9). We have added a star (via the HYSPLIT plotter) to denote the location of each grid point used in the trajectory calculations, and a note in the Fig. 9 caption that panel (c) is to a different map scale. Reviewer A also brought up the issue of the trajectories coming from the west and then sinking. We think the new plot makes this much clearer, and we describe it in the text in section 4a4.

[Minor comments omitted...]